Enhanced-Resolution Processing and Applications of the ASCAT Scatterometer

Richard D. Lindsley

A dissertation submitted to the faculty of
Brigham Young University
in partial fulfillment of the requirements for the degree of

Doctor of Philosophy

David G. Long, Chair
Neal K. Bangerter
Brian D. Jeffs
Dah-Jye Lee
Karl F. Warnick

Department of Electrical and Computer Engineering

Brigham Young University

December 2015

ABSTRACT

Enhanced-Resolution Processing and Applications of the ASCAT Scatterometer

Richard D. Lindsley
Department of Electrical and Computer Engineering, BYU
Doctor of Philosophy

The ASCAT scatterometer measures the Earth surface microwave radar backscatter in order to estimate the near-surface winds over the oceans. While the spatial resolution of the conventional applications is sufficient for many purposes, other geoscience applications benefit from an improved spatial resolution. Specialized algorithms may be applied to the scatterometer data in order to reconstruct the radar backscatter on a high-resolution grid.

Image reconstruction requires the spatial response function (SRF) of each measurement, which is not reported with the measurement data. To address this need, I precisely model the SRF incorporating (1) the antenna beam response, (2) the processing performed onboard ASCAT before telemetering to the ground, and (3) the Doppler shift induced by a satellite orbiting the rotating Earth. I also develop a simple parameterized model of the SRF to reduce computational complexity. The accuracy of both models is validated.

Image reconstruction of the ASCAT data is performed using the modeled SRF. I discuss the spatial resolution of the reconstructed ASCAT images and consider the first- and second-order statistics of the reconstructed data. Optimum values for the parameters of the reconstruction algorithms are also considered. The reconstructed radar backscatter data may be used for enhanced-resolution wind retrieval and for geoscience applications. In this dissertation, the reconstructed backscatter data is used to map the surface extent of the 2010 *Deepwater Horizon* oil spill and in a study to quantify the azimuth angle anisotropy of backscatter in East Antarctica.

Near-coastal ocean wind retrieval is also explored in this dissertation. Because near-coastal ocean measurements of backscatter may be “contaminated” from nearby land and introduce errors to wind retrieval, they must be discarded. The modeled SRF is used to quantify the land contamination, enabling enhanced-resolution wind retrieval much closer to the coasts. The near-coastal winds are validated against buoy measurements.

Keywords: ASCAT, scatterometer, spatial response function, wind retrieval, image reconstruction

ACKNOWLEDGMENTS

First, I thank my advisor, Dr. Long. Thank you for years of support, instruction, and guidance. I appreciate your feedback in directing and improving my research and writing, and I am happy you introduced me to the exciting fields of radar and remote sensing.

I also thank my associates at EUMETSAT, especially Craig Anderson, Julia Figa-Saldaña, and Julian Wilson. Your technical expertise was critical in refining and correcting my research, and I enjoyed your warm hospitality during my stay in Darmstadt.

Finally, I am most thankful to my wife, Whitney. Even though I was perpetually "almost done," you've supported and encouraged me through many long hours and late nights.

Table of Contents

List of Tables

List of Figures

Chapter 1

Introduction

1.1 Overview

The land, oceans, and life on Earth are subject to a variety of natural processes. The wind over the oceans, for example, is partly responsible for both the natural climate of the Earth and for extreme events such as tropical cyclones. In order to understand these processes and to predict their future behavior, we depend on accurate observations of the Earth using a variety of sensors.

One class of Earth sensor is a spaceborne wind scatterometer. A scatterometer measures the microwave backscatter, or radar reflectivity, over a wide swath of the Earth's surface. The extensive spatial coverage enables measurements to be taken everywhere on the globe within a time span of a few days. The radar frequency selected is designed to be unaffected by cloud coverage yet sensitive to the desired characteristics of the Earth's surface. Because a scatterometer is an active microwave instrument, it does not require illumination from the Sun, enabling observations to be made both day and night.

The primary use of a scatterometer is to measure indirectly the wind speed and direction over the ocean surface. This is possible because the wind roughens the ocean surface: the roughness is proportional to the wind speed and is aligned with the wind direction. The amount of microwave power scattered back is related to this surface roughness. If the radar backscatter is measured with an appropriate viewing geometry, it is possible to invert the relationship between wind and backscatter to find the most probable winds that produced the observed backscatter.

While several scatterometers have been in operation over the past few decades, this dissertation focuses on the ASCAT (Advanced Scatterometer) series of scatterometers. Two ASCAT instruments are currently in operation with a third planned for launch in the near future. ASCAT is of particular geoscience value because the data from current and planned ASCAT instruments constitute a consistent and well-calibrated dataset that potentially spans over a decade of continuous measurements.

Although a spaceborne scatterometer such as ASCAT has excellent global coverage, a drawback is the relatively coarse spatial resolution of its measurements: usually on the order of 20 km to 50 km. The spatial resolution is due to several factors, including the large distance between the satellite and the Earth (a common orbit altitude is about 800 km), the microwave frequency used, the size of the antennas, and the method by which the measurements are processed. Improving the resolution of the backscatter data is desirable for a variety of geoscience applications.

This dissertation addresses methods of processing ASCAT scatterometer data in a way that improves the spatial resolution over that of traditional methods. The ASCAT measurement spatial response function (SRF) is derived and validated. An accurate SRF enables enhanced-resolution image reconstruction of the microwave backscatter from the Earth's surface. The performance of various image reconstruction algorithms using ASCAT data are compared, including a spectral analysis to evaluate the recovery of high-frequency content. Some applications of the enhanced-resolution backscatter data are also explored. These include mapping geophysical features such as oil spills and enabling high-resolution wind estimates. The SRF is additionally used to enable the estimation of near-coastal winds, which are validated through comparison against buoy measurements.

1.2 Summary of Results

Previous work has produced and applied enhanced-resolution data for other scatterometers. This dissertation builds on this previous work and extends it to ASCAT. ASCAT is designed to follow the heritage of previous scatterometers while making important improvements. Notwithstanding its similarity with previous scatterometers, special considerations must be made to update and apply the extant work for ASCAT.

A central contribution to this dissertation is an understanding of the ASCAT spatial response function. The SRF quantifies how much an arbitrary point on the Earth surface contributes to the total backscatter measurement. The ASCAT SRF is utilized in the ground processing of the raw ASCAT telemetry into scientific values. However, the ASCAT SRF is not reported in the published data nor thoroughly described in any official documentation. This necessitates “reverse-engineering” the SRF based on available information.

This dissertation presents a model of the ASCAT SRF, which is composed of three major factors: (1) the antenna pattern, (2) the range-Doppler processing performed onboard ASCAT, and (3) the data averaging performed onboard before downlinking the data. Accurately modeling each factor requires a thorough understanding of the ASCAT hardware and software design.

In order to reduce the computational demands of the full SRF as modeled, an approximate model is also developed and presented in this dissertation. This approximation is compared against the modeled SRF and shown to have only negligible error, but it is two orders of magnitude faster to compute.

The SRF is used in conjunction with image reconstruction algorithms to produce backscatter measurements on a high-resolution grid. Three imaging algorithms are discussed: GRD, AVE, and SIR. These algorithms have been used successfully for previous scatterometers, but only GRD has been applied to ASCAT data. The appropriate processing parameters for these algorithms are selected for ASCAT. One such parameter is the grid spacing, or pixel size. Based on sampling theory and the ASCAT sampling geometry, appropriate grid spacing is selected to minimize aliasing of the backscatter signal for single and multiple passes.

Another contribution of this dissertation is to characterize the first- and second-order statistics of the GRD, AVE, and SIR algorithms. Results are shown using the ASCAT sample geometry, but the technique is applicable to any arbitrary sample geometry and SRF. These image statistics may be used to evaluate the bias, accuracy, and precision of the resulting images. The correlation of an arbitrary pixel with its neighboring pixels is also evaluated.

Although it is difficult to precisely quantify the spatial resolution of the reconstructed backscatter images, a basic spectral analysis is conducted to obtain some idea of the resolution of the processed data. The behavior in both spatial and frequency domains for GRD, AVE, and SIR is compared and discussed. The AVE algorithm is shown to have high-frequency content, but it is attenuated. While the SIR algorithm has similar spatial resolution to AVE, SIR is able to recover most of the attenuated content.

The reconstructed backscatter data have a variety of geoscience applications. One example is the mapping of large oil spills. The 2010 *Deepwater Horizon* oil spill, while environmentally devastating, is unique in producing a very large area of surface oil. This allows ASCAT to be used to map the spill extent and monitor its evolution. Another application of enhanced-resolution backscatter is the mapping of the azimuth angle anisotropy of radar backscatter over East Antarctica. The azimuth-dependent backscatter is due to unusual geophysical features, including sastrugi and wind glaze. Mapping the azimuth anisotropy indirectly maps these geophysical features as well.

The ASCAT SRF is essential for near-coastal wind retrieval. Backscatter measurements of the ocean may be biased, or contaminated, due to nearby land. Traditionally all near-coastal backscatter measurements are excluded from the wind retrieval process to avoid the errors introduced by land contamination. This restricts the closest retrievable winds to about 30 km from coastlines and islands. However, due to the ASCAT SRF shape, size, and orientation, not all near-coastal measurements are necessarily land contaminated. The land contribution ratio (LCR) is a metric to quantify the land contamination based on a land map and the SRF. Previous work introduced the LCR and successfully applied it to near-coastal data for the QuikSCAT scatterometer. This dissertation applies the LCR approach to ASCAT data. With the LCR, winds may be estimated as close to 5 km of land. In order to evaluate the efficacy of the LCR method, the ASCAT high-resolution winds are compared against winds measured by buoys near coasts. The results show no evidence of error due to land contamination when processed with the LCR method.

1.3 Outline

The remainder of this dissertation is organized as follows: Chapter 2 presents background information for the subsequent chapters. A brief overview of scatterometry is presented with a focus on the ASCAT scatterometer. Previous work on and applications of enhanced resolution backscatter reconstruction are reviewed. Chapter 3 details the measurement spatial response function for ASCAT. A "reference SRF" that models the SRF using the full measurement geometry is presented. A parameterized approximation is developed in order to decrease computation time. The validation of both SRF estimates is considered. Chapter 4 details the use of the estimated SRF in enhanced resolution backscatter reconstruction algorithms. The spatial resolution, first- and second-order statistics, and reconstruction processing parameters are considered. Chapter 5 examines an application of enhanced resolution backscatter data: near-coastal enhanced-resolution wind retrieval. Enhanced-resolution wind retrieval is discussed, and the issue of land contamination near coasts is examined. The ASCAT SRF may be used to mitigate land contamination, enabling wind retrieval close to coasts. The resulting near-coastal wind data are compared against buoy-measured winds. Chapter 6 presents two additional applications of enhanced resolution backscatter and wind data: mapping the *Deepwater Horizon* oil spill and the azimuth variation of data over East Antarctica. Finally, Chapter 7 summarizes the work presented in this dissertation and discusses avenues for future work.

Chapter 2

Background

This chapter provides the background information required to place the material in the subsequent chapters of this dissertation into context. An overview of scatterometry is first provided. A description of the ASCAT scatterometer, on which this dissertation focuses, follows. Sampling and reconstruction of the Earth σ° from scatterometer measurements is next considered. Previous applications of reconstructed σ° data are then described. The chapter concludes with a review of the previous work conducted for land and oil contamination in ocean σ° measurements.

2.1 Scatterometry

Near-surface ocean winds are an important geophysical parameter. These winds drive the flow of heat, moisture, and the ocean itself. Local and global climate are both affected by winds [2, 3]. While ships and buoys can measure local ocean winds, only a satellite-hosted sensor can measure wind on a global basis within a day or two. The sensor commonly chosen is an active microwave radar due to its ability to measure the ocean surface regardless of solar illumination or cloud cover [2, 3].

The radar equation relates the power received by a radar to the power it transmits:

$$\frac{P_r}{P_t} = \frac{G^2\lambda^2}{(4\pi)^3 R^4}\sigma, \tag{2.1}$$

where P_t and P_r are the power transmitted and received; G is the one-way antenna gain; λ is the wavelength of the electromagnetic radiation; R is the distance, or range, between the radar and the target; and σ is the radar cross section of the target. For simplicity, this formulation is for a monostatic radar (same antenna for transmission and reception) at a single polarization with a single point target. The radar cross section (RCS) has units of square area [4].

For remote sensing of distributed targets (e.g., terrain or other geophysical features, as opposed to "hard targets" such as aircraft or buildings), the radar equation is modified to account for the multiple scatterers within the measurement footprint:

$$\frac{P_r}{P_t} = \iint_A \frac{G^2 \lambda^2}{(4\pi)^3 R^4} \frac{\sigma}{A} \, dA, \tag{2.2}$$

where A is the area illuminated by the radar beam and the integration is over the entire antenna footprint (i.e., $A = \iint_A dA$). When the RCS is normalized by the area of integration, it is a dimensionless quantity, the *normalized radar cross section* (NRCS), or often simply the *backscatter coefficient* or *radar reflectivity*:

$$\sigma^\circ = \sigma / A. \tag{2.3}$$

The NRCS σ° is a property of the Earth surface. Areas that are are smooth and reflective (e.g., oceans and lakes) scatter very little energy back in the direction of the radar; therefore, the σ° value is low. Areas that are rough (e.g., vegetation) scatter energy in all directions, with more energy scattered back to the radar; therefore, the σ° value is higher [4].

Many terms in Eq. (2.2) are a function of location within the antenna footprint:

$$\frac{P_r}{P_t} = \frac{\lambda^2}{(4\pi)^3} \iint_{x,y} \frac{G(x,y)^2}{R(x,y)^4} \sigma^\circ(x,y) \, dx \, dy. \tag{2.4}$$

If $\sigma^\circ(x,y)$ is constant over the area A, then it can be factored out and solved for:

$$\sigma^\circ = \frac{P_r}{P_t} \frac{(4\pi)^3}{\lambda^2 \iint_{x,y} \frac{G(x,y)^2}{R(x,y)^4} \, dx \, dy} \tag{2.5}$$

$$\sigma^\circ = \frac{P_r}{X}. \tag{2.6}$$

The term X encompasses all other terms in the radar equation [5], and is sometimes referred to as "the X-factor". It normalizes the received power of the radar by all other terms that may vary measurement to measurement and are in consequence of the instrument geometry (e.g., the range and antenna gain) so that σ° is intrinsic to the surface and not to the radar system.

In practice, $\sigma^\circ(x, y)$ is not constant over A. Letting the term s refer to the normalized power, then

$$\begin{aligned} s &= \frac{P_r}{X} && (2.7) \\ &= \frac{\iint_{x,y} \frac{G(x,y)^2}{R(x,y)^4} \sigma^\circ(x, y)\; dx\, dy}{\iint_{x,y} \frac{G(x,y)^2}{R(x,y)^4}\; dx\, dy} && (2.8) \\ &= \frac{\iint_{x,y} h(x, y)\sigma^\circ(x, y)\; dx\, dy}{\iint_{x,y} h(x, y)\; dx\, dy}, && (2.9) \end{aligned}$$

where $h(x, y)$ is the measurement *spatial response function* (SRF) [4,5]. Similar in role to X, $h(x, y)$ abstracts some of the less relevant details. A scatterometer, in effect, measures

$$s_i = \frac{\iint_{x,y} h_i(x, y)\sigma^\circ(x, y)\; dx\, dy}{\iint_{x,y} h_i(x, y)\; dx\, dy}, \tag{2.10}$$

where s_i is measurement i (not accounting for measurement noise), $h_i(x, y)$ is the SRF for measurement i, and $\sigma^\circ(x, y)$ is the true signal: the radar reflectivity of the Earth's surface. The class of radar used is thus called a scatterometer, since it accurately measures the radar backscatter of the Earth's surface.

For a wind scatterometer, its science objective is to infer ocean vector (speed and direction) wind from σ° measurements. At the oblique incidence angle range used for scatterometers (30° to 60° for ASCAT), the scattering mechanism from the ocean surface roughness is due to Bragg scattering. When ocean wave wavelengths of λ_o fulfill the Bragg resonance condition,

$$\lambda_o = n\lambda_r / 2 \sin\theta, \quad n = 1, 2, \ldots, \tag{2.11}$$

where λ_r is the radar wavelength and θ is the incidence angle, the electromagnetic waves constructively self-interfere to enhance the surface σ° value [4]. While modulated by larger gravity waves, Bragg waves are generally in equilibrium with near-surface wind speed [3]. Higher winds generate more Bragg waves, leading to greater σ° values for greater wind speeds.

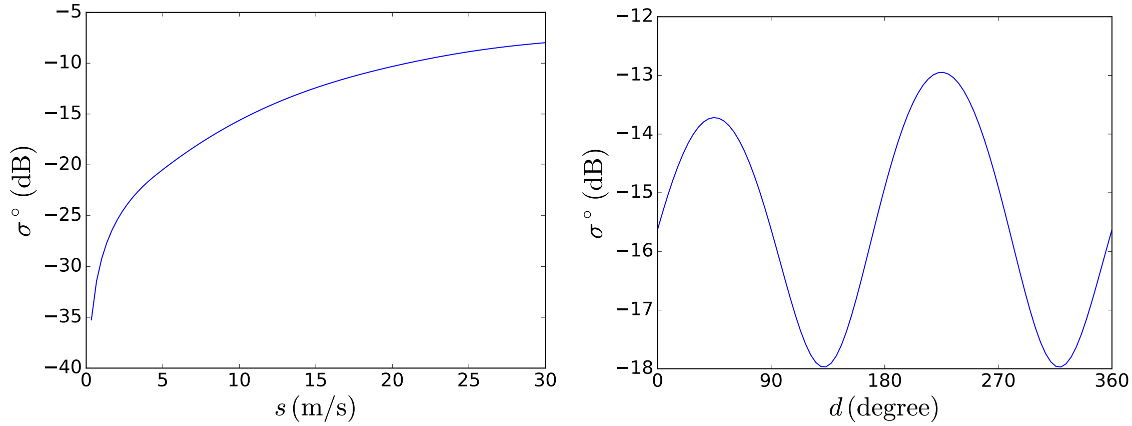

Figure 2.1: The ASCAT geophysical model function, CMOD5.n, for $\theta = 40°$, $\phi = 45°$. The left subfigure is $\sigma°$ as a function of speed, given a wind direction of 0°. The right subfigure is $\sigma°$ as a function of wind direction, given a speed of 10 m/s.

The relationship between $\sigma°$ and ocean wind at a standard height of 10 m above the ocean surface is given by an empirically derived geophysical model function (GMF), $\mathcal{M}$:

$$\sigma^\circ = \mathcal{M}(s, d - \phi, \theta), \tag{2.12}$$

where s is the wind speed, d the wind direction, ϕ the radar azimuth direction, and θ is the incidence angle [3, 4, 6] (frequency and polarization dependence are omitted since ASCAT operates at a single frequency and polarization). Figure 2.1 illustrates the GMF used for ASCAT, CMOD5.n [7], as a function of wind speed and direction given known incidence and azimuth angles.

A single $\sigma°$ measurement is insufficient to invert the GMF. Due to the sinusoidal nature of the GMF, multiple $\sigma°$ measurements at different azimuth angles are required to uniquely determine s and d. This motivates a common scatterometer design in which each location on the ground is measured multiple times at different azimuth angles. A max-likelihood estimator is used to estimate the wind speed $\hat{s}$ and direction $\hat{d}$ from the set of collocated $\sigma°$, θ, and ϕ measurements given a measurement variance ς_i^2 [4, 6, 8]:

$$[\hat{s}, \hat{d}]^T = \arg\min_{s,d} \sum_{i=1}^{N} \frac{(\sigma_i^\circ - \mathcal{M}(s, d - \phi_i, \theta_i))^2}{\varsigma_i^2}. \tag{2.13}$$

The estimation of vector winds from the associated σ° measurements is termed *wind retrieval* [2]. Because the GMF is not a one-to-one function, inversion of the GMF (i.e., solving Eq. (2.13)) leads to several non-unique solutions, or ambiguities. Spatial consistency constraints are used to select a unique vector wind [4, 9, 10].

Scatterometer data are primarily designed to retrieve vector winds over the ocean, but they are also valuable for other geoscience applications. These include mapping and classifying sea ice [11, 12], tracking icebergs [13, 14], measuring soil moisture content [2, 15], mapping changes in vegetation [2, 16], estimating rain over the ocean in addition to wind estimation [17, 18], and measuring azimuth anisotropy over Antarctica [19, 20] and Greenland [21].

2.2 ASCAT

The Advanced Scatterometer on the MetOp series of satellites (ASCAT) is a wind scatterometer that measures σ°. ASCAT is a vertically polarized fan beam scatterometer operating at 5.255 GHz in the C band [2]. The ground geometry is illustrated in Fig. 2.2. Six beams—three for each of the two swaths—measure at fore, mid, and aft azimuth angles. Range-Doppler processing subdivides each fan beam into 256 measurements at varying incidence angles, although only a subset of 192 measurements is reported. These measurement locations are also termed "nodes". The six beams are periodically calibrated to maintain the accuracy of the σ° measurements and the derived geophysical parameters, such as wind or soil moisture.

An ASCAT instrument currently operates on each of the MetOp-A (2006–present) and MetOp-B (2012–present) satellites. These two ASCATs are referred to as ASCAT-A and ASCAT-B, respectively. A third ASCAT, on MetOp-C, is planned for launch within a few years. The MetOp satellites are in a sun-synchronous near-polar orbit with a ground track repeat of 29 days [2]. The MetOp satellites and their associated sensors are managed by EUMETSAT in Darmstadt, Germany.[1] The raw telemetry from ASCAT is downlinked every orbit (at the Svalbard Satellite Station with a backup at the NOAA station in Fairbanks, Alaska) and processed at EUMETSAT for later distribution.

The measurement values (radar backscatter, incidence angle, azimuth angle) and location (in latitude and longitude) are reported for each measurement within each beam.

---

[1] `http://eumetsat.int`

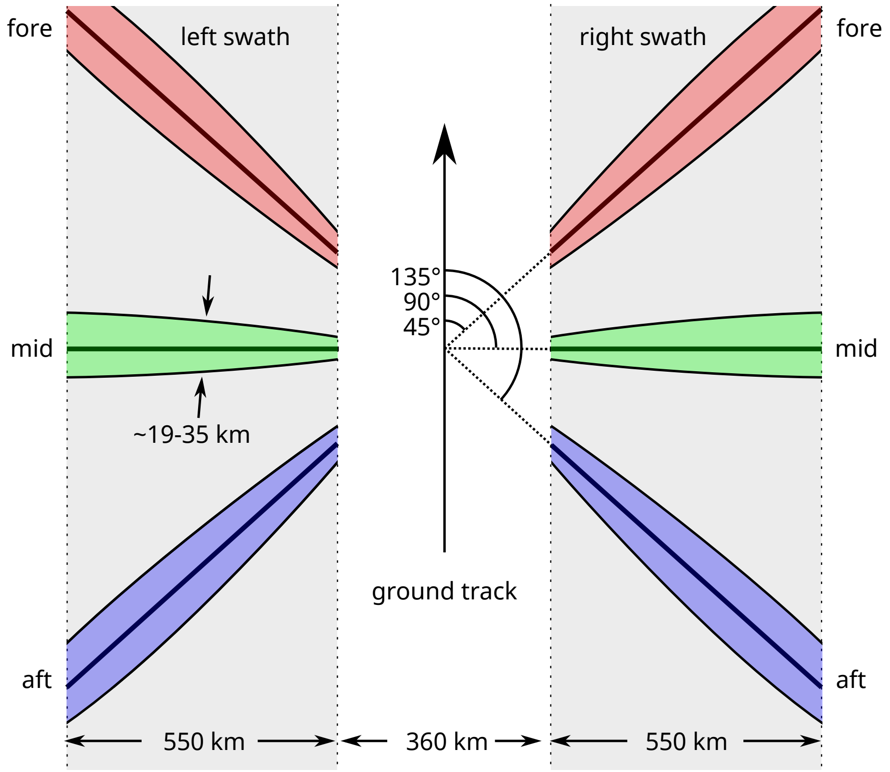

Figure 2.2: ASCAT ground measurement and swath geometry. Each swath is sampled at a range of incidence angles at fore, mid, and aft azimuth angles. Surface beamwidth is exaggerated for illustrative purposes.

This is the "full resolution" (SZF) Level 1B (L1B) product. Spatially averaged products are also produced, in which a swath-oriented grid is defined and the value at each grid point is the combination of all nearby full-resolution measurements, spatially weighted with a Hamming window. This dissertation does not consider the spatially averaged products.

The sampling geometry and incidence angle dependence is distinctly different for ASCAT than for other recent scatterometers, such as the QuikSCAT (1999–2009), OSCAT (2009–2014), and RapidSCAT (2014–present) scatterometers, which all are scanning pencil-beam scatterometers at a fixed incidence angle. ASCAT is an improved version of the ERS (1992–1996; 1996–2001) scatterometers, which have a similar fan-beam design but only a single swath.

ASCAT measures σ° over a wide range of incidence angles θ. Over land and sea ice with incidence angles from about 30° to 60°, the dependence of σ° on θ can be modeled as a

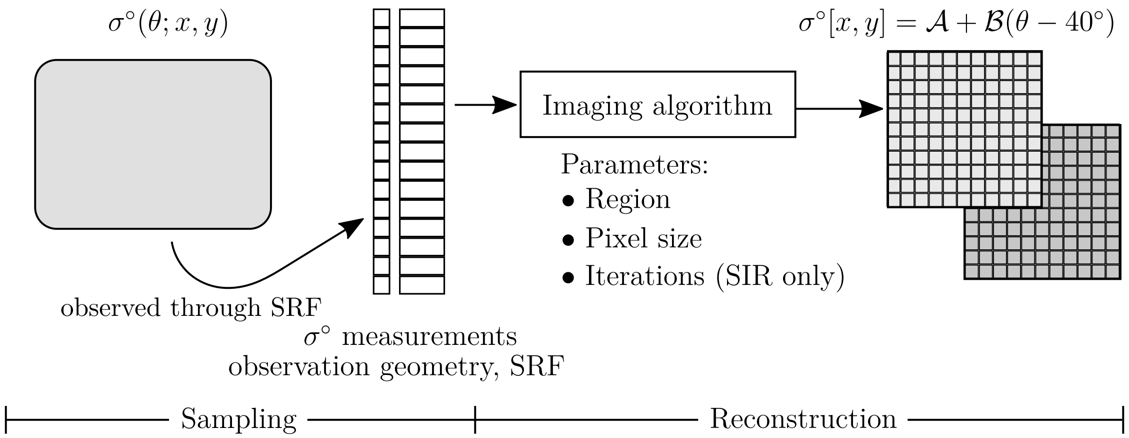

Figure 2.3: The sampling and reconstruction process. The sampling process is already determined by instrument design and orbit geometry. For reconstruction, $\sigma^\circ[x, y]$ is represented from the ASCAT measurements, subject to parameters such as pixel size and reconstruction algorithm.

linear fit with σ° in a logarithmic space, such as dB:

$$\sigma^\circ(\theta) = \mathcal{A} + \mathcal{B}(\theta - 40^\circ). \tag{2.14}$$

In this model, σ° is decomposed into $\mathcal{A}$, which is the backscatter normalized to a 40° incidence angle, and $\mathcal{B}$, which describes the slope or gradient of the θ dependence [22–25]. While any reference angle may be used, 40° is commonly used for other fan-beam scatterometers, so to maintain consistency it is likewise applied for ASCAT.

2.3 Backscatter Sampling and Reconstruction

A diagram of the overall scatterometer sampling and reconstruction process is depicted in Fig. 2.3. The sampling process, including the measurement SRF used, is dictated by the instrument design and orbit geometry. The reconstruction process takes as input the sampled σ° data and associated observation geometry and produces an output σ° image, shown here as decomposed into $\mathcal{A}[x, y]$ and $\mathcal{B}[x, y]$ in order to express the incidence angle relationship from Eq. (2.14). Reconstruction parameters, including the choice of pixel size, are considered for ASCAT in Chapter 4.

Scatterometers, including ASCAT, sample the Earth surface σ° over a distributed area filtered with an aperture function. (More background on this special case of sampling is found in Appendix A.1.) Neglecting measurement noise, a model for the reported backscatter measurement produced is of the form

$$s_i = \frac{\iint \sigma^\circ(x,y) h_i(x,y)\, dx\, dy}{\iint h_i(x,y)\, dx\, dy}, \tag{2.15}$$

where measurement s_i is the weighted combination of the surface normalized radar cross section (NRCS) and the SRF $h_i(x,y)$ for measurement i [26]. The SRF represents the contribution from each location within the ground footprint and is a variable aperture function—i.e., the aperture function for each measurement may differ due to sampling geometry. If the SRF can be assumed to be normalized ($\iint h_i(x,y)\, dx\, dy = 1$), then Eq. (2.15) simplifies to

$$s_i = \iint \sigma^\circ(x,y) h_i(x,y)\, dx\, dy. \tag{2.16}$$

Accurate knowledge of the SRF is critical for the enhanced-resolution processing and applications considered in this dissertation. The ASCAT SRF is modeled in greater detail in Chapter 3.

The sampling equation of Eq. (2.16) may be discretized (as explained in Appendix A.1):

$$s_i = \sum_{x_k} \sum_{y_k} \sigma^\circ[x_k, y_k] h_i[x_k, y_k], \tag{2.17}$$

where i indexes the measurements and x_k and y_k index the regularly sampled locations, or equivalently, the pixels in the reconstructed image. $h_i[x_k, y_k]$ is the measurement spatial response function (SRF, or aperture) of measurement i at pixel $[x_k, y_k]$. For notational convenience below, the two-dimensional indexing of $a[x_k, y_k]$ is vectorized into a single dimension, j, so that j indexes $[x_k, y_k]$ (e.g., $j = x + N_x \times y$). Then Eq. (2.17) may be expressed more compactly:

$$s_i = \sum_j a_j h_{ij}. \tag{2.18}$$

A multiplicative model for scatterometer measurement noise often adopted [27] is

$$z_i = s_i(1 + K_{p,i}\,\nu_i), \tag{2.19}$$

where z_i is the σ° measurement affected by measurement noise, $K_{p,i}$ is a per-measurement noise term, and ν_i is a zero-mean unit-variance uncorrelated Gaussian random process. The noisy measurements z_i are distributed as

$$z_i \sim \mathcal{N}(s_i, (K_{p,i}\,s_i)^2). \tag{2.20}$$

2.3.1 Gridding

A traditional approach to form an image from σ° measurements, referred to in this dissertation as the GRD method, is to define a regularly spaced grid and use a "drop-in-the-bucket" method to grid the measurements into a two-dimensional image of σ°. In this method each grid element, or pixel, is the average of all measurement values (drops) whose centers fall within the pixel (bucket). The GRD method is expressed as

$$\sigma^\circ_{\mathrm{grd},j} = \frac{\sum_i z_i G_{ij}}{N_j}, \tag{2.21}$$

where G_{ij} is an indicator function with $G_{ij} = 1$ if the center of measurement i falls within GRD pixel j and 0 otherwise. $N_j = \sum_i G_{ij}$ is the number of measurements contained within pixel j. Since the samples are irregularly spaced, a coarse resolution grid (i.e., a large grid spacing) is required to reduce the number of pixels that do not contain any measurements and to increase the number of measurements per pixel. Assuming uncorrelated measurement noise, averaging more measurements together reduces the noise for each GRD pixel.

The chief drawback to gridding is the low spatial resolution of the resulting image. The effective resolution of the gridded data is the sum of the grid dimension and measurement spatial extent sizes. This is because although a measurement center may lie within a GRD pixel, as much as half of its SRF could be in neighboring pixels. An alternative imaging method interpolates the measurements on a higher-resolution grid. Since the measurements are noisy, the measurements are often averaged or filtered before interpolation to reduce the noise. Both approaches are effective in presenting the σ° samples as a spatial image but suffer from degraded spatial resolution.

Unlike the above approaches, image reconstruction retains the high-frequency information that is otherwise discarded, effectively inverting Eq. (2.16). The objective of reconstruction is to recover $\sigma^\circ(x, y)$—or more precisely, the uniformly sampled version $\sigma^\circ[x_i, y_i]$—from multiple overlapping aperture-filtered noisy measurements z_i [28]. Gridding, on the other hand, does not require modeling the SRF or the measurement noise.

2.3.2 Full Reconstruction

A conventional approach to reconstruction, or "full reconstruction", is considered first. For simplicity, measurement noise is neglected in this discussion. The discrete sampling in Eq. (2.18) may be represented as a matrix equation:

$$\vec{s} = H\vec{a}, \tag{2.22}$$

where $\vec{s}$ is the collection of measurements s_i, $\vec{a}$ is the vectorized image a_j (or $a[x_k, y_k]$), and H has elements h_{ij}. H is an $m \times n$ sampling matrix, where m is the number of measurements (rows) and n the number of pixels (columns).

The objective of reconstruction is to invert this matrix equation to obtain $\vec{a_r}$ (the r subscript for "reconstructed"):

$$\vec{a_r} = H^{-1}\vec{s}. \tag{2.23}$$

In practice, H is not square but either overdetermined ($m > n$, or more measurements than pixels) or underdetermined ($m < n$, or fewer measurements than pixels). One approach is to use the linear least-squares solution:

$$\vec{a_r} \approx H^\dagger \vec{s} \tag{2.24}$$

$$\vec{a_r} \approx (H^T H)^{-1} H^T \vec{s}. \tag{2.25}$$

However, for all but the smallest images, H is a very large sparse matrix, so this matrix inversion is not computationally feasible. Additionally, if there is any error in the H sampling matrix (e.g., due to an inaccurate model of the SRF), the error will also affect H^{-1} or $H^{\dagger}$. Finally, a further shortcoming is that measurement noise is left unmodeled and may be amplified.

2.3.3 Partial Reconstruction

An alternate reconstruction approach is to only perform a partial, or limited, reconstruction. Not only is this more computationally tractable than a full reconstruction, but it also serves as a regularization to reduce error from amplified noise. A particular partial reconstruction approach is the block additive algebraic reconstruction technique (AART) [29], an iterative technique. Further details on AART are found in Appendix A.2. This framework is shared by the AVE (weighted AVErage) and SIR (Scatterometer Image Reconstruction) algorithms.

The AVE and SIR algorithms are the chief reconstruction algorithms considered in this dissertation. These two algorithms use the measurement spatial response function (SRF), i.e., the ground footprint imposed by the antenna pattern and onboard processing [5, 25, 28, 29]. Partial reconstruction methods not considered in this dissertation include Backus-Gilbert inversion [30, 31], a gradient method in Banach spaces proposed in [32], and a maximum *a posteriori* approach [28].

The AVE and SIR algorithms have been applied to other scatterometers and radiometers, including QuikSCAT (1999–2009) [29], a long-running Ku-band pencil-beam scatterometer; OSCAT (2009–2014) [33], a scatterometer with similar design to QuikSCAT; NSCAT (1996–1997) [34], a Ku-band fan-beam scatterometer; and the scatterometers on ERS-1 (1992–1996) and ERS-2 (1996–2001) [29], a C-band scatterometer design previous to that of ASCAT. Enhanced-resolution data for these and other instruments are available online[2] as part of the NASA Scatterometer Climate Record Pathfinder project (SCP). The SCP datasets contain reconstructed high-resolution σ° imagery over many land and sea ice regions [23, 35].

---

[2] `http://scp.byu.edu`

For a collection of σ° measurements indexed by i, z_i, and a grid where j is the grid point, or pixel index, the AVE algorithm is

$$\sigma^\circ_{\mathrm{ave},j} = \frac{\sum_i z_i h_{ij}}{\sum_i h_{ij}}, \tag{2.26}$$

where h_{ij} is the SRF value $h_i(x, y)$ of measurement i sampled at pixel j. In effect, AVE is an average of all σ° measurements per pixel, weighted by the SRF value. The chief difference versus the GRD method is that the spatial extent of the measurement is defined by the SRF instead of treated as a point at the measurement center. Thus each σ° measurement may affect multiple pixels instead of only one. This permits a finer-resolution pixel grid than that used for GRD.

SIR is a modified algebraic reconstruction technique (ART) tuned for scatterometers and robust in the presence of noise [29]. The SIR algorithm is iterative with a nonlinear update term. The update term is weighted by the SRF similar to AVE:

$$\sigma^\circ_{\mathrm{sir},k,j} = \frac{\sum_i u^k_{ij} h_{ij}}{\sum_i h_{ij}}, \tag{2.27}$$

where u^k_{ij} is the SIR update term for SIR iteration k, measurement i, pixel j. The update term is

$$u^k_{ij} = \begin{cases} \left[\dfrac{1}{2p^k_i}\left(1 - \dfrac{1}{d^k_i}\right) + \dfrac{1}{a^k_j d^k_i}\right]^{-1} & d^k_i \geq 1 \\ \dfrac{1}{2}\, p^k_i (1 - d^k_i) + a^k_j d^k_i & d^k_i < 1 \end{cases}, \tag{2.28}$$

where a^k_j is $\sigma^\circ_{\mathrm{sir},k,j}$, pixel j of SIR iteration k; p^k_i is the forward projection of measurement i:

$$p^k_i = \frac{\sum_j a^k_j h_{ij}}{\sum_j h_{ij}}; \tag{2.29}$$

and d^k_i is a function of the σ° measurement z_i and the projection p^k_i:

$$d^k_i = \sqrt{\frac{z_i}{p^k_i}}. \tag{2.30}$$

The first iteration of SIR is AVE. As SIR continues to iterate, it progressively inverts the SRF; it equalizes spatial frequencies distorted due to the SRF frequency response while reconstructing the irregular sampling defined by the measurement locations. However, the number of SIR iterations is truncated as a form of regularization that reduces noise at the expense of spatial resolution. Further details on SIR may be found in [25, 29].

AVE and SIR are both partial reconstruction techniques to reconstruct σ° on a high-resolution grid, whereas GRD creates a σ° image on a conventional resolution grid. GRD, AVE, and SIR are all applied to ASCAT data in Chapter 4 and evaluated. The resulting σ° data have many applications.

2.4 Applications of Enhanced-Resolution Backscatter

The reconstructed σ° data from previous scatterometers have been used in many ways. Using a single pass of data, σ° may be reconstructed and used for high-resolution wind retrieval. This has been performed for QuikSCAT [36, 37] and its related scatterometers, OSCAT and RapidSCAT. The data has also been used for rain estimation [17, 38] and improved characterization of tropical cyclones [39].

With multiple passes of data, the spatial resolution of the reconstructed σ° data is improved at the expense of temporal resolution. Combining passes is best suited for temporally stable surfaces, such as land and ice. Applications of this reconstructed data include, among others, mapping and classifying sea ice [11, 40], melt detection of ice shelves [41], tracking and estimating icebergs [13, 14], analyzing melt and refreeze over Greenland [42], and mapping vegetation [43–45].

Although ASCAT has differing characteristics from the scatterometers used for the data above (e.g., polarization and frequency), it is anticipated that the creation of enhanced-resolution ASCAT σ° data will be of value for future scientific studies. A continuous C-band dataset currently spans nearly a decade with ASCAT-A and ASCAT-B, and is expected to continue to increase.

2.5 Contamination in Ocean Measurements

To fulfill its designed mission of near-surface ocean vector wind retrieval, a scatterometer measures σ° of the ocean surface. The relationship between σ° and vector winds is given by the GMF, defined in Eq. (2.12). However, there are two factors considered in this dissertation that the GMF alone does not account for: the contamination from nearby land and the effect of oil on the ocean surface. These are discussed separately below.

2.5.1 Land Contamination

Due to the distributed spatial extent of the measurement SRF, a near-coastal measurement whose center is over ocean may include σ° from nearby land or ice as well as the ocean. The land σ° value within the measurement footprint contaminates the ocean σ° measurement. The error due to land contamination carries through wind retrieval, such that the wind speed is overestimated.

A traditional approach to circumvent land contamination is to discard all σ° measurements within a distance threshold of land, for example 30 km (since this is on the order of the maximum size of an SRF). While effective, this approach is overly conservative since many measurements may lie within the distance threshold yet be free of land contamination.

A more informed approach is to evaluate the land fraction, or *land contribution ratio (LCR)* [46], which incorporates knowledge of the orientation, shape, and size of the measurement ground footprint. The LCR for measurement i is defined as

$$\mathrm{LCR}_i = \frac{\iint L(x,y)\, h_i(x,y)\; dx\, dy}{\iint h_i(x,y)\; dx\, dy}, \tag{2.31}$$

where $h_i(x,y)$ is the SRF for measurement i and $L(x,y)$ is a binary-valued land indicator function. Since the LCR is normalized by the SRF, it varies between 0 (entirely ocean) and 1 (entirely land). For computation purposes, the land map and SRF values are discretized on a high-resolution grid:

$$\mathrm{LCR}_i = \frac{\sum_{x,y} L[x,y]\, h_i[x,y]}{\sum_{x,y} h_i[x,y]}. \tag{2.32}$$

The LCR is a metric that characterizes the degree of land contamination in a σ° measurement, subject to the accuracy of the land mask and the SRF estimate. Measurements with LCR values greater than some threshold level are discarded and not used for wind retrieval. The LCR is successfully used for QuikSCAT [46] to mitigate contamination from known land and extended to include the variable sea ice contamination in near-polar regions [47]. It is also applied to ASCAT in Chapter 5.

2.5.2 Oil Contamination

Another source of contamination, even over open ocean away from land, is that from surface oil. Because oil is more viscous than sea water, oil on the ocean surface dampens the amplitude of Bragg waves. This modifies the σ° of the affected area because the smoother ocean surface reflects less microwave power back to the scatterometer. The σ° measurement of the oil-contaminated area is thus lower than the oil-free case [48–51].

The presence of oil in σ° imagery can be therefore determined by the contrast difference between oil-affected σ° with non-oil-affected σ°. The exact value of σ° over the ocean depends on many factors—geophysical, such as due to roughness induced by near-surface wind; instrument-specific, such as the frequency, polarization, and incidence and azimuth angles; and the type and the volume or thickness of surface oil. ASCAT is used in Section 6.1 to detect surface oil from the Deepwater Horizon oil spill.

While detecting oil from an anthropogenic oil spill is of interest, other sources—oil and otherwise—can also result in patches of dampened backscatter. These include biogenic oil slicks produced by plankton and fish, natural oil seeps from the ocean floor, organic wastes from fish processing ships, and changes in the water-ocean interface, such as that from upwelling [48]. Since these sources can lead to false positives in oil spill detection, they are referred to as "look-alikes." Techniques to reduce look-alikes include using multi-frequency and multi-polarization instruments [51–54]; applying *a priori* knowledge of geographic information, historical human and animal activity, and shipping lanes; and using different remote sensors that detect oil under mechanisms other than Bragg scattering (such as microwave radiometers or infrared, optical, or ultraviolet sensors) [48, 50]. Many of these look-alikes are too small to be resolvable by a scatterometer such as ASCAT. However, large regions with a low wind speed can have very low backscatter and potentially be confused with oil-covered ocean surface.

A challenge to oil detection using measured σ° is that the degree of σ° dampening due to oil depends on the near-surface wind speed. If the winds are below a threshold wind speed, the ocean surface is not sufficiently roughened to provide a contrast between the oil-contaminated surface and the oil-free surface. For C-band scatterometers such as ASCAT, this threshold is ≈ 3–$4\,\mathrm{m/s}$ [55]. Additionally, if the winds are too high (> 7–$10\,\mathrm{m/s}$), the surface oil mixes down into the water and may be less detectable. The wind speed range best suited for oil detection is therefore about 3–10 m/s. Previous work has recognized the importance of factoring wind speed in to surface oil detection [49, 50], and has done so, for example, as part of synergistic data methods [56].

Another geophysical influence on ocean backscatter is precipitation. At C-band, the radar band used by ASCAT, rain generally increases the observed σ° [57, 58]. As with oil- or land-contaminated σ° measurements, this backscatter bias results in a wind speed bias after wind retrieval.

2.6 Summary

This chapter has reviewed the theory of and motivation for wind scatterometry, with a description of the ASCAT scatterometer. The irregular aperture-filtered sampling of σ° and the reconstruction of σ° from scatterometer measurements have been reviewed. The AVE and SIR algorithms perform a partial reconstruction of σ° on a high-resolution grid, whereas the GRD method is limited to a reduced-resolution grid. Enhanced-resolution σ° reconstruction has successfully been employed for other scatterometers; this dissertation extends the reconstruction techniques to also operate on ASCAT data.

Oil and land contamination in ocean σ° measurements is also described. Oil contamination may be detected by a contrast in σ° since surface oil dampens the roughness of the ocean surface. However, this requires a sufficiently rough ocean surface due to moderate wind speeds. Land contamination is addressed by computing the LCR of each measurement. The LCR characterizes the level of land contamination in order to avoid inaccurate wind estimates. The SRF is required not only for σ° reconstruction, but also for the LCR. Thus, the ASCAT SRF must next be described.

Chapter 3

ASCAT Spatial Response Function

Each ASCAT measurement of radar backscatter, σ°, has an associated spatial response function (SRF), as described in Eq. (2.10). The measurement SRF quantifies the weighted contribution of the area of the Earth's surface around the measurement center. While the backscatter measurement alone is useful, some applications additionally require a good understanding of the SRF associated with each measurement. This chapter discusses the ASCAT SRF, whereas applications of the SRF are discussed in subsequent chapters of this dissertation.

The SRF is required in ground processing to convert each scatterometer measurement from received backscatter power to σ°. This is performed at the EUMETSAT ground Product Processing Facility (PPF) in order to create L1B data from the ASCAT raw telemetry (or, Level 0 data). However, once the ASCAT SRF is used to process the data to L1B, the SRF is not distributed. Instead, I develop an estimate of the measurement SRF. A key difference between the SRF used at the PPF and the version described in this chapter is that this SRF does not depend on quantities in the Level 0 data, but instead on the Level 1B data.

Section 3.1 describes the various components that shape the SRF. This modeled SRF is also termed the reference SRF. To reduce the computational demands of the estimate, the SRF may be parameterized, as described in Section 3.2. The two estimates are validated in Section 3.3.

For convenience, a locally tangent plane convention [59] is used to describe the SRF. Each measurement uses a different plane tangent to the Earth at the reported measurement center. Operating in the tangent plane permits working in units of linear distance (e.g., km) from the measurement center rather than in geodetic latitude and longitude. The tangent plane mapping is not applicable at extreme latitudes ($> |89.5°|$). Because the tangent plane is aligned with North, the axes of the tangent plane are in northing and easting.

3.1 Modeled SRF

The measurement SRF is the combination of several factors. The three main components examined here are (1) the antenna beam response, (2) the frequency response of the FFT-based onboard processing, and (3) the along-track pulse averaging performed onboard. Other factors may also influence the SRF, such as the onboard receive filter response, but these do not influence the response to the same extent as those outlined below. For brevity, many details about the geometry required to compute the SRF on a tangent plane are omitted here, but they may be found in [60].

3.1.1 Antenna Beam Response

The first component to the SRF is the response resulting from the antenna beam pattern. Of the six ASCAT beams, the antenna patterns of the four side beams are essentially identical to each other, and the patterns for the two mid beams are likewise identical.

In the following, only the antenna patterns in the cross-beam (or azimuth) direction are used. While the antenna response varies along the length of the beam (or elevation), the variation is small for each individual measurement. Thus, for the SRF, the along-beam response is treated to be constant. Because the modeled SRF is normalized so its peak value is unity, this also normalizes out the bulk along-beam response.

To account for the use of the antenna response for both transmission and reception, the magnitude-square of the normalized antenna gain pattern is used, corresponding to the G^2 term in Eq. (2.2). This is shown for the mid and side beams in Fig. 3.1.

3.1.2 Range-Doppler Processing

The second component to the SRF is the range-Doppler processing performed onboard. The range-Doppler processing subdivides the fan-beam antenna response, providing range resolution.

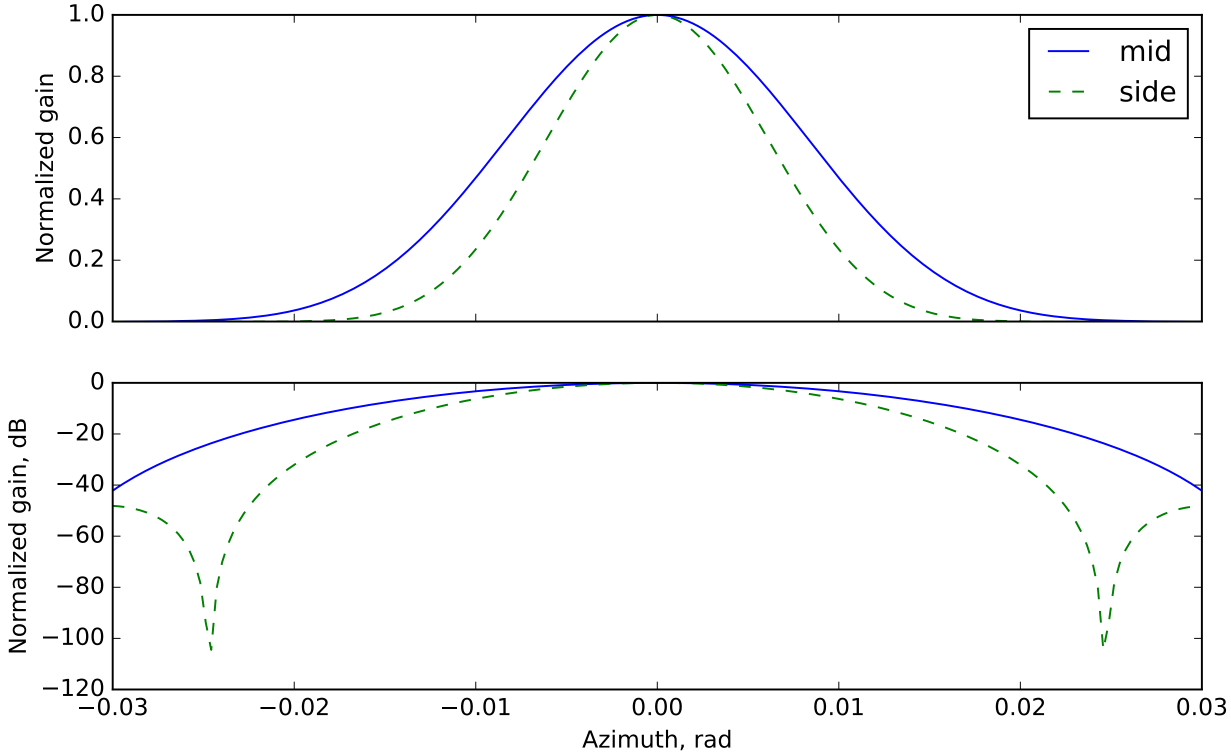

Figure 3.1: The cross-beam or azimuthal nominal antenna patterns. The mid (solid) and side (dashed) beams are shown together. The upper subplot is in linear space, the lower subplot in dB space. The values shown are for the magnitude-squared normalized antenna gain pattern.

ASCAT is a pulsed radar, with each pulse a linear FM chirp. The received signal—a sum of time-delayed and attenuated copies of the transmit chirp—is dechirped to baseband. This baseband signal is termed the *discriminator signal* and is sampled at 412.5 kHz. The power spectrum of the discriminator signal is estimated using Welch's method (viz., Fourier transforms of multiple overlapping segments of the sampled time-domain data are computed separately, magnitude-squared, and then averaged together). The discretely sampled power spectrum is the received power as a function of *discriminator frequency* [2, 26, 61], denoted here as $P[f]$.

The center frequency of each discriminator frequency FFT bin is given by

$$f_{\text{offset}} - \underbrace{\frac{4\alpha s}{c}}_{f_r} - \underbrace{\frac{2v_r}{\lambda}}_{f_d} = i\delta_f, \tag{3.1}$$

Table 3.1: Discriminator frequency parameters for Eq. (3.1).

Term	Value
$f_{\text{offset}}(\text{fore})$	$-189.0 \times 10^3\,\text{Hz}$
$f_{\text{offset}}(\text{mid})$	$-286.2 \times 10^3\,\text{Hz}$
$f_{\text{offset}}(\text{aft})$	$400.6 \times 10^3\,\text{Hz}$
$\alpha(\text{fore})$	$-1.03 \times 10^7\,\text{Hz/s}$
$\alpha(\text{mid})$	$-2.69 \times 10^7\,\text{Hz/s}$
$\alpha(\text{aft})$	$+1.03 \times 10^7\,\text{Hz/s}$
λ	$\frac{c}{f} = 5.71\,\text{cm}$
i	$0, 1, \ldots, 255$
δ_f	$\frac{412.5\,\text{kHz}}{512} = 805.7\,\text{Hz}$

where f_{offset} is a beam-dependent frequency offset, α the beam-dependent chirp rate, s the slant range from ASCAT to the Earth surface, c the speed of light, v_r the radial velocity between ASCAT and the Earth surface, λ the radar wavelength, i the FFT bin number, and δ_f the frequency bin width. Values for these parameters are given in Table 3.1. As noted by the underbraces, the discriminator frequency has components due to a range frequency, f_r, and a Doppler frequency, f_d. The received power is normalized to σ° using the radar equation (e.g., Eq. (2.6)), and Eq. (3.1) is solved for the slant range s, so $P[f]$ maps to $\sigma^\circ[s]$.

To better demonstrate the role of f_r and f_d, an illustration of how they contribute to the measurement SRF is shown in Fig. 3.2. Lines of constant range, or isoranges, and lines of constant Doppler frequency, or isodops, are shown. A zoomed illustration of a mid-looking ASCAT beam is shown in Fig. 3.3 with isoranges and isodops again illustrated. Since the discriminator frequency is the combination of f_r and f_d, a line of constant discriminator frequency does not follow an isorange—range and Doppler couple together into the discriminator frequency.

Due to the nature of the discrete Fourier transform, each FFT bin has an associated frequency response: the power in the bin is the weighted combination of signals at many frequencies. Since each (continuous) discriminator frequency in Eq. (3.1) maps to a point on the Earth surface, the bin frequency response maps to a spatial response on the ground. The frequency response of the FFT bins performed onboard ASCAT is derived in Appendix B.

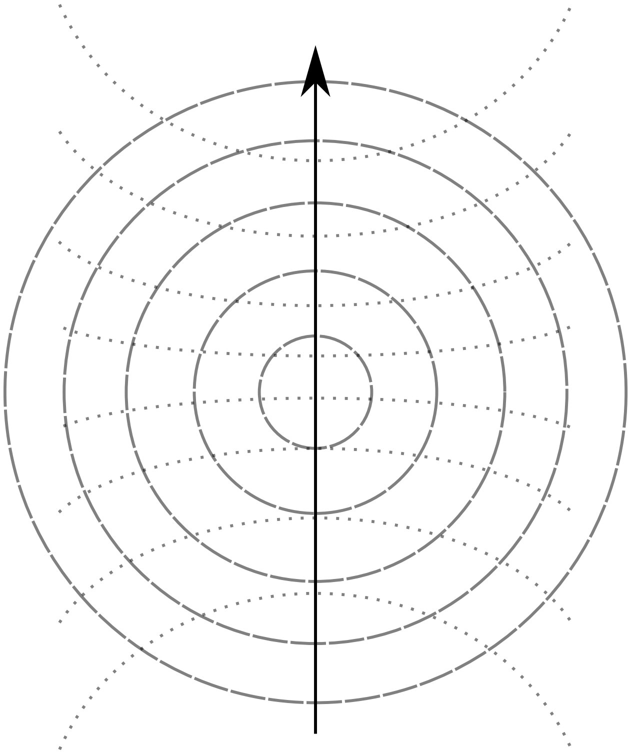

Figure 3.2: An illustration of lines of constant range (isoranges) and constant Doppler (isodops). In this case, isoranges are circles centered at nadir and isodops are hyperbolic. However, the exact isoranges and isodops are complicated by the fact that they are projected on a ellipsoidal Earth. The relative motion between the orbiting satellite and the rotating Earth further complicates the isodops.

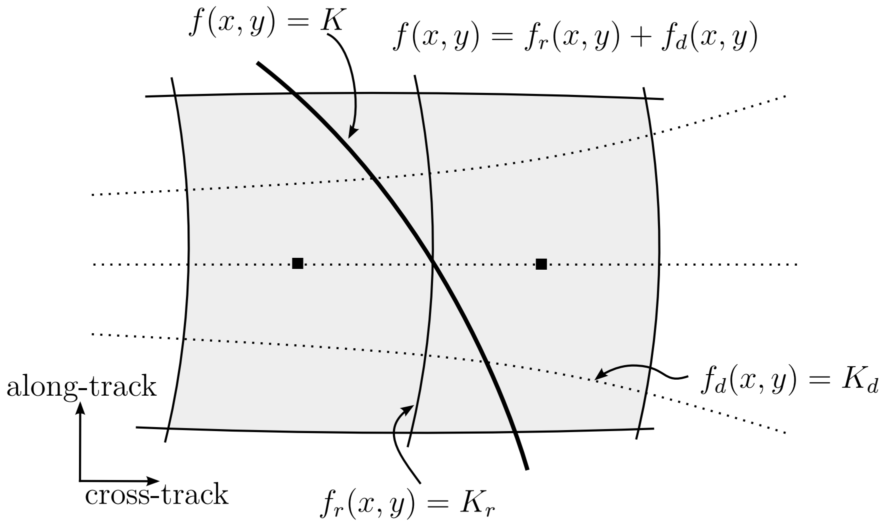

Figure 3.3: An illustration of a portion from a mid beam. Any point on the ground in (x, y) has a discriminator frequency $f(x, y)$ (ignoring f_{offset}). Isoranges and isodops are plotted, along with measurement centers indicated with the dark squares. A line of constant discriminator frequency is also denoted and is roughly a tilted isorange line.

3.1.3 Along-Track Pulse Averaging

The final major component to the SRF is the along-track pulse averaging performed onboard ASCAT [61]. This is performed to reduce the amount of data required to downlink from ASCAT to the ground. Each reported measurement is the weighted average of eight pulses. The weights are {0.05, 0.10, 0.15, 0.20, 0.20, 0.15, 0.10, 0.05}, and a measurement is saved every four pulses. The radar itself has a pulse repetition frequency (PRF) of approximately 28.26 Hz [62]. This is divided among the six beams, which are pulsed in sequence (left fore, left mid, left aft, right fore, right mid, right aft). Thus the PRF for each beam is $28.26/6 = 4.71$ Hz. The measurements are stored at a frequency of $4.71/4 = 1.1775$ Hz, or, since ASCAT orbits at a speed of about 6.7 km/s, about every 5.6 km along-track.

3.1.4 Cumulative Effect

The cumulative effect for all three components is illustrated for a sample measurement in Fig. 3.4. The measurement parameters are listed in Table 3.2 and the response is computed on a plane tangent to the measurement center [60]. For each location (x, y) on the locally tangent plane, the value of the SRF due to all three components (antenna pattern, FFT response, pulse average) is computed.

The antenna response for the sample measurement is illustrated in Fig. 3.4a. To estimate the range-Doppler SRF component, the frequency response of the 512-point onboard FFT, including the window function, is used to compute the ground response. The spatial response due to the FFT is shown in Fig. 3.4b for the sample measurement.

The cumulative effect of the range-Doppler processing on the antenna pattern is shown in Fig. 3.4c, which is a multiplication of the two responses in Figs. 3.4a and 3.4b. This is the SRF for a single ASCAT pulse so is termed the pulse SRF. Due to a non-negligible Doppler frequency f_d, the pulse SRF is rotated by roughly 60° from the cross-beam direction. The shape of the pulse SRF, due to the rotation, is generally observed to be elliptical.

The individual pulse locations are not reported in the L1B data so are estimated based on the measurement location, the along-track direction, and the ground-track velocity. The measurement SRF is computed by shifting the pulse SRFs to the correct locations and summing them together using the weighting given above [60]. The resulting measurement

Table 3.2: The parameters for a sample ASCAT measurement used for Fig. 3.4.

Beam	Right mid
Pass	Ascending
Incidence angle	38.24°
Location	66.52 ° N 299.67 ° E
Date	2011-10-26 (DOY 299)
Time	1:00:01.254Z

SRF for the sample measurement is shown in Fig. 3.4d. Pulse averaging generally gives the measurement SRF a more elliptical shape.

3.2 Parameterized Estimate

Although the SRF may be computed using the components outlined in Section 3.1, it is time-consuming to process. In order to increase the utility of the SRF, I develop a parameterized variant. Not only does this speed up the processing, but it significantly simplifies the code required to implement it.

The parameterization is based on the observation that the measurement SRF is generally an ellipse rotated such that the semi-minor axis is aligned with the spatial gradient of the discriminator frequency. The rotation angle between northing and the discriminator frequency gradient is termed ψ. The parameterized SRF is treated as separable in the directions aligned with the ellipse semi-major and semi-minor axes. Three parameters are modeled: (1) the ellipse rotation angle ψ, (2) the SRF response along the x (semi-minor) axis, and (3) the SRF response along the y (semi-major) axis. To compute the parameterized SRF value for a location near a measurement, the following high-level algorithm is used:

1. Define a location on the locally tangent plane centered on the reported measurement location
2. Rotate from tangent plane coordinates $(x_{\text{tp}}, y_{\text{tp}})$ to coordinates with respect to the SRF ellipse (x_d, y_d) using the angle ψ
3. Look up the SRF response in the x direction
4. Look up the SRF response in the y direction

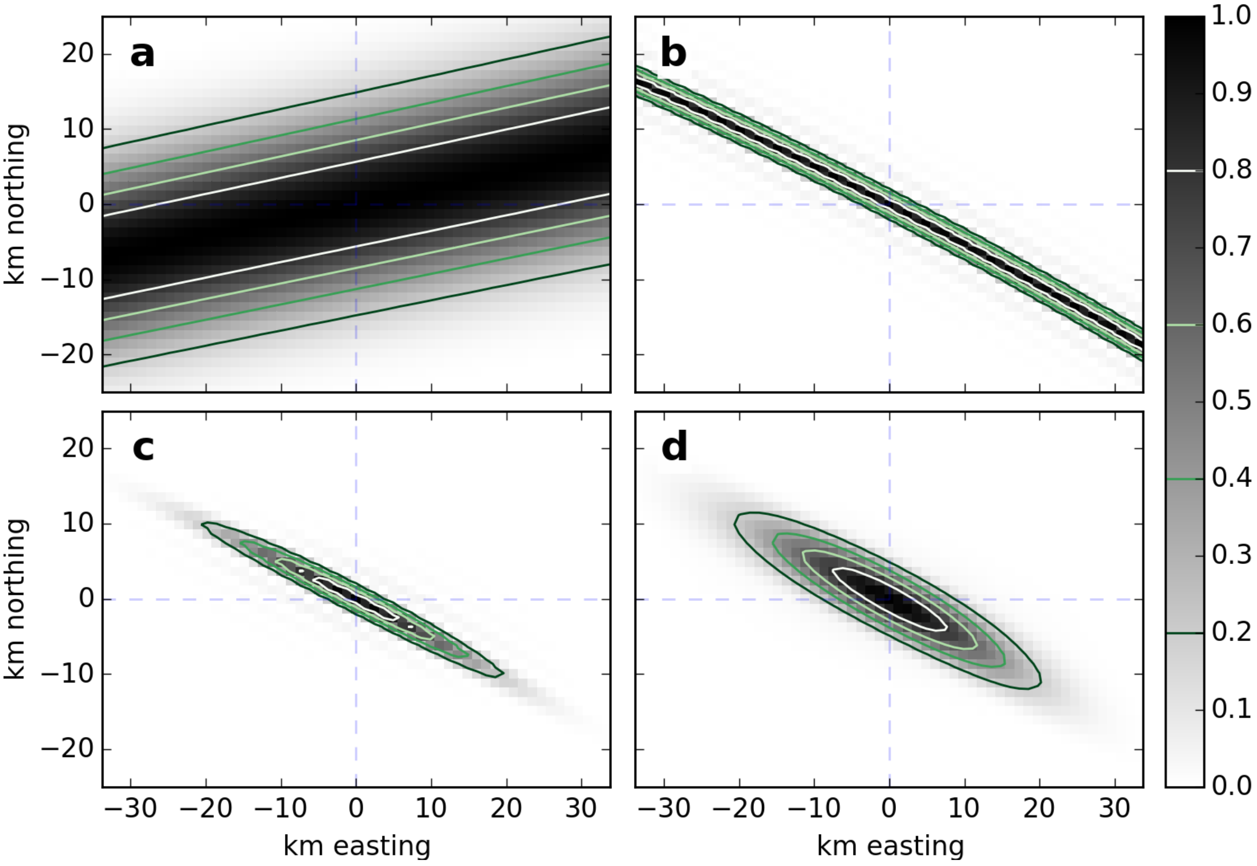

Figure 3.4: The SRF is progressively built up by including various components: (a) the cross-beam antenna response, (b) the range-Doppler response for a single FFT bin, (c) the pulse SRF, and (d) the full SRF. The SRF shown is for the measurement with parameters given in Table 3.2.

5. Multiply the x and y response values together to obtain the SRF value

The rotation angle ψ is a function of latitude, but it may be decomposed into constituent angles:

$$\psi = (-\varphi) + \beta + \alpha, \tag{3.2}$$

where ψ is the angle from northing to the discriminator frequency gradient, φ is the rotation angle from along-track to northing, β is the rotation angle from along-track to along-beam, and α is the angle from along-beam to the discriminator frequency gradient. The angles φ

Table 3.3: The angles β and φ for the six ASCAT beams. β is the angle between along-beam and along-track, and φ is the angle between along-track and northing. The angle ϕ is the azimuth angle reported in the L1B data.

Beam	β	φ
1	45°	$\phi - 135°$
2	90°	$\phi - 90°$
3	135°	$\phi - 45°$
4	−45°	$\phi + 135°$
5	−90°	$\phi + 90°$
6	−135°	$\phi + 45°$

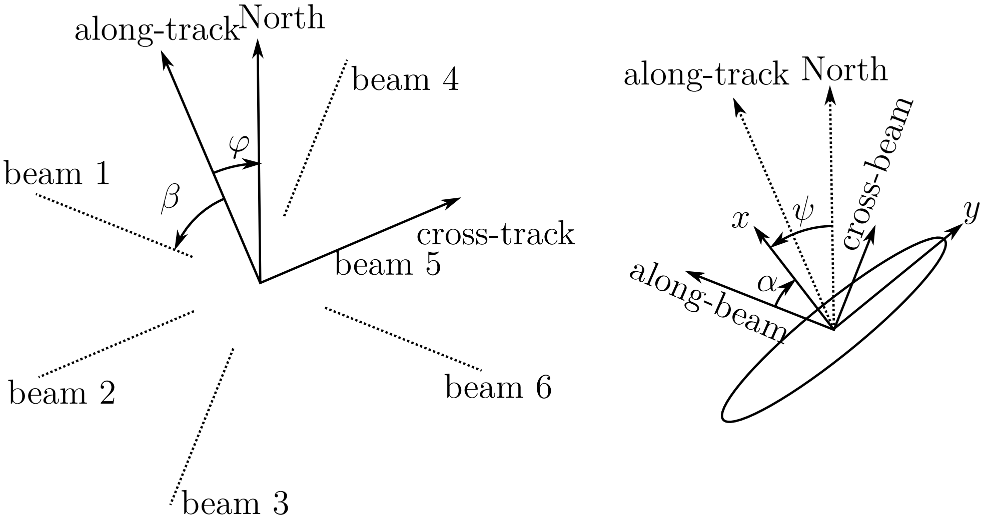

Figure 3.5: Left: the rotation angles φ and β for beam 1. Right: the rotation angles α and ψ for beam 1. The ellipse represents the parameterized SRF.

and β are functions of beam geometry and are defined in Table 3.3. Figure 3.5 illustrates the rotation angles. In all cases, the angles are defined such that positive values are in the counter-clockwise direction.

The angle ψ is obtained directly in the reference SRF computed in Section 3.1 by computing the gradient of the computed discriminator frequencies on the tangent plane grid. At high latitudes, ψ rapidly varies due to φ, the angle between along-track and North. However, α is much more stable as a function of latitude, so it is parameterized rather than ψ. The remaining components of ψ—β and φ—are only a function of the beam number and azimuth angle so are not parameterized.

The angle α follows a surface as a function of measurement node and latitude. (The measurements along each beam are indexed by node.) An example is shown in Fig. 3.6. A fourth-order polynomial surface is fit individually for each of the six beams, and separately for ascending and descending passes. The α parameterization is

$$\alpha(n, l; b, a) = c_{00} + c_{01}n + c_{02}n^2 + c_{10}l + c_{11}nl + \cdots + c_{44}n^4l^4, \tag{3.3}$$

where n is the node number, l the latitude, b the beam number, and a is ascending or descending. For each combination of b and a, $(4+1)^2 = 25$ coefficients are required. With six beams ($b \in \{1, \ldots, 6\}$) and two cases for ascending/descending ($a \in \{0, 1\}$), there are twelve sets of coefficients, or 300 total coefficients, to parameterize α.

The coefficients are determined by computing the reference SRF estimate described in Section 3.1 for a large number of ASCAT measurements, randomly distributed in latitude and node. The angle α is computed for each measurement and the data is fit in the least-squares sense to solve for the coefficients. For about 190 000 measurements per combination of beam and ascending/descending pass, the R^2 coefficient of determination is greater than 0.99 in all cases. Such a high value indicates the polynomial model chosen nearly perfectly describes the data.

The SRF response values in the x and y directions may be modeled by a Gaussian fit. However, to reduce the model error while retaining a simple parameterization, I describe here a polynomial fit to the SRF response. A low-order polynomial fits the SRF mainlobe more closely in dB space than linear space. The polynomial fit is constrained so it only fits the mainlobe down to −15 dB in order to avoid fitting the “ripples” in the mainlobe. A biquadratic fit is applied, or a fourth-order polynomial fit with the odd terms set to 0 to enforce symmetry:

$$\mathrm{SRF}_x(x; \ldots) = a_0 + a_2x^2 + a_4x^4 \tag{3.4}$$

$$\mathrm{SRF}_y(y; \ldots) = b_0 + b_2y^2 + b_4y^4, \tag{3.5}$$

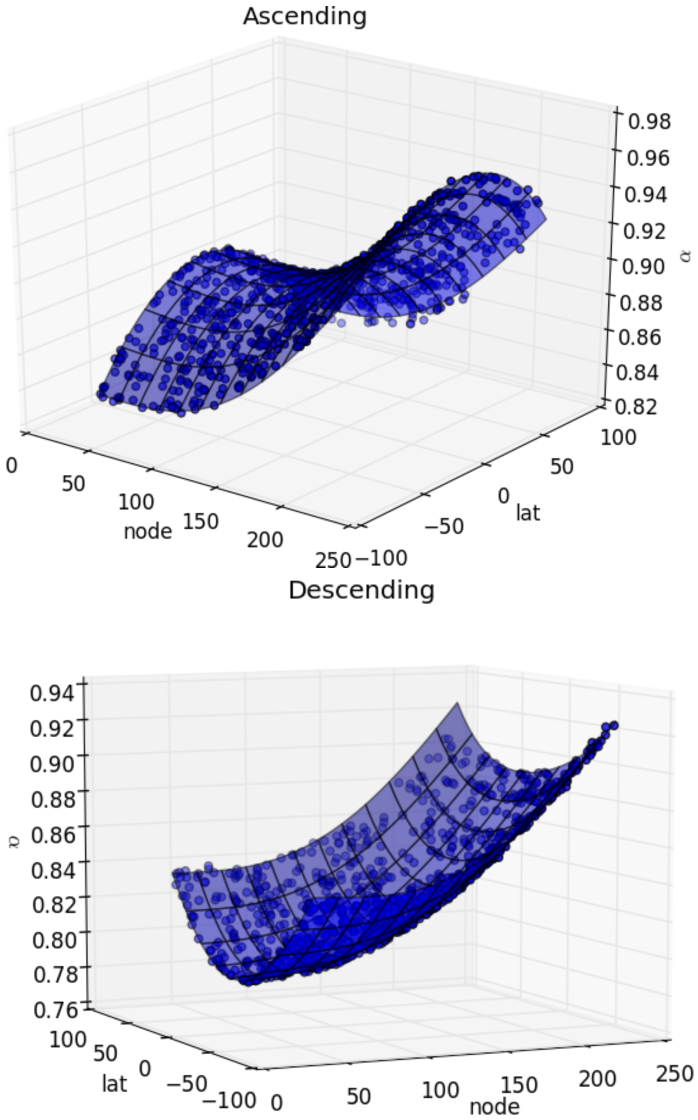

Figure 3.6: The angle α, in radians, is shown as a function of node and latitude for the right aft beam for both ascending and descending passes. The points shown are a subset from 5 days of ASCAT data. The surface, a fourth-order polynomial described in the text, is fit to the points.

where x and y are in units of km from the center of the locally tangent plane. A sample SRF response and the polynomial fit are shown in Fig. 3.7.

Equations (3.4) and (3.5) model the SRF response. The coefficients are, as with the angle α, functions of node, latitude, beam, and ascending/descending pass. A polynomial surface is fit to each coefficient as a function of node and latitude. However, unlike for α, only a second-order polynomial surface is required. For example, for the a_0 coefficient

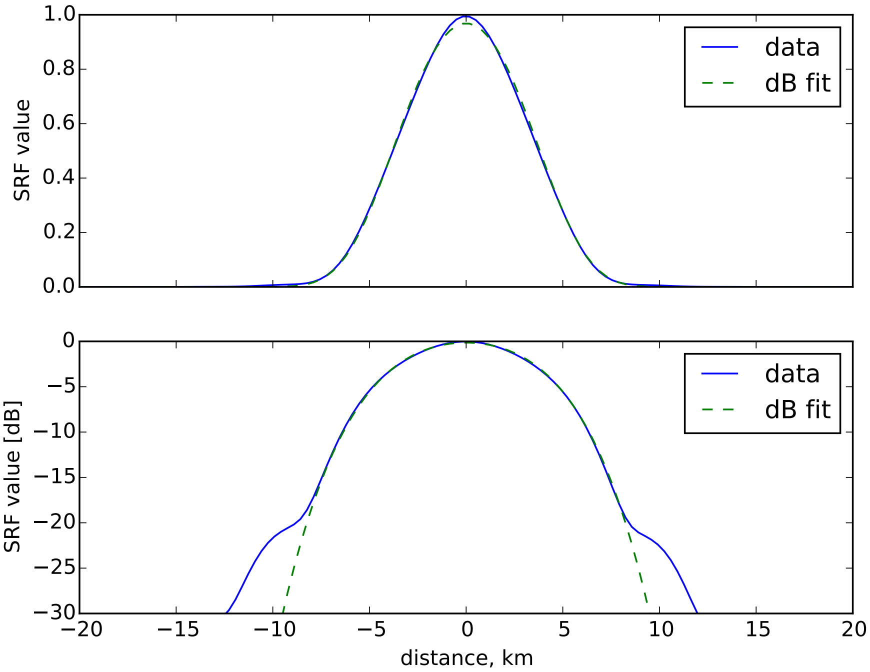

Figure 3.7: The SRF values along the x axis for a measurement from beam 3. The upper subplot shows the values in linear space, and the lower subplot shows the values in dB space. A biquadratic fit in dB space is applied to the data down to $-15\,\mathrm{dB}$.

from Eq. (3.4),

$$a_0(n, l; b, a) = a_{00} + a_{01}n + a_{02}n^2 + a_{10}l + a_{11}nl + \cdots + a_{22}n^2l^2. \tag{3.6}$$

For each of the six coefficients from Eqs. (3.4) and (3.5), there are $(2+1)^2 = 9$ coefficients. As with α, the fits are separately performed by beam and ascending/descending pass, for twelve cases. Thus $6 \times 9 \times 12 = 648$ coefficients are used to parameterize the SRF response in the x and y directions.

The parameterized SRF is much less computationally demanding than the reference estimate from Section 3.1. For a typical use case of evaluating a measurement SRF value at 100 locations, the time is benchmarked on a computer at 19.61 ms for the reference SRF estimate, and 0.1048 ms for the parameterized SRF estimate.

This decrease in runtime by two orders of magnitude does not appreciably affect the accuracy of the SRF estimate. Comparison plots for the reference and parameterized SRF estimates are shown in Figs. 3.8 and 3.9 for a side and mid beam, respectively. The

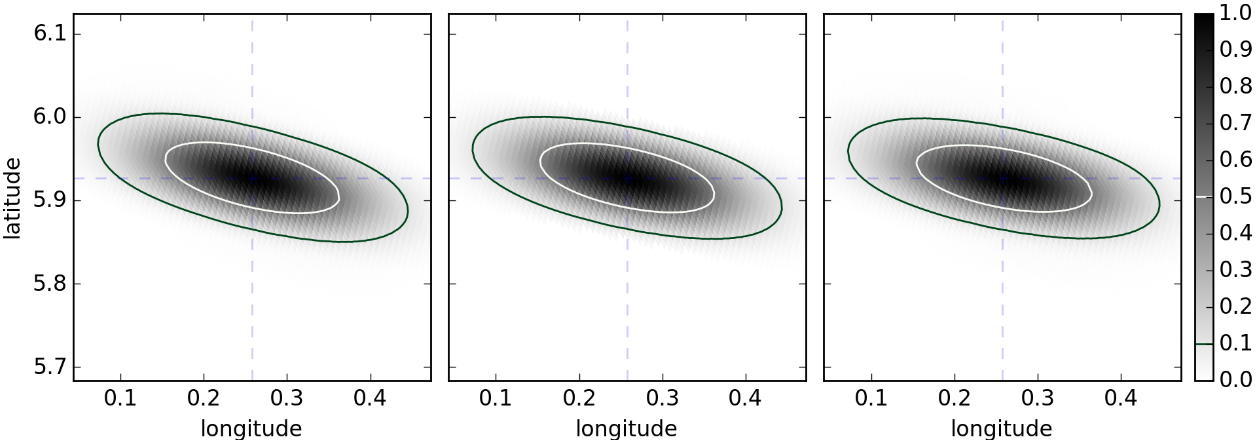

Figure 3.8: The reference (left) and parameterized (center) SRF estimates and the PPF SRF (right) for a measurement in the left fore beam.

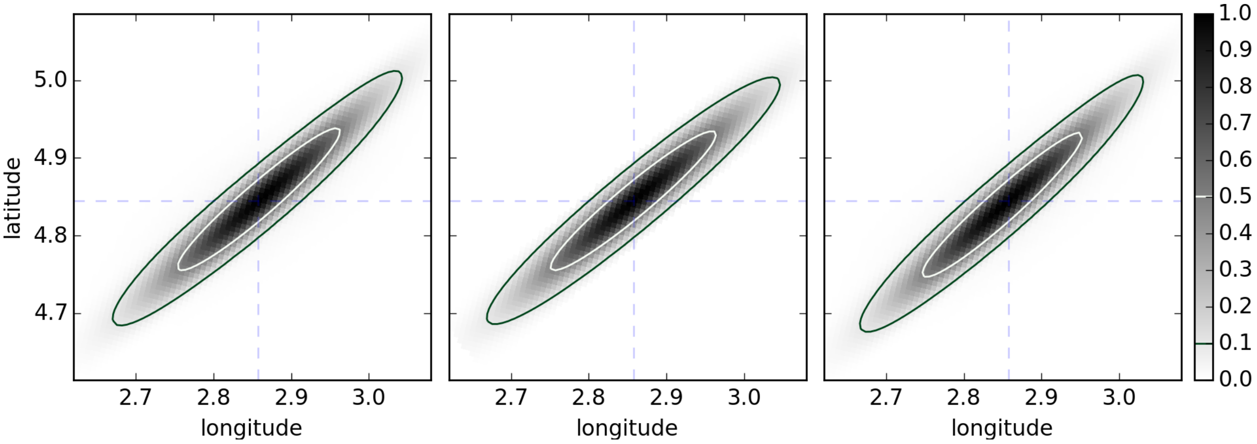

Figure 3.9: The reference (left) and parameterized (center) SRF estimates and the PPF SRF (right) for a measurement in the left mid beam.

estimated SRF values are very similar for the two estimates. The largest differences are for measurements with low incidence angles in the mid beams. In these cases, the reference SRF curves slightly, deviating from the ellipse model. Since the difference is small, and in the interest of a simple parameterization, the curvature is not accounted for.

My parameterized SRF estimate is publicly available,[1] including the coefficients for the polynomial fits.

---

[1] `http://www.scp.byu.edu/software/ASCAT`

3.3 SRF Validation

The SRF estimates from Sections 3.1 and 3.2 may be validated using several techniques. Two methods are comparing the estimates with the SRF model used during the ground processing of the raw data from ASCAT and comparing the SRF estimates against the spatial signal seen in the transponder data collected for the external calibration of ASCAT. These validation methods are conducted by EUMETSAT and are detailed in [63]. Because the methods are not my work, I do not detail them here. However, the SRF model used during ground processing at the EUMETSAT PPF may be seen in Figs. 3.8 and 3.9 along with both the reference and parameterized SRFs. All three SRF models agree well, although they are not identical—some small error is expected due to approximations undertaken to create a simple model and parameterization of the SRF.

A final validation method, which I implement based on an observation from Craig Anderson of EUMETSAT, is shown in this section: observed features in the ASCAT σ° data are consistent with those predicted by the SRF estimates. Generally, the σ° values for land and vegetation are larger than for the open ocean. I select a study region that includes the island of Niue (19.06° S 169.87° W) in the Pacific Ocean. When the wind speeds are low, the large σ° values from the island provide an excellent contrast against the low σ° values of the surrounding ocean.

Due to the distributed nature of the SRF, measurements over the ocean but near Niue contain a combination of the true ocean σ° and the land σ°. Thus some "blurring" in the σ° data is expected around Niue. Due to the elliptical shape of the SRF, the blur is larger along one direction (oriented along the semi-major axis of the SRF ellipse) than the perpendicular direction (oriented along the semi-minor axis of the SRF ellipse).

Niue is shown for geoprojected ASCAT backscatter in the upper left subfigure of Fig. 3.10. The GSHHG[2] coastline is overlaid on the σ° values. A few 3 dB contours of the measurement SRF are shown for scale and orientation. As expected, the σ° values near Niue are "blurred" in the orientation of the SRF semi-major axis.

To illustrate the significance of inaccuracies in the SRF estimate, a synthetic σ° scene is created for the Niue region where land (the area within the Niue coastline) is set to

---

[2] `http://www.soest.hawaii.edu/pwessel/gshhg/`

-10 dB and ocean is set to -20 dB. The synthetic scene is sampled with three different SRF estimates: (1) a circular Gaussian with a -3 dB width of 25 km, (2) an early SRF estimate from [24] that incorrectly assumes a rectangular shape perpendicular to the beam, and (3) the parameterization from Section 3.2. The sampled σ° values are shown in the remaining subfigures of Fig. 3.10 along with the SRF 3 dB contours for a few measurements. Of the three SRF types, only the estimate presented in this chapter enables synthetic σ° measurements that match the observed values.

In all cases observed, the blurred backscatter matches the orientation of the SRF estimate, and I conclude that the SRF as described here accurately models the characteristics of the ASCAT NRCS measurements.

3.4 Conclusion

The ASCAT SRF is a quantity that characterizes the spatial extent and weighting of each ASCAT σ° measurement. I model the SRF using the viewing geometry, antenna gain patterns, and details of the ASCAT onboard processing. I also present a computationally efficient SRF estimate that parameterizes the SRF based on measurement latitude and cross-swath position.

The modeled and parameterized SRF are both constructed to only require quantities reported in the ASCAT L1B data product. This avoids considerations such as orbit propagation and does not depend on quantities only reported in the lower-level data such as measurement slant ranges.

I validate the modeled SRF by observing the features in ASCAT σ° data. The observed features match the behavior predicted due to the SRF. In collaboration with EUMETSAT I have also validated the SRF through comparison with the internal EUMETSAT SRF model and through transponder data [63]. Subsequent chapters of this dissertation utilize the parameterized SRF as presented here.

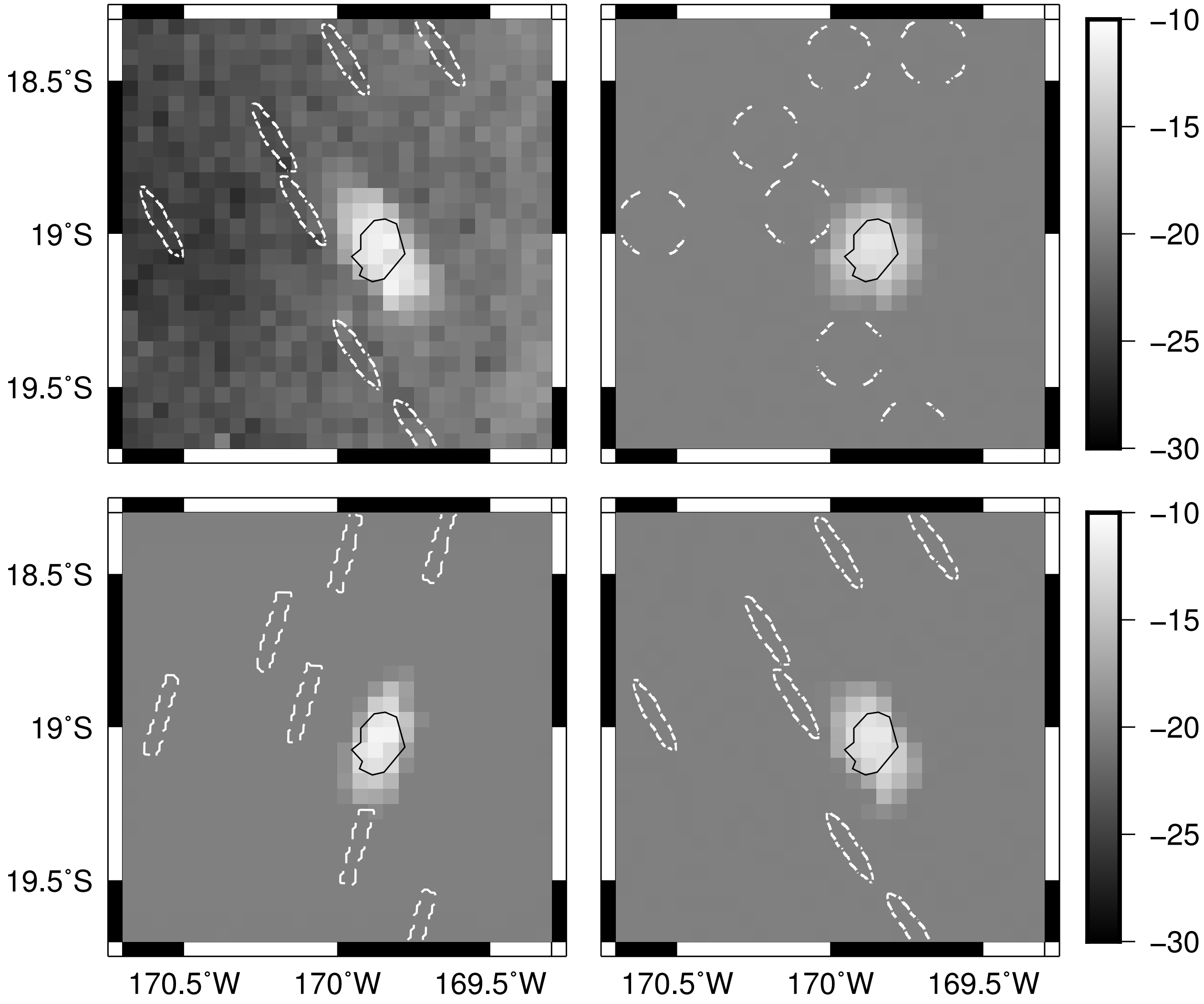

Figure 3.10: ASCAT σ° measurements near Niue for the right mid beam on a grid spacing of 0.05° ($\approx 6\,\text{km}$). The coastline of Niue is overlaid using a black line and the SRF 3 dB contour for some measurements are indicated with white dashed lines. The top left subplot is the observed σ° measurements; the remaining subplots are synthetic values sampled with different SRF estimates. Top right: a 25 km Gaussian SRF; bottom left: an SRF that is perpendicular to the along-beam direction; bottom right: the parameterized SRF described in Section 3.2.

Chapter 4

Enhanced Resolution Backscatter Reconstruction

The reconstruction of the Earth surface σ° from ASCAT measurements is discussed in this chapter. The GRD, AVE, and SIR algorithms discussed in Section 2.3 are applied to ASCAT data in conjunction with the parameterized SRF from Chapter 3.

The σ° data is produced on a high-resolution grid. The optimum grid spacing is first considered in Section 4.1, along with the theoretical spatial resolution of ASCAT data. Other parameters for the reconstruction algorithms are discussed in Section 4.2. Resulting images of the reconstructed backscatter are shown in Section 4.3. First- and second-order statistics of the GRD, AVE, and SIR algorithms are compared in Section 4.4. A basic spectral analysis of GRD, AVE, and SIR using ASCAT data is conducted in Section 4.5 in order to evaluate the effective resolution of the output images. Section 4.6 concludes this chapter.

4.1 Spatial Resolution

In this section I address the question of spatial resolution in order to determine an appropriate grid spacing for the reconstructed σ°. As depicted in Fig. 2.3, image reconstruction operates on the irregularly sampled input data to produce a regularly sampled digital image. Both the input (ASCAT σ° measurements) and output (reconstructed σ° image) are samples of the same underlying signal—the Earth surface radar reflectivity $\sigma^\circ(x, y)$—but may have different notions of resolution.

Sampling theory dictates that, under approximate conditions, a bandlimited signal may be sampled such that the samples completely represent the signal. The classic case of a band-limited regularly sampled signal is governed by the Nyquist criterion—the samples perfectly represent the signal if the sampling frequency is at least twice the signal bandwidth.

Since the output σ° image is a regularly sampled signal, due to the Nyquist criterion, the spatial resolution of the image is at least twice the sample period, or pixel size. Thus the output image has a *pixel resolution* determined only from the pixel size. This differs from the *effective resolution*, which is determined by the input data and the reconstruction algorithm. To avoid aliasing, the pixel resolution must be equal to or finer than the effective resolution. For simplicity, I use square pixels so the pixel resolution in the x direction is the same as in the y direction.

It is important to choose an appropriate pixel size, or grid spacing, for the output image. Choosing a smaller pixel size increases the storage requirements and computation time of the image reconstruction. A smaller pixel size than is necessary provides no benefit to the image effective resolution. Choosing a larger pixel size leads to aliasing of the signal and a loss of effective resolution. Since the image reconstruction also evaluates the measurement SRF on the pixel grid (h_{ij} in Eqs. (2.26) and (2.27)), an additional constraint is that the pixel size adequately samples the SRF values. Thus the choice of pixel size is motivated by computational cost and SRF quantization, in addition to the effective resolution of the image.

The image reconstruction algorithm ideally preserves the effective resolution of the input data. It is difficult to exactly quantify the effective resolution of ASCAT σ° samples. The frequency response of the underlying σ° signal, the sampling geometry, and the measurement SRF all may vary the effective resolution.

Because the input data consists of irregularly sampled aperture-filtered measurements, the conditions of classic sampling theory are too restrictive for ASCAT and other scatterometers. It has been shown [29, 64] that, analogous to the Nyquist criterion

$$T_s < \frac{1}{2B} \tag{4.1}$$

for a signal bandlimited to $[-B, B]$ and sampled regularly with period T_s, an irregularly sampled signal with frequency extent $[-B, B]$ must satisfy

$$\delta < \frac{\ln 2}{2B} \tag{4.2}$$

in order to be fully represented by its samples. The parameter δ is the maximum sample spacing. A spatial region is said to be δ-dense if the union of all rectangles with width δ centered on each measurement completely fills the region [64]. Further details on irregular sampling are discussed in Appendix A.1.

Whatever the true bandlimit of the signal, given irregular samples with a density of δ, Eq. (4.2) dictates the recoverable bandlimit. The signal, if bandlimited, may or may not be aliased. If the signal is not bandlimited, then it is certainly aliased. However, a bandlimited signal implies the signal has infinite extent in the spatial domain. Since the true σ° signal is finite in extent, it cannot be purely bandlimited. However, it is treated as *approximately* bandlimited.

The justification for treating σ° as approximately bandlimited is due to its behavior: radar reflectivity is a physical process with a power-law relationship that results in a red spectrum—that is, the power density is inversely proportional to frequency. Although the true σ° signal has high-frequency content that is aliased due to sampling, the energy in this portion is minimal for a suitably chosen sample frequency. Additionally, since the aperture functions that sample the σ° signal are generally lowpass, they further suppress the high-frequency energy so that the aliased energy can be ignored. Note that because of the filtered or ignored high-frequency content, the reconstructed enhanced-resolution image is a bandlimited version of the true continuous signal $\sigma^\circ(x, y)$.

I thus treat Eq. (4.2) as satisfied for the available sampling—that is, the σ° samples have a δ-density sufficiently large to represent the σ° signal bandlimited to B, as determined by Eq. (4.2). In order for the pixels of the output image to represent this bandlimited signal, Eq. (4.1) must be satisfied. Since Eq. (4.2) is assumed satisfied, I combine them to yield

$$T_s < \frac{\delta}{\ln 2}. \tag{4.3}$$

This represents the largest pixel size, T_s, that can represent the bandlimited signal, which is irregularly sampled at a density of δ. Since Eq. (4.3) implies no aliasing of the irregularly sampled signal, the effective resolution is the same as (or more coarse than) the pixel resolution. As stated above, the pixel resolution is $2T_s$. Thus from Eq. (4.3) the best-case effective

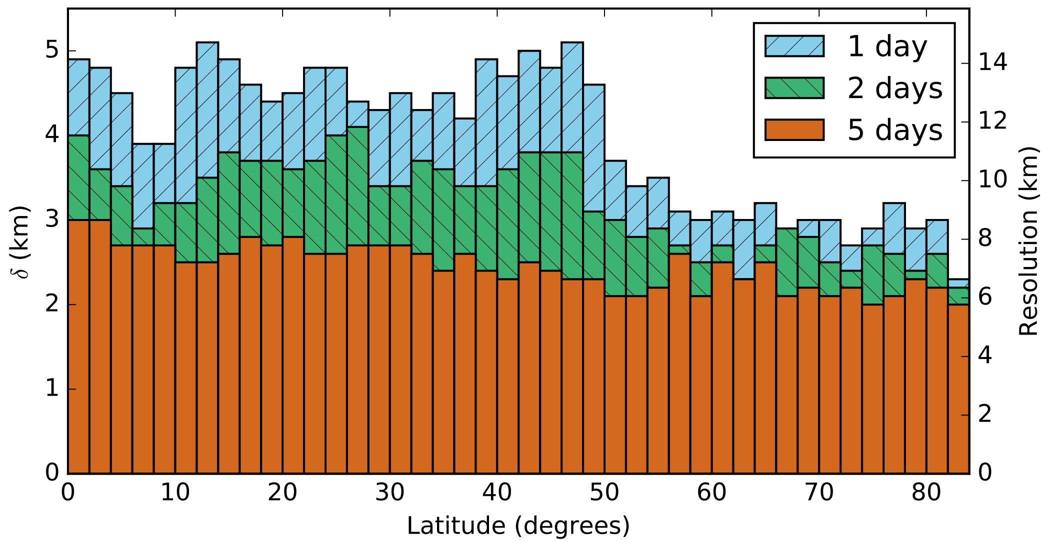

Figure 4.1: The sample density δ as a function of latitude for bins of latitude using 1, 2, and 5 days of ASCAT data. The smallest spatial resolution that may be reconstructed is also indicated.

resolution may be computed directly from δ: $\frac{2\delta}{\ln 2}$. Note that due to the frequency response of the aperture functions used to sample the signal, the effective resolution may be worse than that determined solely by δ.

The parameter δ is intrinsic to the observation geometry and sample spacing. A simple estimate for δ is found through binning the measurements over a region at various grid sizes. The smallest grid size with no empty bins is the estimated δ. For ASCAT, using only one beam from a single pass of data yields the largest nominal δ: approximately 5.25 km. From this single-pass single-beam δ, the worst-case effective resolution is therefore 15.15 km. Combining all beams and using multiple passes reduces δ, but this is a function of latitude: due to the near-polar orbit, locations at high latitudes are sampled more densely than those closer to the equator. The density δ and effective resolution are shown in Fig. 4.1 as a function of latitude using 1, 2, and 5 days of data. The average δ for equatorial and for polar regions is displayed in Table 4.1. The theoretical spatial resolution that may be reconstructed in these cases is also shown.

For compatibility with existing SCP datasets, I choose a pixel size of $8.9\,\text{km}/2 = 4.45\,\text{km}$ in order to avoid aliasing. This pixel size is slightly smaller than the pixel sizes of

Table 4.1: The average δ and corresponding spatial resolution from Fig. 4.1 for equatorial ($< 50°$) and for polar ($> 55°$) latitudes.

	Equatorial latitudes		Polar latitudes	
Days	δ (km)	Resolution (km)	δ (km)	Resolution (km)
1	4.6	13.3	3.0	8.5
2	3.6	10.3	2.6	7.4
5	2.6	7.5	2.2	6.4

4.6 km or 5.6 km required to represent 9.2 km or 11.5 km resolution data from the 5-day or 2-day δ values.

As part of AVE and SIR reconstruction, the SRF is quantized or sampled on the same grid used to reconstruct the $\sigma°$ data. The chosen pixel size of 4.45 km is on the order of the width of a measurement SRF. While this coarse quantization of an SRF is not a particularly accurate representation of the SRF, no issues are apparent in the final reconstruction output using this coarse representation over a more finely quantized version using a smaller pixel size.

For comparison purposes in this dissertation, I also consider a reconstruction pixel size of 3.125 km for a pixel resolution of 6.25 km. To match the resolution of the spatially averaged ASCAT data, which are produced at 25 km and 50 km resolution [26], I create conventionally gridded $\sigma°$ images on a grid spacing of 12.5 km and 25 km for pixel resolutions of 25 km and 50 km. The alternate pixel size of 3.125 km for the reconstructed images permits an easier comparison between the gridded versus the reconstructed images since the gridded pixel sizes are an integer multiple of the reconstructed pixel size. Thus for AVE and SIR I use a grid spacing of 3.125 km, and for GRD I use both 12.5 km and 25 km.

4.2 Reconstruction Parameters

I consider three reconstruction parameters for ASCAT: (1) the pixel size; (2) the number of SIR iterations; and (3) quantization of the SRF estimate. The choice of pixel size, or posting grid, is discussed above in Section 4.1. In this section, I evaluate the other two parameters.

Since SIR is an iterative algorithm, the number of SIR iterations is a parameter that affects the final reconstruction output—prematurely terminating the SIR iterations is a regularization that results in a partial reconstruction. This parameter controls a tradeoff between the image fidelity and the noise added or amplified during the reconstruction process. The number of iterations can be fixed or chosen dynamically, e.g., by terminating if the change in image values as a function of iteration falls below some threshold. Here, I select a fixed value for the number of iterations.

The SRF may be quantized in order to reduce computation. The quantized, or binary-valued, SRF is an approximation to the true, or full-valued, SRF $h_i(x, y)$, which is 1 inside the SRF 3 dB contour and 0 outside. A quantized SRF was previously used for QuikSCAT slice measurements to reduce computational complexity [5]. I evaluate this approach for the ASCAT SRF by reconstructing with both the original SRF and the quantized SRF.

I use simulations to select both the number of SIR iterations and choose between a full-valued or binary-valued SRF by minimizing the error metrics defined below. A synthetic "truth" image of $\sigma^\circ[x, y]$ is created and sampled using ASCAT measurement geometry and the full-valued SRF estimate. Using Eq. (2.17), the synthetic ASCAT measurement σ_i° is expressed as

$$\sigma_i^\circ = \frac{\sum_j \sigma_{\mathrm{true},j}^\circ h_{ij}}{\sum_j h_{ij}}, \tag{4.4}$$

where j indexes the pixels of the true σ° image, i indexes the measurements, and h_{ij} is the full-valued SRF value of measurement i at pixel j. Note that the evaluation of SRF quantization is a reconstruction-only parameter, so a quantized SRF is not appropriate for the sampling procedure. Measurement noise is additionally simulated using Eq. (2.19), with $\nu_i \sim \mathcal{N}(0, 1)$ and $K_p = 0.20$:

$$z_i = \sigma_i^\circ (1 + K_{p,i}\, \nu_i). \tag{4.5}$$

Both noisy and noise-free samples of the synthetic image are processed using AVE and SIR reconstruction as well as the traditional GRD method ("drop-in-the-bucket"). AVE and SIR are produced at a grid spacing of 3.125 km and GRD is produced at grid spacings of 12.5 and 25 km. Reconstruction is performed using either full-valued or binary-valued SRF estimates and for various iterations of SIR. The reconstruction error is quantified by evaluation of the difference between the reconstructed $\widehat{\sigma^\circ}[x,y]$ results and the input synthetic image $\sigma^\circ[x,y]$.

For this section, the *signal error* is defined as the standard deviation of the difference between the synthetic truth image and the reconstructed output when using noise-free samples. It is the difference between the actual scene and the reconstructed scene in the ideal sense, i.e., with no measurement noise. I also define the *noise error* as the standard deviation of the difference between reconstruction outputs when using noise-free versus noisy synthetic measurements. This represents the error due only to the measurement noise. As SIR iterates, the reconstruction amplifies the noise error as it reduces the signal error. The objective of the simulation is to find an optimum number of SIR iterations such that these two error metrics are jointly minimized, as well as to evaluate the effect of SRF quantization on the signal and noise errors [29].

A parametric plot of signal error and noise error as a function of SIR iteration is shown in Fig. 4.2 for the truth image using the full-valued and the binary-valued SRF to reconstruct. Since the partial reconstruction process is not a linear operation, the error values depend on the truth image chosen. However, the general trend is similar among the various truth images evaluated: the first few iterations of SIR rapidly reduce the signal error at the expense of additional noise. After about 10 iterations, the signal error continues to decrease, but the increase in noise error is less dramatic. After about 30 iterations, any further reduction in signal error is small, but noise error slowly continues to increase. The decrease in signal error indicates resolution enhancement via improved signal reconstruction.

When using the quantized SRF, AVE has a slightly lower signal error but larger signal error than with using the original SRF. However, as SIR iterates, the full-valued SRF permits a greater reduction in signal than with the binary-valued SRF. Although exact values vary as a function of input truth image, the trend is similar for all cases tested: a quantized SRF may improve AVE, but it limits the performance of SIR.

The error for GRD at both grid spacings is also shown in Fig. 4.2. The noise error is very low, but the signal error is larger than for AVE or SIR. This illustrates an important tradeoff in enhanced-resolution image reconstruction: the signal error is improved at the

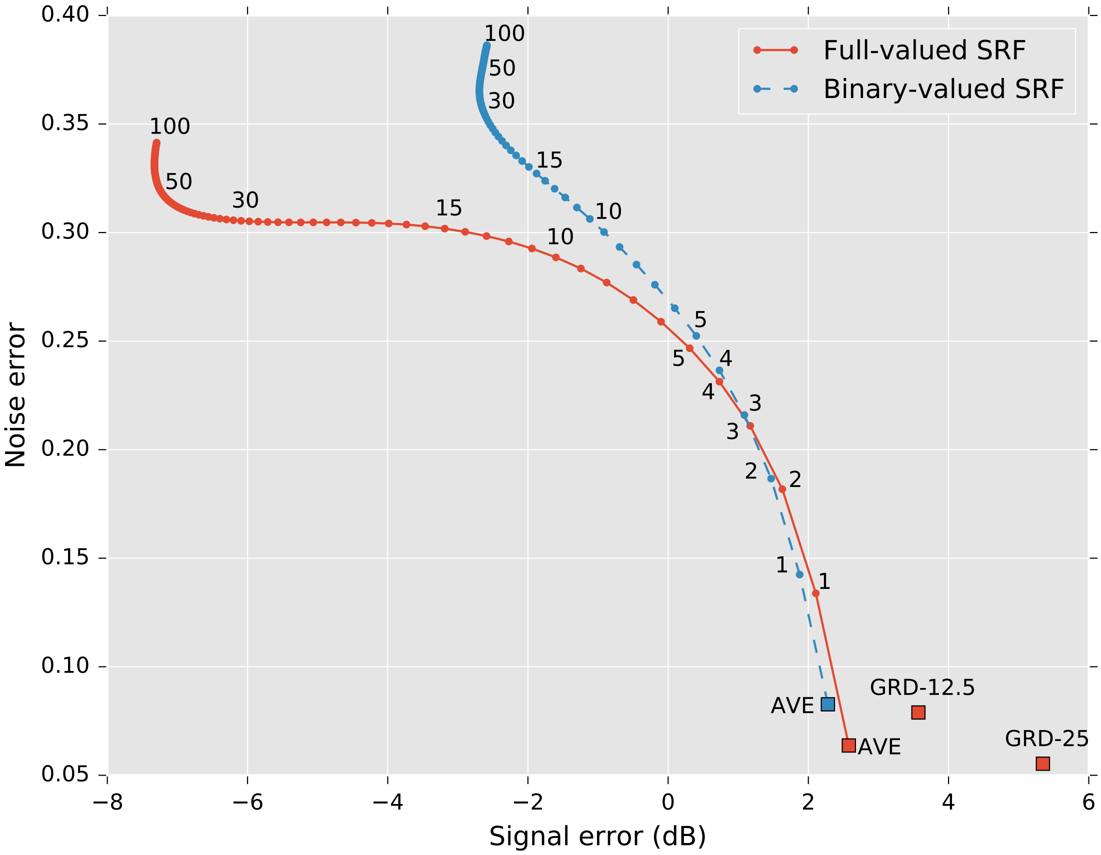

Figure 4.2: The noise error versus signal error for a synthetic truth image for up to 100 SIR iterations. The solid line indicates reconstruction with the full-valued SRF, and the dashed line indicates reconstruction with the binary-valued SRF. Selected iterations of SIR are labeled along with AVE and GRD.

expense of greater noise. In some applications the improved spatial resolution may not justify the additional noise, but for other applications this tradeoff is acceptable.

Based on the simulation results, I use the non-quantized SRF for reconstruction and select 30 iterations of SIR. ASCAT images processed using GRD, AVE, and SIR are included in the SCP to allow users some control over the noise/resolution tradeoff.

4.3 Reconstruction Results

At the spatial resolution of ASCAT, most land regions are isotropic with respect to azimuth angle, whereas azimuth anisotropy is critical for ocean wind estimation. For land and sea ice applications of σ° data, σ° data from all azimuth angle directions are averaged together to increase the number of measurements available for reconstruction. For wind applications (see Chapter 5), each beam is separately reconstructed.

Data from multiple ASCAT orbits are used for enhanced resolution processing over land and ice. Using multiple orbits of data over a few days increases the spatial coverage and improves the measurement density. Since the tradeoff is a reduced temporal resolution, using multiple passes is best suited for areas that do not rapidly change, such as land and ice.

To illustrate the effectiveness of resolution enhancement, examples of conventional images using gridding and enhanced-resolution images using AVE and SIR are shown in this section. The gridded images are produced at pixel sizes of 12.5 and 25 km using the GRD method (referred to as GRD-12.5 and GRD-25, respectively), and the AVE and SIR images are produced at a pixel size of 3.125 km. I use the reconstruction parameters selected in Section 4.2: 30 iterations of SIR using the full-valued SRF.

Three regions in Antarctica and the Amazon, shown in Figs. 4.3 and 4.4, are selected as study regions. Because ASCAT is in a near-polar orbit, polar regions are measured more frequently than at lower latitudes. Because Antarctica is a polar region, only 9 orbits (about 15 hours) are required to completely sample the land. Sea ice extent varies as a function of time, but two days of data is a good compromise between complete land and sea ice coverage and high temporal resolution. The Amazon lies at the equator, so it represents a worst-case example of coverage. At least 22 orbits (37 hours) are required to obtain complete coverage over the land. For this region, five days of data are used.

Figures 4.5 and 4.6 show the reconstructed images for both Antarctic regions. Two days of data (299–300, 2011) are used, with $\mathcal{A}$ (incidence angle-normalized σ°) images shown. Figure 4.5 shows the Weddell Sea, with the Brunt Ice Shelf visible on the right edge. Most of the region consists of sea ice, with some icebergs visible as brighter patches. Many features are visible in all four images, but the iceberg shape and orientation are more defined in the AVE and SIR images compared to the GRD images. The smaller grid spacing of the GRD-12.5 image is an improvement over the larger spacing in the GRD-25 image, and AVE and SIR further improve on the GRD-12.5 image. SIR is similar to AVE, but the contrast between sea ice and iceberg or ice shelves is sharpened. In effect, SIR de-blurs the AVE data.

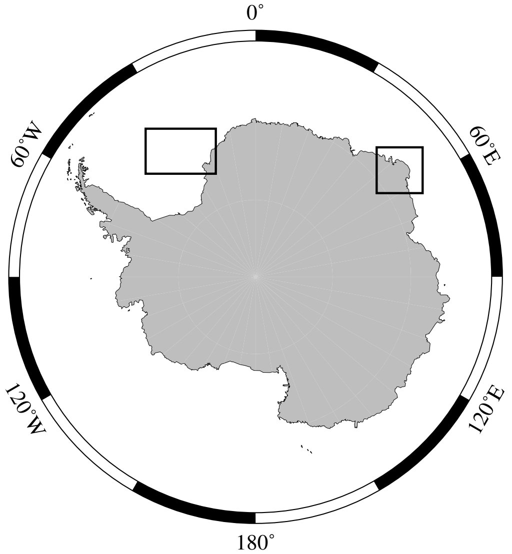

Figure 4.3: The regions of Antarctica used for Figs. 4.5 and 4.6. Figure 4.5 contains the Weddell Sea and Fig. 4.6 contains Enderby Land.

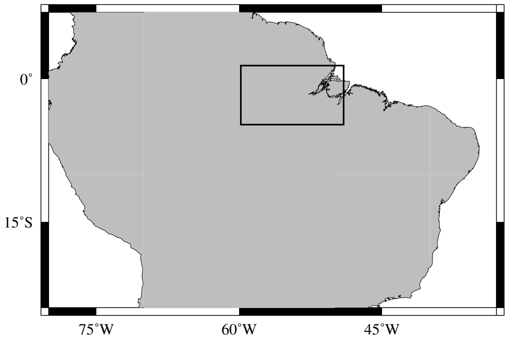

Figure 4.4: The region in South America containing the Amazon Basin used for Fig. 4.7.

Figure 4.6 contains part of Enderby Land and shows icebergs visible in the top-left and center-right of the region. The coarse grid spacing of the GRD-25 precludes the recovery of any small-scale features. With GRD-12.5, some smaller features become visible; with AVE, the size and shape of icebergs and the coastline are more clear. SIR sharpens the transition between contrasting features, such as the icebergs in the surrounding sea ice.

The Amazon Basin region is shown in Fig. 4.7. Five days of data (299–303, 2011) are used, with $\mathcal{A}$ (incidence angle-normalized $\sigma°$) images shown. The Amazon River and some of its tributaries are visible in all images. While much of the region appears homogeneous due to the high vegetation, the rivers are better resolved with AVE and SIR, with the largest

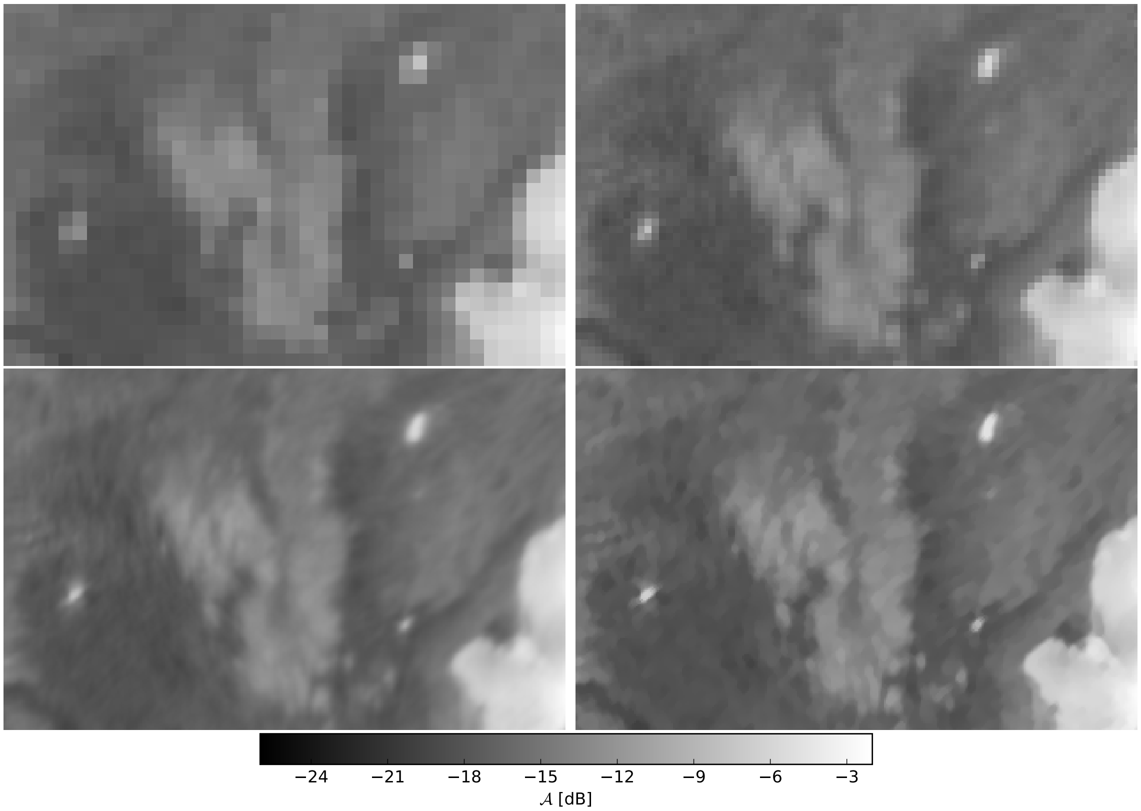

Figure 4.5: $\mathcal{A}$ images of a region from the Weddell Sea, Antarctica. Top left: gridded with a pixel spacing of 25 km; top right: gridded at 12.5 km; bottom left: AVE at 3.125 km; bottom right: SIR at 3.125 km after 30 iterations.

contrasts between land and river visible in SIR. Some image artifacts are visible in the GRD and AVE images near the center and the right. These are due to insufficient incidence angle information to estimate $\mathcal{B}$, the gradient of σ°, which leads to a poor $\mathcal{A}$ estimate.

The spatial resolution of the AVE and SIR-reconstructed data is enhanced over that of conventional GRD processing. This is demonstrated in Fig. 4.2 for a synthetic $\sigma^\circ(x, y)$ scene and visually verified in Figs. 4.5 to 4.7 for ASCAT σ° measurement data. Other regions of the Earth similarly demonstrate enhanced resolution.

4.4 Reconstruction Statistics

To quantify the performance of the reconstruction algorithms, the reconstructed data is characterized by first- and second-order statistics: the mean and variance of each pixel and the autocovariance between each pair of pixels. These statistics are used to evaluate the

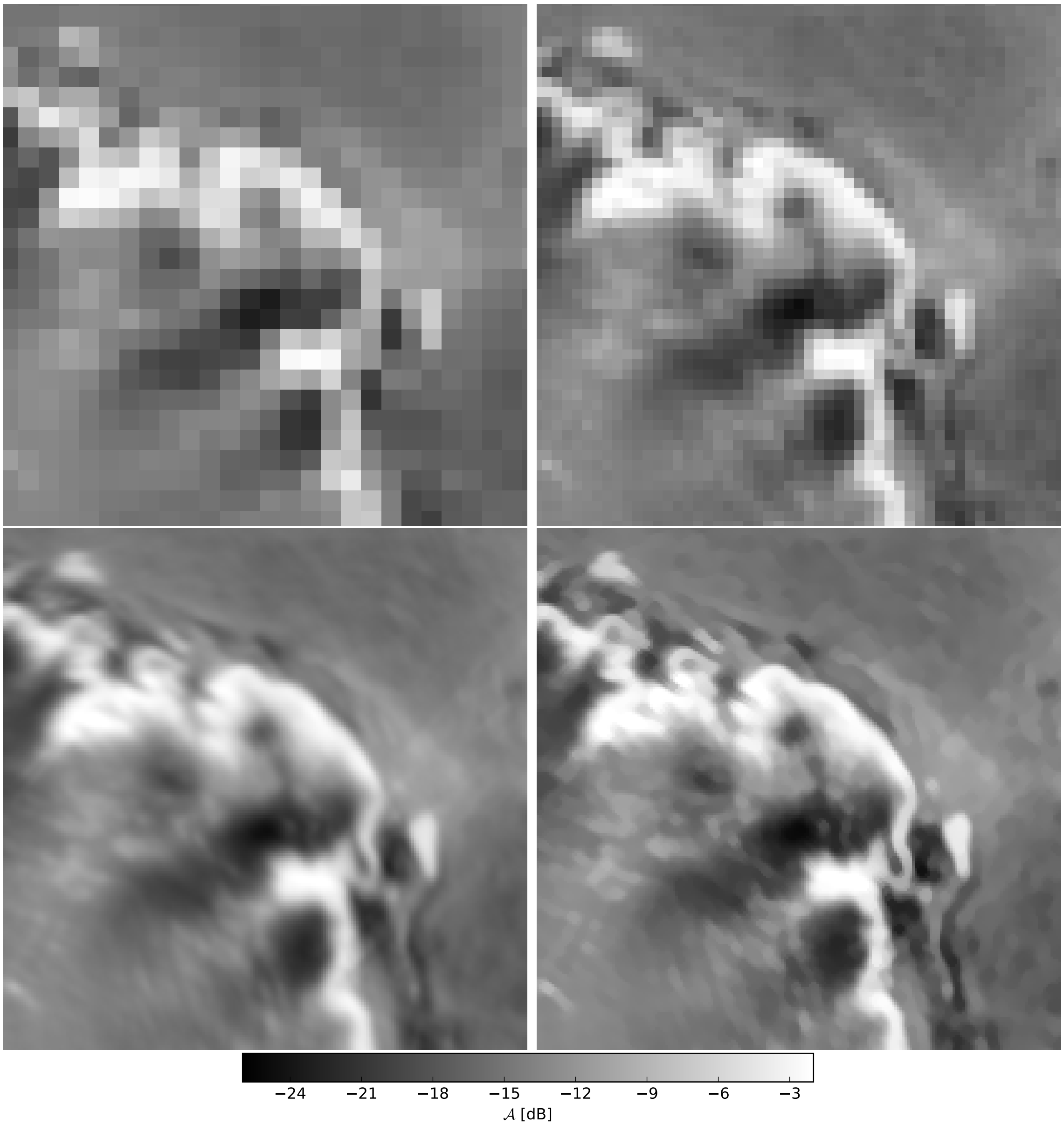

Figure 4.6: $\mathcal{A}$ images of a region from Enderby Land, Antarctica. Top left: gridded with a pixel spacing of 25 km; top right: gridded at 12.5 km; bottom left: AVE at 3.125 km; bottom right: SIR at 3.125 km after 30 iterations.

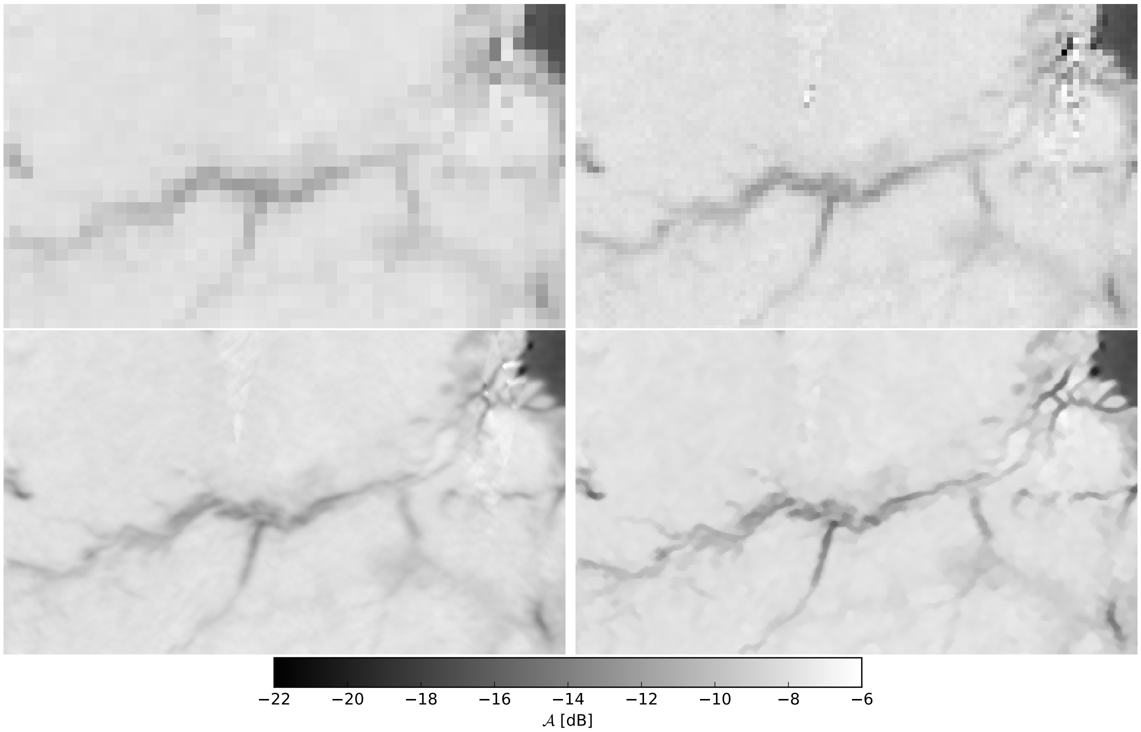

Figure 4.7: $\mathcal{A}$ images of a region from the Amazon Basin. Top left: gridded with a pixel spacing of 25 km; top right: gridded at 12.5 km; bottom left: AVE at 3.125 km; bottom right: SIR at 3.125 km after 30 iterations.

accuracy and precision of the reconstruction algorithms as applied to ASCAT. Although a full derivation of these statistics is available in Appendix C, in this section only the results and salient points are discussed.

For GRD and for AVE, I predict the mean σ° for each pixel j and the autocovariance between pixels m and n. The mean is the expected value of the pixel:

$$\mu_{\text{ave}}[j] = E[\sigma^\circ_{\text{ave}}[j]], \tag{4.6}$$

and the autocovariance is

$$k_{\text{ave}}(m,n) = E\left[(\sigma^\circ_{\text{ave}}[m] - \mu_{\text{ave}}[m])(\sigma^\circ_{\text{ave}}[n] - \mu_{\text{ave}}[n])\right]. \tag{4.7}$$

Due to the non-linear nature of the SIR algorithm, the pixel mean and autocovariance are not readily computable, so instead I use the sample mean and sample autocovariance through simulation. The sample statistics are also computed for AVE and for GRD and compared against the predicted values in order to validate the prediction. To simplify the analysis, no incidence angle dependence is included.

The simulation process includes two modeled sources of randomness: measurement noise and the uncertainty of the true Earth surface $\sigma^\circ(x, y)$. The uncertainty of the true surface is modeled as having first- and second-order statistics $\mu_A[j]$ and $k_A(m, n)$, the mean at pixel j, and autocovariance between pixels m and n, respectively. After sampling with the ASCAT measurement geometry and SRF, the ASCAT measurements z_i have first- and second-order statistics $\mu_z[i]$ and $k_z(a, b)$, the mean of measurement z_i, and the autocovariance between measurements z_a and z_b.

Measurement noise, because it is zero mean and uncorrelated, does not change $\mu_z[i]$ or $k_z(a, b)$ for $a \neq b$, but it does increase the measurement variance $\text{var}_z[i] = k_z(i, i)$. The pixel mean and autocovariance for AVE for GRD ($\mu_{\text{ave}}[j]$, $k_{\text{ave}}(m, n)$, $\mu_{\text{grd}}[j]$, and $k_{\text{grd}}(m, n)$) are related to the measurement statistics.

Synthetic truth images are generated from a mean vector and autocovariance matrix, μ_A and Σ_A. A multivariate Gaussian distribution is used with the parameters μ_A and Σ_A to obtain multiple realizations of truth images. The truth images are sampled with the SRF and the ASCAT measurement geometry over an equatorial region using 5 days of data to obtain synthetic ASCAT measurements. Noise is added to the measurements using Eq. (2.19) with a constant K_p value of 0.20. Based on the truth image statistics μ_A and Σ_A, the measurement statistics are predicted, and from those the AVE and GRD pixel statistics are predicted.

The GRD, AVE, and SIR algorithms reconstruct the output images from the noisy synthetic measurements. The reconstructed images are created for each truth realization; for the results following, 500 realizations are generated, so 500 sets of GRD/AVE/SIR images are created. The sample mean and sample autocovariance are taken over the realizations and computed independently for each image pixel.

The predicted statistics are compared against the sample statistics to validate the prediction. This is shown in Appendix C, but here only the sample statistics are shown in order to compare the performance of GRD, AVE, and SIR. A subset of the sample pixel mean and variance are shown in Fig. 4.8 for GRD, AVE, and SIR. For GRD, a grid spacing at both

12.5 km and 25 km is used. AVE and SIR are both computed on a grid spacing of 3.125 km. For comparison, the GRD pixels are upsampled appropriately to match the AVE/SIR pixel size. The pixel mean subplot of Fig. 4.8 additionally includes the truth image mean. GRD and AVE are centered around the truth image mean, but SIR has a slight bias of -0.025 dB.

The pixel variance in Fig. 4.8 is typically largest for GRD at 12.5 km, is generally less for AVE, is still less for SIR, and has the lowest pixel variance for GRD at 25 km. The GRD and AVE results are proportional to the number of measurements used to compute each reconstructed pixel. The number of measurements per pixel is shown in the bottom subplot of Fig. 4.8 for GRD and for AVE (SIR has the same number of measurements per pixel as does AVE). Even though SIR uses the same number of measurements per pixel as does AVE, the pixel variance is lower for SIR than for AVE.

The autocovariance among pixels pairs is next evaluated. To increase the clarity of the plots, the correlation coefficient is plotted rather than the autocovariance. The correlation coefficient ranges between ± 1:

$$\rho(m,n) = \frac{k(m,n)}{\sqrt{k(m,m)\,k(n,n)}}. \tag{4.8}$$

For this section, I define the *correlation area* as the area in the correlation neighborhood covered by the contour 3 dB below the peak value of 1 and the *correlation length* as the radius of the 3 dB correlation contour.

The autocovariance $k(m,n)$ and correlation coefficient $\rho(m,n)$ vary as a function of position due to the ASCAT sample geometry, including the SRF shape and orientation. The exact values differ as a function of location, but the general behavior is consistent over the image. For an example pixel from GRD (both 25 km and 12.5 km grid spacings), AVE, and SIR, the sample correlation coefficient $\rho(m,n)$ between the pixel and its neighboring pixels are shown in Fig. 4.9. The GRD pixels are upsampled to match the area in the AVE and SIR cases.

In Fig. 4.9, both GRD-25 and GRD-12.5 have a very small correlation between neighboring pixels; however, since the grid spacing is large, the resulting correlation area is also large. The correlation area for AVE is about the same as for GRD-12.5, whereas

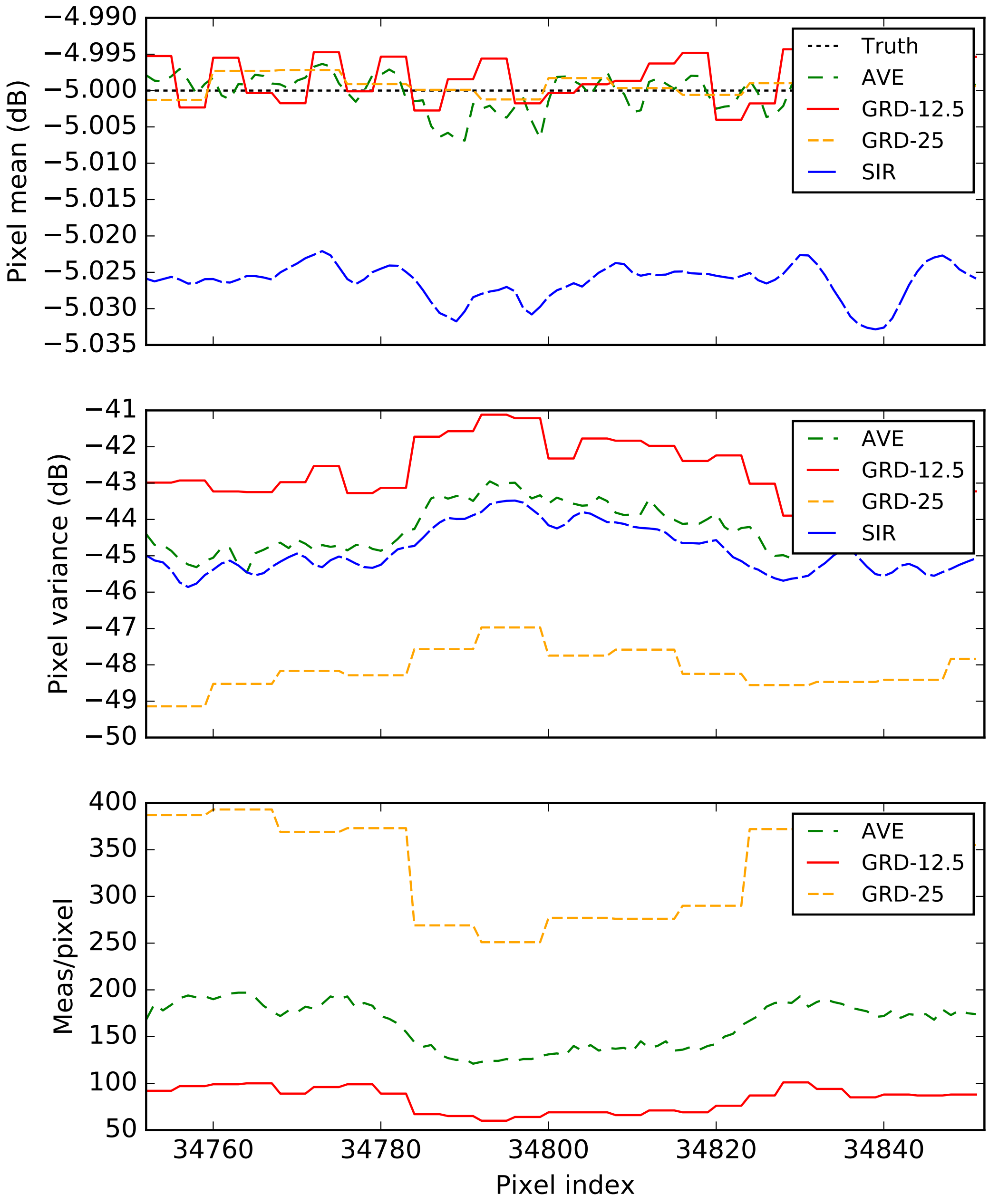

Figure 4.8: The sample mean (top) and variance (middle) for a few pixels of GRD, AVE, and SIR. GRD is computed on a grid spacing of both 25 km and 12.5 km. AVE and SIR are on a grid spacing of 3.125 km. The number of measurements used to compute each pixel (bottom) is shown for the three grid spacings.

SIR increases the correlation area beyond that of AVE. (For the pixels used in Fig. 4.9, the correlation areas for GRD-12.5, GRD-25, AVE, and SIR are: 634, 158, 175, and 314 km^2.) However, due to the measurement geometry and SRF shape, AVE typically has irregularly shaped correlation contours, while SIR smooths the contours to be more circularly symmetric—i.e., the variance of the correlation length is smaller for SIR than for AVE.

A desirable correlation coefficient area is small (so pixels are only weakly correlated with adjacent pixels) but symmetric (so the correlation distance is directionally isotropic). GRD satisfies both these conditions, but the grid spacing is large. AVE provides a smaller correlation area than GRD, but it is less symmetric than GRD. SIR tends to improve the correlation symmetry of AVE at the tradeoff of a larger correlation area.

This section has evaluated the GRD, AVE, and SIR methods by comparing the pixel mean, pixel variance, and correlation neighborhoods. Although the pixel statistics may be predicted for GRD and for AVE, in order to additionally consider SIR, the sampling process is simulated and the measured statistics are compared. As mentioned previously, because the number of SIR iterations is truncated, SIR is a partial reconstruction approach.

For the cases considered here, GRD and AVE both are unbiased while SIR exhibits a small bias. SIR, however, improves the pixel variance over that of AVE. The pixel variance of GRD depends on the grid spacing, which affects the number of measurements used for each GRD pixel. For the two cases examined (12.5 and 25 km) the GRD pixel variance is either greater than or less than that of AVE and SIR.

GRD pixels are weakly correlated with neighboring pixels, but AVE and SIR have a larger number of adjacent pixels correlated. AVE has a small correlation area, but the correlation is typically nonsymmetric. SIR improves the correlation symmetry but at the tradeoff of a larger correlation area.

4.5 Spectral Analysis

Due to measurement spacing and SRF size and orientation, the effective resolution of the reconstructed images may vary across the image. It is therefore difficult to precisely quantify the resolution of the reconstructed images as a single value. However, in order to

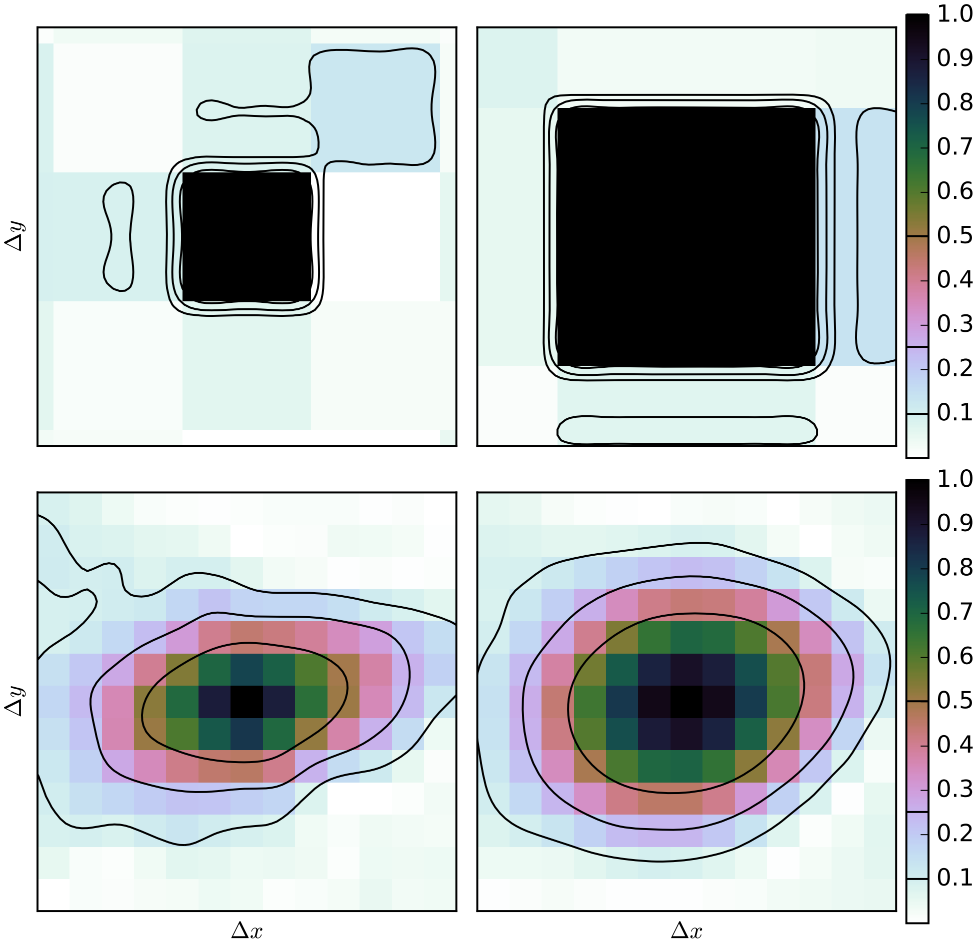

Figure 4.9: The correlation coefficient between a random pixel and its neighboring pixels for GRD at a grid of spacing of 12.5 km (top left), GRD at a spacing of 25 km (top right), AVE at a spacing of 3.125 km (bottom left), and SIR (30 iterations) at a spacing of 3.125 km (bottom right). The GRD pixels are upsampled to match the AVE/SIR grid spacing. Contours are drawn at −3, −6, and −10 dB.

determine an approximate effective resolution I conduct a basic spectral analysis on the reconstructed images.

The synthetic truth image used is shown in Fig. 4.10. It contains a linear frequency-modulated chirp in order to test a wide range of spatial frequencies. To simplify the analysis, the same values are used for each row of the synthetic truth image. The synthetic chirp image is treated as deterministic so the only uncertainty is the added measurement noise. Using an (essentially) one-dimensional truth image permits simplifying the image spectrum to

Figure 4.10: The chirp truth image used for spectral analysis.

one-dimensional as well. The image spectrum, as used here, is the row-wise power spectrum computed using Welch's method.

The spectra for GRD, AVE, and SIR are shown in Fig. 4.11. As before, grid spacings of 12.5 and 25 km are used for GRD and a grid spacing of 3.125 km is used for AVE and SIR; additionally, the ASCAT measurement geometry is from an equatorial region using 5 days of data. The spectra of the reconstructed outputs follow the behavior of the truth spectrum down to a wavenumber of about 0.01 km^{-1} (a spatial period of 100 km). Below that, AVE and GRD have similar values, but the spectra taper off. This is effectively a non-ideal lowpass filtering of the truth image. The AVE spectrum continues to decrease until high-frequency noise starts to dominate below a wavenumber of about 0.05 km^{-1} (20 km).

Although the GRD pixel resolutions for the two cases considered are 25 km and 50 km, the effective resolution of GRD is somewhat coarser than this. This is due to the SRF of each measurement not always being entirely contained in the same pixel as the measurement center. This is evident in the falling off of the GRD power spectra in Fig. 4.11 below 100 km.

The SIR spectrum in Fig. 4.11 is similar to AVE, but it successfully recovers more frequency content between wavenumbers of 0.01 km^{-1} to 0.05 km^{-1} than AVE or GRD. Similar to AVE, below about 0.05 km^{-1}, the spectrum values are larger than the truth spectrum, and the slope of the spectrum is more shallow, indicating that high-frequency noise dominates.

Figure 4.12 shows the spatial domain results, or the values of the rows of the images averaged together. Since the image is symmetric, only half of the averaged row is shown. For all reconstruction cases considered, the recovered amplitude decays as frequency increases, in

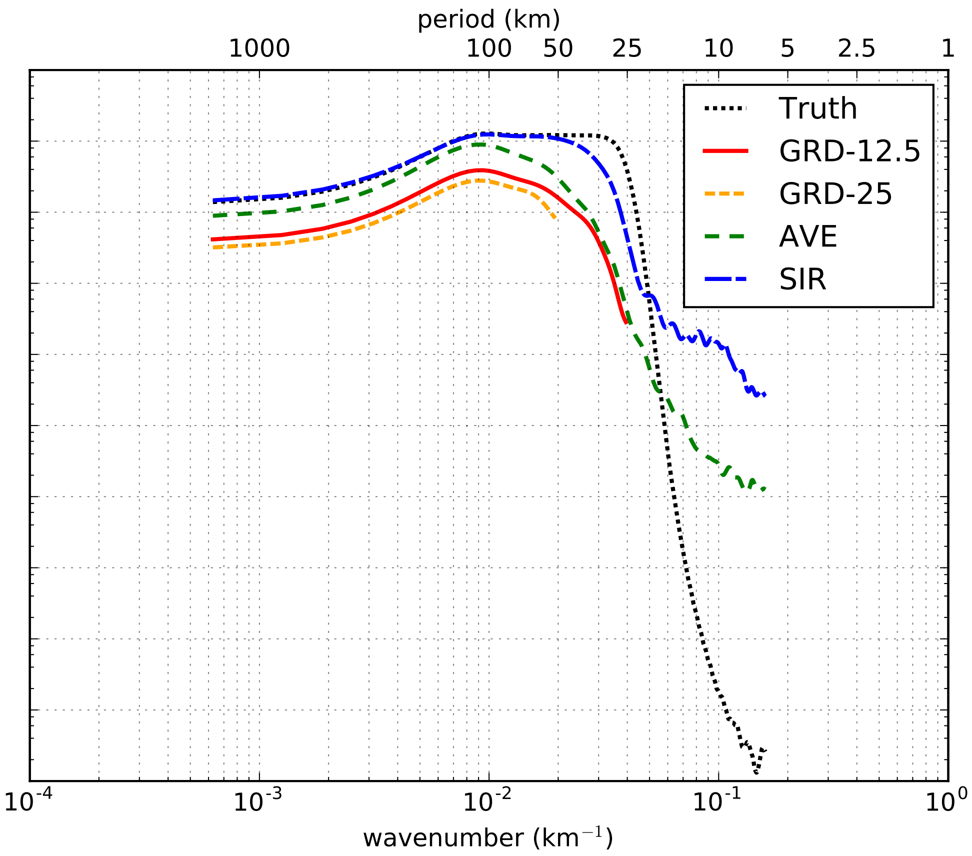

Figure 4.11: Spectra for GRD, AVE, and SIR. The spectrum of the truth chirp image is shown for comparison. For clarity, the GRD spectra are plotted shifted downward slightly but otherwise is very similar to the AVE spectrum. GRD is computed on grid spacings of 12.5 and 25 km and AVE and SIR are on a grid spacing of 3.125 km.

agreement with the spectra results in Fig. 4.11. GRD cannot recover the highest frequencies due to aliasing. AVE and SIR recover all the frequencies for this particular chirp, but with diminished amplitudes. SIR, however, is able to recover the amplitudes better than AVE, especially the troughs of each wave. The improved amplitude recovery of SIR versus GRD and AVE matches the higher energy in mid-range frequencies in Fig. 4.11.

The spectra are also computed using ASCAT measurement geometry from a polar region. Due to the near-polar orbit of ASCAT, a high-latitude region is more densely sampled than at lower latitudes—i.e., the δ-density value is smaller. With 5 days of data, the spectra (not shown) indicate an effective resolution of 12.5 km. However, in order to improve the temporal resolution of polar regions (e.g., to detect and track fast-moving icebergs), 2 days

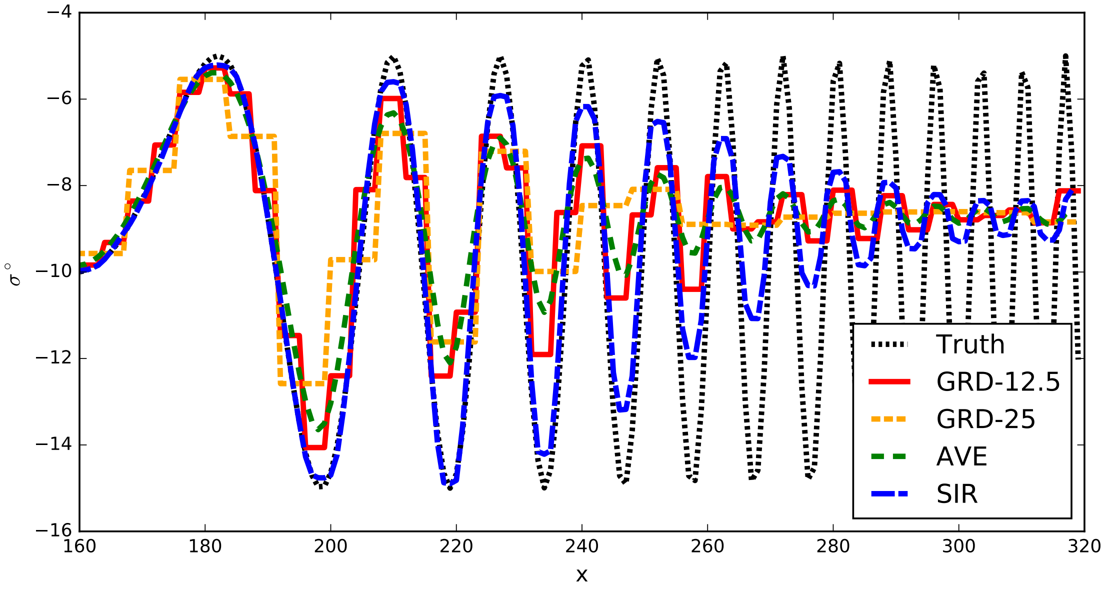

Figure 4.12: The averaged row values for the truth input and the GRD, AVE, and SIR outputs. Due to symmetry, only half of the row is shown.

of ASCAT data is used. The spectra for 2-day polar regions indicate a spatial resolution of about 15 km.

Including data from both ASCAT instruments on MetOp-A and MetOp-B in tandem processing further increases the number of measurements. The spectra results (not shown) however do not support an improved spatial resolution—this is likely due to the two MetOp satellites operating in a co-planar orbit. However, tandem processing enables improved temporal resolution since combining data from both instruments improves the coverage over that using only a single ASCAT instrument.

Although the spectra results vary as a function of parameters including the truth image and measurement geometry, the general trends observed are similar. The coarse grid spacing of GRD precludes recovery of high spatial frequencies. The results in both spatial and frequency domains show that AVE and SIR both contain spatial content down to about 15 km, but as evidenced by the attenuation they cannot recover *all* data to 15 km; however, SIR has less attenuation and is better able than AVE to recover the high-frequency content. Both AVE and SIR provide improved spatial resolution over GRD.

4.6 Conclusion

Image reconstruction algorithms, in conjunction with the measurement SRF, enable enhanced-resolution estimates of the sampled Earth surface σ°. The effective spatial resolution of the reconstructed AVE and SIR products is difficult to precisely quantify for ASCAT but is on the order of 15 km to 20 km compared to at least 25 km for GRD-12.5 and 50 km for GRD-25. Increasing the number of ASCAT passes used increases the sample density, which also improves the resolution (to a point) and reduces noise.

The parameters of reconstruction discussed include the choice of pixel size, quantizing the measurement SRF, and the number of SIR iterations. A pixel size of 4.45 km/pixel is chosen for compatibility with other products in the SCP dataset. This is selected to balance the requirements of using a pixel resolution finer than the effective resolution but not so fine as to provide no additional benefit for the larger storage requirement. Based on simulated truth images and actual observation geometry, I select 30 iterations of SIR and do not use a quantized SRF. The choice of SIR iterations is a reasonable tradeoff to reduce signal error without needlessly amplifying reconstruction noise.

I also evaluate the pixel statistics of the GRD, AVE, and SIR methods, noting that the statistics are dependent on the SRF, sample geometry, and synthetic truth pixel statistics. Here, the results for ASCAT are examined, but the values may readily be determined for any arbitrary SRF and sample geometry, e.g., for another scatterometer. I find that SIR introduces a small bias of about 0.02 dB but has a smaller pixel variance than does AVE. The pixel variance of GRD is directly proportional to the number of measurements used per pixel; thus, the choice of grid spacing is an important consideration for GRD. However, the number of measurements per pixel for AVE and SIR is affected by the sampling geometry and measurement SRF, not the grid spacing; thus, the grid spacing size is not significant for AVE and SIR pixel variance.

The correlation coefficient between reconstructed pixel pairs is also evaluated. GRD pixels are only weakly correlated with adjacent pixels, but the correlation extends further for AVE and for SIR. Because of the measurement geometry and SRF shape, the correlation coefficient may be directionally dependent for AVE. SIR, however, tends to circularize the correlation coefficient contours at the tradeoff of an increased correlation area.

A basic spectral analysis indicates that AVE and SIR perform a limited recovery of high-resolution information. The resolution recovery for GRD is constrained by the coarse grid spacing. SIR improves upon AVE and amplifies high-frequency content that is otherwise attenuated. Since the number of SIR iterations is truncated, it is only a partial reconstruction. Increasing the number of SIR iterations may continue to recover high-frequency content, but high-frequency noise is amplified as well.

The processed ASCAT σ° products at conventional resolution using GRD and at enhanced resolution using AVE and SIR are publicly available in the SCP archives (`http://scp.byu.edu`) and may be used in a variety of geoscience applications.

Chapter 5

Near-Coastal Enhanced-Resolution Wind Retrieval

An application of enhanced-resolution backscatter is the production of enhanced-resolution wind estimates, referred to as ultra-high resolution (UHR) winds. While UHR winds are useful, their utility is limited by the land contamination present in near-coastal regions. This chapter addresses this drawback by identifying and removing σ° measurements sufficiently contaminated by land. In order to validate the accuracy of the near-coastal ASCAT winds and to confirm the absence of land contamination, the ASCAT winds are compared against buoy-measured winds.

The production of UHR ASCAT winds is outlined in Section 5.1. The land contamination ratio (LCR), or land fraction, which was discussed in Section 2.5.1, is applied to ASCAT σ° measurements in Section 5.2. The LCR is used in order to reduce land contamination to acceptable levels and enable (unbiased) wind retrieval much closer to land than otherwise. This is detailed in Section 5.3 for ASCAT UHR winds. Finally, the near-coastal ASCAT wind, both at conventional and enhanced resolution, is validated in Section 5.4 using buoy measurements.

5.1 Ultra-High Resolution Winds

KNMI[1] generates the ASCAT Level 2 wind product, referred to in this chapter using the initialism L2W. The L2W winds are produced on a swath-oriented grid at a grid spacing of 12.5 km. Each grid location is termed a wind vector cell (WVC). Of the L2W varieties available, this chapter uses the "coastal" L2W product, which contains wind estimates closer to land than the original L2W dataset but with a different approach than the LCR method

---

[1] `http://knmi.nl`

in this chapter [65]. The target wind retrieval error in the L2W dataset is 2 m/s RMS error for wind speeds below 25 m/s [2].

In contrast to the conventional resolution L2W winds, the ultra-high resolution (UHR) winds are produced from reconstructed σ° values. UHR is processed on a high-resolution grid aligned with the swath-oriented 12.5 km L2W grid, but it is subdivided into a grid with 1.25 km spacing. Similar to the L2W grid, each UHR grid point is referred to as a UHR WVC. The AVE algorithm is used to generate UHR σ° values at each UHR WVC from the original σ° measurements and their associated SRFs. The AVE image reconstruction method includes a limited form of resolution enhancement by which the value reported at each grid point is the average of all nearby σ° measurements, weighted by each measurement's associated SRF value at that point, as demonstrated in Chapter 4. AVE reconstruction is performed separately for each of the three ASCAT beams within each swath. Further information on ASCAT UHR, including validation through comparison with SAR-derived wind, is found in [66]. The ASCAT UHR winds are produced by the BYU MERS Lab.

Figure 5.1 highlights the difference in spatial resolution between retrieved UHR and L2W winds for a high wind event: Hurricane Katia of 2011. Storms tend to have more high-resolution wind features than many other weather patterns due to their high wind speeds and cyclonic nature and therefore provide excellent case studies for comparing the two wind products [66–68]. In Fig. 5.1, the UHR wind speed contours are more detailed with higher frequency variations than L2W. Additionally, the eye of the storm is more clearly defined in the UHR image, and the pattern of decrease in wind speed away from the center is more detailed.

While the UHR winds are useful in estimating higher resolution features than L2W, the wind estimates near land are biased too high (examples are shown below in Section 5.3). To mitigate these near-coastal errors, I require the land fraction of each ASCAT measurement. It is anticipated that a future update to the ASCAT L1B data will include this quantity, but until then, the land fraction must be computed during UHR processing.

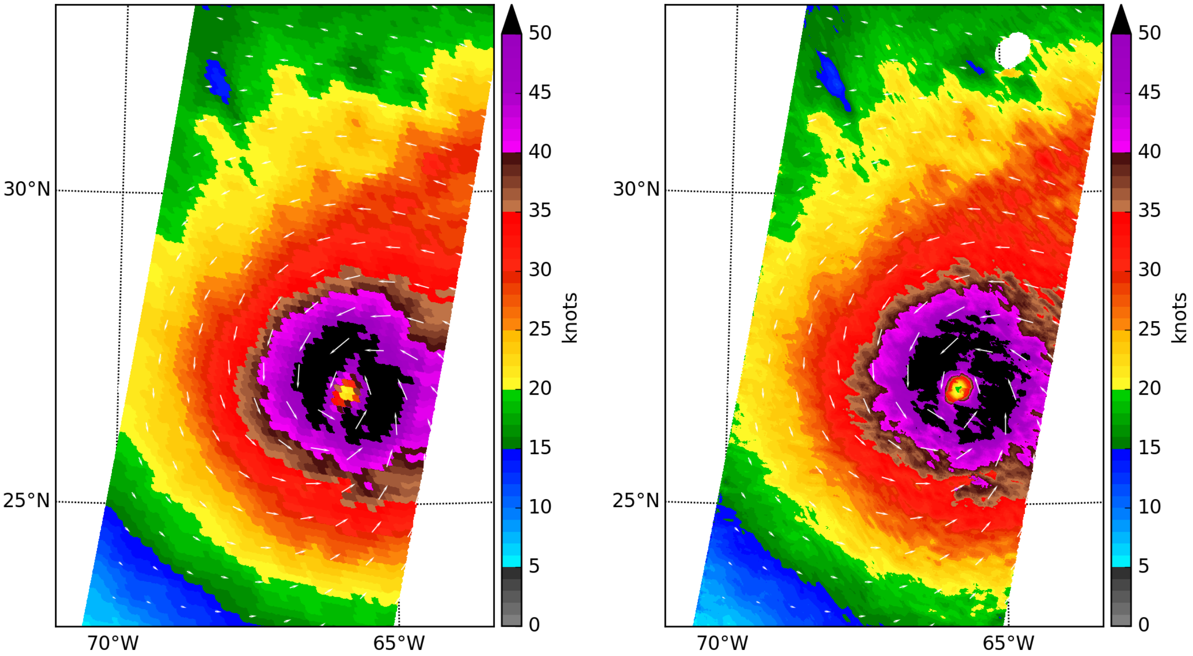

Figure 5.1: L2W winds (left) and UHR winds (right) retrieved from ASCAT on 2011-09-06 in the North Atlantic. The storm shown is Hurricane Katia. Direction arrows are downsampled to increase visibility.

5.2 ASCAT Land Fraction

The land contribution ratio (LCR), or land fraction, is an application of the SRF to ASCAT σ° data. As described in Section 2.5.1, it characterizes the degree each measurement of σ° over the ocean is (possibly) contaminated by nearby land by incorporating information about the size, shape, and orientation of the measurement SRF [46].

The LCR is defined in Eq. (2.32) and repeated here for convenience:

$$\mathrm{LCR}_i = \frac{\sum_{x,y} L[x,y]\, h_i[x,y]}{\sum_{x,y} h_i[x,y]}, \tag{5.1}$$

where $L[x,y]$ is a rasterized binary-valued land map and $h_i[x,y]$ is the SRF value of measurement i at pixel $[x,y]$. The rasterized land map used is based on the GSHHG dataset[2]. The map is on a equirectangular projection with a grid spacing of $\frac{1}{100}^\circ$ (approximately 1 km, varying as a function of latitude).

---

[2] `http://www.soest.hawaii.edu/pwessel/gshhg/`

However, the LCR as defined by Eq. (5.1) may not be exact since the land map may not perfectly characterize coastal regions. The land map is a binary indicator of land or ocean, but for some coastal regions (e.g., marshes) the true σ° is not spatially homogeneous over the "land" portion of the SRF and the full integral formulation of the LCR from Eq. (2.31) is required. Notwithstanding this weakness, in practice the LCR model is valid for most coastal regions.

To compute the LCR for each ASCAT measurement, a grid tangent to the Earth surface at the reported measurement location is defined [59]. This grid has a spacing of 1 km and extends over a 60 km by 60 km area. For each point on the grid, the SRF value and land value ($h_i[x, y]$ and $L[x, y]$) are evaluated. The terms for all grid points are combined as in Eq. (5.1) to compute the final LCR estimate for the measurement.

To illustrate, the LCR is evaluated with σ° data for a region containing the island Niue in Fig. 5.2. The computed LCR compares well against the larger σ° values observed over Niue. As expected, the LCR shape and extent correspond to the "blurring" of σ° measurements around the island coast. Due to the SRF orientation and shape, the blur is not rotationally symmetric, but spreads further along one direction than the other.

The interpolated LCR and σ° values along the transects labeled in Fig. 5.2 are shown in Fig. 5.3, labeled A and B. The portions of the transects over land are also indicated in the figure. The number of LCR values above a threshold (e.g., -20 dB) differs for the two transects, indicating that the minimum land distance of uncontaminated measurements varies. Along transect A, the σ° measurements are only biased by land within about 5 km of land, representing a favorable SRF orientation. Transect B represents a worst-case SRF orientation, where the σ° measurements are land contaminated within about 25 km of land.

5.3 Land Contamination Removal

As discussion in Section 2.5.1, land contamination in σ° measurements affects the retrieved winds. A traditional approach to removing land contamination is to use a distance threshold such that all σ° measurements within the threshold are discarded. However, since the ASCAT measurement SRF is non-circular, a strict distance threshold is sub-optimal. A measurement may lie "parallel" to land so it falls within the distance threshold yet

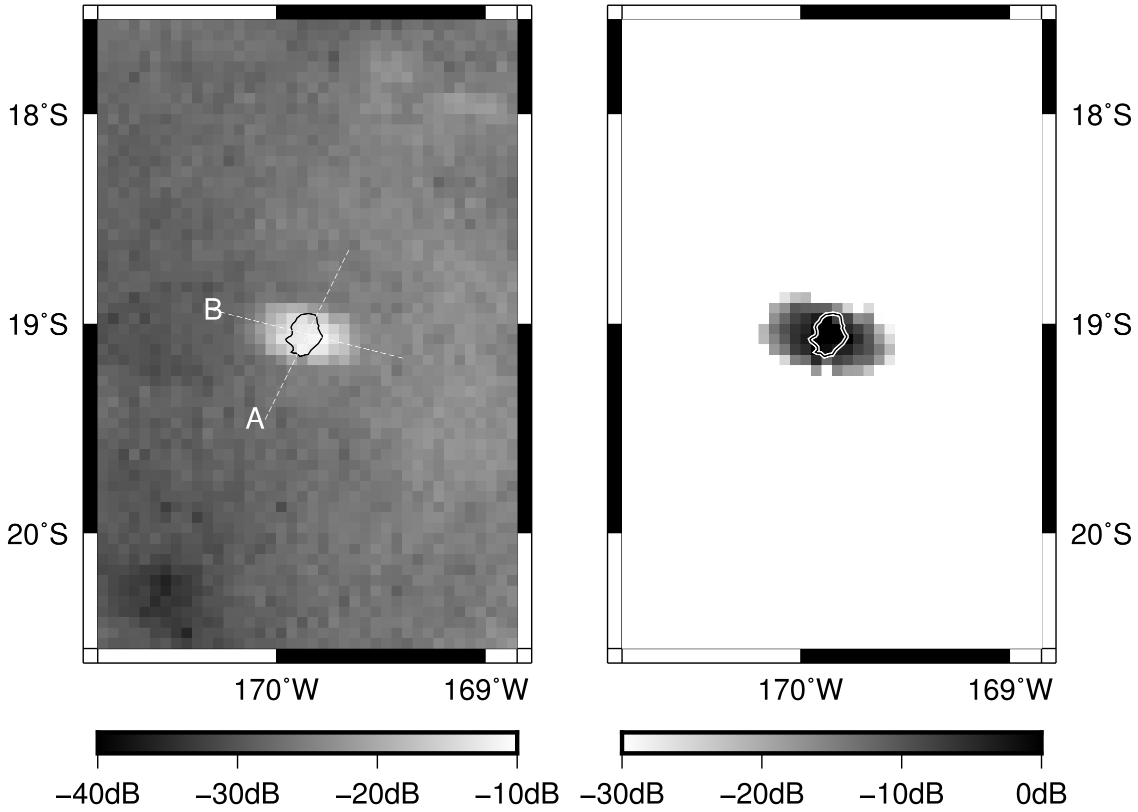

Figure 5.2: The observed σ° (left) and computed LCR (right) near Niue on a grid spacing of 0.05° ($\approx 6\,$km). The coastline is indicated with the solid line. The dashed lines are transects A and B for Fig. 5.3.

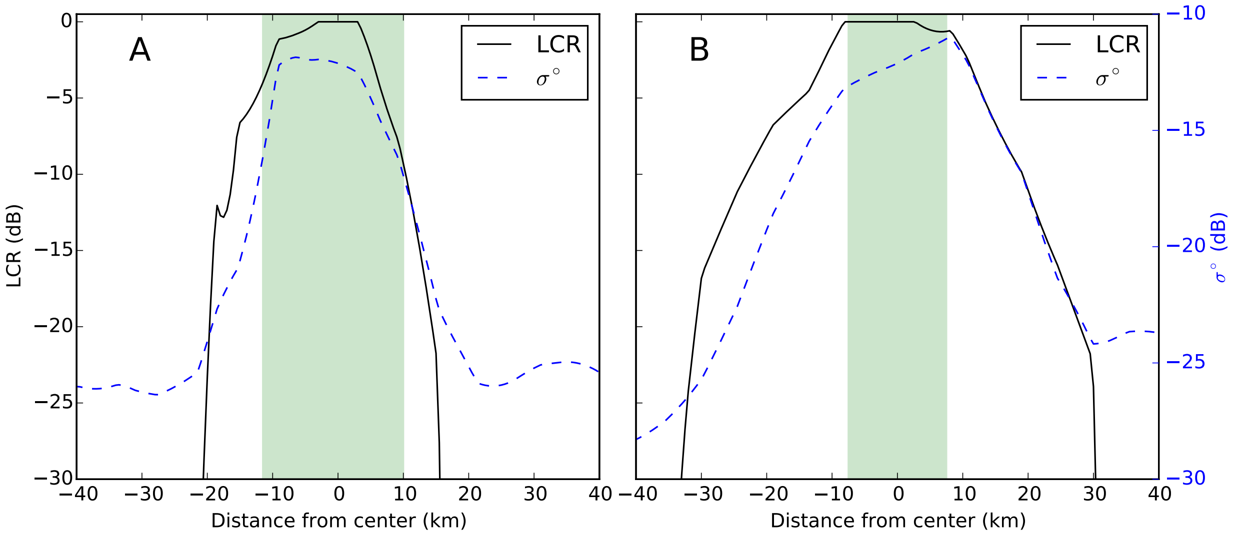

Figure 5.3: The observed σ° and computed LCR values along the two transects of Fig. 5.2. The portion of the transects over land are indicated with shading. The values between measurements are linearly interpolated.

be uncontaminated by land. Or, if a measurement is "perpendicular" to land, then even measurements far away (up to half the "length" of a measurement footprint) are affected by land. This is illustrated in Figs. 5.2 and 5.3, in which the land contamination (as manifest by larger σ° and LCR values) is shown to extend further from the coastline for transect B than for transect A. For this reason, I examine the removal of land contamination in UHR winds using the LCR.

The LCR for each measurement is evaluated using the corresponding SRF and a binary land map, as described in Section 5.2. To entirely avoid any land contamination, all measurements with a nonzero LCR would be discarded and not used for wind retrieval. However, in order to increase the quantity of retrievable near-coastal winds, this strict threshold is relaxed. In fact, it is possible to retain measurements for wind retrieval, even if they contain a small amount of land contamination, as long as the impact of the land contamination on the wind is small.

Based on trial-and-error with some case studies, I find that a reasonable LCR threshold is $-20\,\mathrm{dB}$ (or, 0.01): any measurement with an LCR greater than $-20\,\mathrm{dB}$ is not used for wind retrieval. However, this threshold level is entirely a subjective choice. The more objective approach discussed in this section is to choose the threshold level subject to minimizing a suitable error metric. This also allows the LCR threshold to vary across the region as a function of local conditions.

My approach with ASCAT is similar to previous work with QuikSCAT land contamination [46]. The QuikSCAT LCR threshold is evaluated using compass simulations and found to be largely a function of local land σ°, local wind speed, and cross-track position. I find this evaluation holds for ASCAT as well. The local wind direction does not significantly affect the results.

The "compass simulation" procedure [46] is to define a "truth" wind field with spatially constant speed and direction. The scatterometer measurement geometry and GMF are used to sample the truth wind field to create synthetic σ° measurements, along with an appropriate level of measurement noise. The σ° values are then passed through wind retrieval, and the retrieved winds are compared with the input truth wind field. Multiple truth wind fields with different wind speeds and directions are used to evaluate the retrieval performance over

Table 5.1: LCR compass simulation input values, for a total of $10 \times 8 \times 10 \times 7 = 5600$ input combinations.

Parameter	Values
Wind speed (m/s)	$2.5, 5, \ldots, 25$
Wind direction (degree)	$0, 45, \ldots, 315$
LCR value (dB)	$-45, -40, \ldots, 0$
Land σ° (dB)	$-30, -25, \ldots, 0$

a variety of parameters. Land contamination is additionally modeled by including a land σ° value and LCR value in the truth wind field. To give the worst-case error, each simulated LCR value is applied equally in all beams.

The compass simulations are conducted for ASCAT for a range of wind speeds, directions, land σ° values, and LCR values, as listed in Table 5.1. The ocean-only error is determined by computing the RMS wind speed error with no land contamination present. An error threshold is defined where the total RMS wind speed error is set so that the *additional* error due to land contamination is 10 % of the ocean-only error. While another value could be used, I select a 10 % level since the total speed error, even at wind speeds of 25 m/s, is less than 1.0 m/s. This is well below the ASCAT L2W target RMS wind speed error of 2.0 m/s. For an example case, the ocean-only error is shown in Fig. 5.4. The maximum land-only and therefore total error are also indicated.

The LCR threshold selected is the LCR value such that the corresponding RMS speed error meets the error threshold. The threshold level is a function of (1) local wind speed, (2) local land σ°, and (3) cross-track location. The threshold values are stored as a lookup table, in order to determine the maximum LCR threshold such that the additional wind speed RMS error due to land is at most 10 % of the ocean-only error. The local wind speed and land σ° are determined for each measurement by averaging nearby L2W wind speeds and land σ° values for each near-coastal measurement. The cross-track location is given in terms of the nearest L2W WVC.

A selection from the LCR lookup table is shown in Fig. 5.5 for a single cross-track position. Values for other cross-track locations are similar, but they vary somewhat. For low wind speeds and low land σ° values, a modest LCR threshold level may be used (> -20 dB).

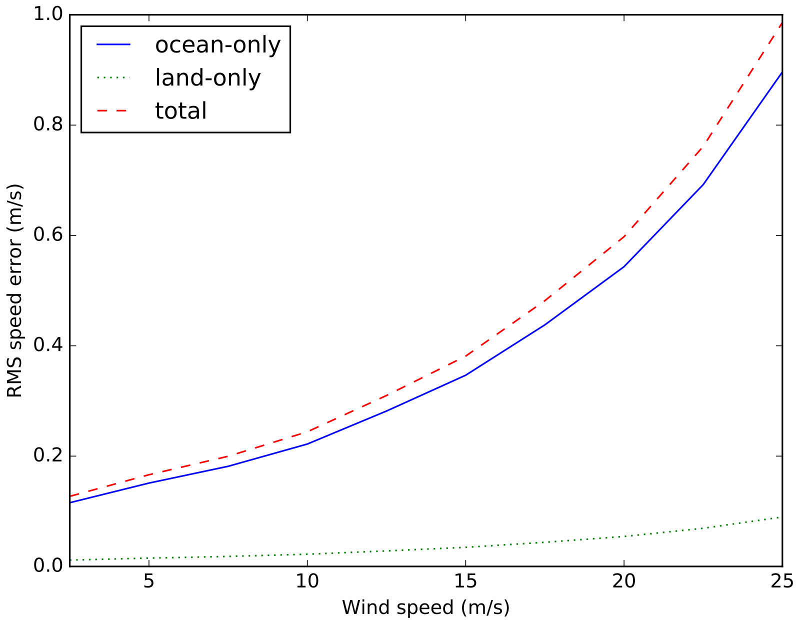

Figure 5.4: The RMS wind speed error as a function of truth wind speed for a particular WVC. The ocean-only error is determined, which error increases as a function of truth wind speed. The land-only error is set to 10 % of the ocean-only error. The total error is also indicated.

As wind speeds decrease or as land σ° increases, the LCR threshold must be decreased to maintain the same maximum RMS error.

The land contamination removal described in this section, including the concept of a dynamic LCR threshold, builds on previous work originally conducted for the QuikSCAT scatterometer by Owen and Long [46]. I find that the basic approach and results for land contamination removal using QuikSCAT are similar with ASCAT, notwithstanding the differences in measurement geometry between the two scatterometer designs. However, my contributions in applying this technique to ASCAT differ in two key respects. First, for QuikSCAT, the compass simulations are used to find, for each WVC, the wind direction that gives the largest RMS wind speed error. For ASCAT, the speed errors are less dependent on wind direction than for QuikSCAT, so instead of using the worst-case truth wind direction, I average the results across all wind directions. This simplifies the computation of the dynamic LCR threshold since the worst wind direction as a function of WVC no longer needs to be retained.

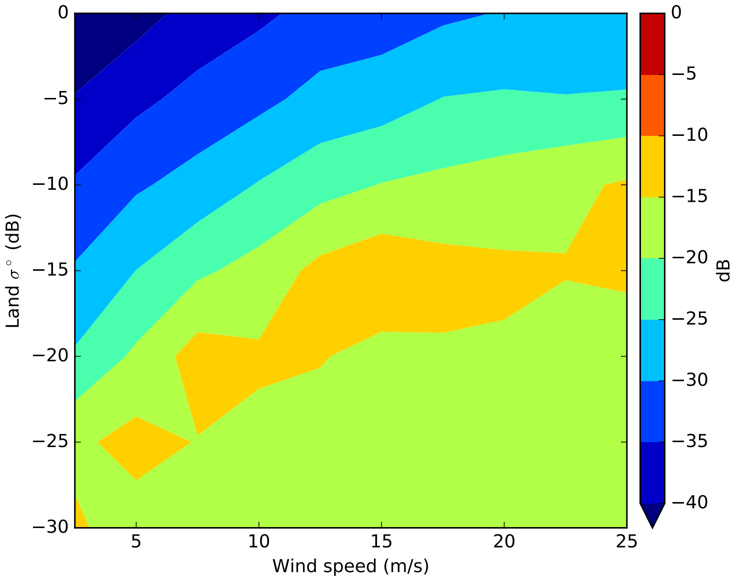

Figure 5.5: For a WVC, the largest LCR value such that the land contamination error is within 10 % of the ocean-only RMS wind speed error. The LCR value is a function of wind speed, land σ° value, and WVC.

Second, the Owen and Long approach [46] sets the maximum RMS wind speed error to be a percentage of the truth wind speed. The exact percentage appears to vary as a function of WVC but ranges between 15 % and 20 %, with a mean value of 18 % across the entire swath. Instead, for ASCAT, I set the maximum RMS wind speed error relative to the ocean-only RMS speed error. This is a more direct method of precisely controlling the amount of error due to land contamination versus the typical retrieval error encountered over open ocean.

To illustrate land contamination mitigation using a dynamic LCR threshold, UHR wind speeds are shown in Fig. 5.6 for a Caribbean region containing many islands and coastlines. Four cases of UHR are produced: with no land contamination mitigation, with a conventional distance threshold of 30 km, with a constant LCR threshold of −20 dB, and with a dynamic LCR threshold. The mean dynamic LCR threshold level for this region is −25.2 dB, but due to differing nearby land σ° levels and wind speeds, it varies from −38.1 dB to −6.2 dB, with a standard deviation of 4.9 dB.

As expected, with no attempt at avoiding land contamination, the wind speeds near land in Fig. 5.6 are biased high. This is visible around the many islands and coasts in the region. A distance threshold of 30 km is effective at removing land contamination, but removes all near-coastal measurements, contaminated or not. The LCR approach permits retrieval much closer to land, with no visible wind speed biases. For this region, using the constant LCR threshold permits the estimation of winds slightly closer to the coasts than with the dynamic LCR threshold. However, the dynamic threshold ensures a maximum error level in a more controlled manner. For this region, of all valid WVCs within 30 km of land, 50 % are within 18 km, and 10 % are 8 km or closer.

Another example of ASCAT winds is shown in Fig. 5.7. The storm is Hurricane Rina (2011) in the Gulf of Honduras. This region contains both a high wind event as well as islands and coastlines. As with Fig. 5.6, processing with LCR removes land contamination while retaining wind estimates close to land, so long as the land contamination error is small.

It may be possible that the distribution of retrieved winds near land may differ from those over open ocean due to residual, undetected land contamination or to geophysical effects, since the actual near-coastal wind may not be neutrally stable or otherwise affected by land. For these reasons, although UHR processing with LCR enables near-coastal wind retrieval, I next examine these wind estimates through comparison with near-coastal buoy data.

5.4 Near-Coastal UHR Validation

In order to validate the near-coastal UHR wind data, ASCAT winds are compared with buoy-measured winds. I use buoy data distributed by the NOAA Marine Environmental Buoy Database.[3] I select buoys in a region along the North American coastline of the Atlantic Ocean where buoys are present at a variety of distances from land. The buoy locations and identification numbers are shown in Fig. 5.8.

In order to compare the buoy-measured winds with ASCAT wind estimates, the buoy-measured winds are converted to neutrally stable wind speeds at a standard height of 10 m above sea level to match the ASCAT winds. I use the LKB model [69, 70], which additionally requires other buoy-measured quantities including air and sea temperatures and

---

[3] `https://www.nodc.noaa.gov/BUOY/`

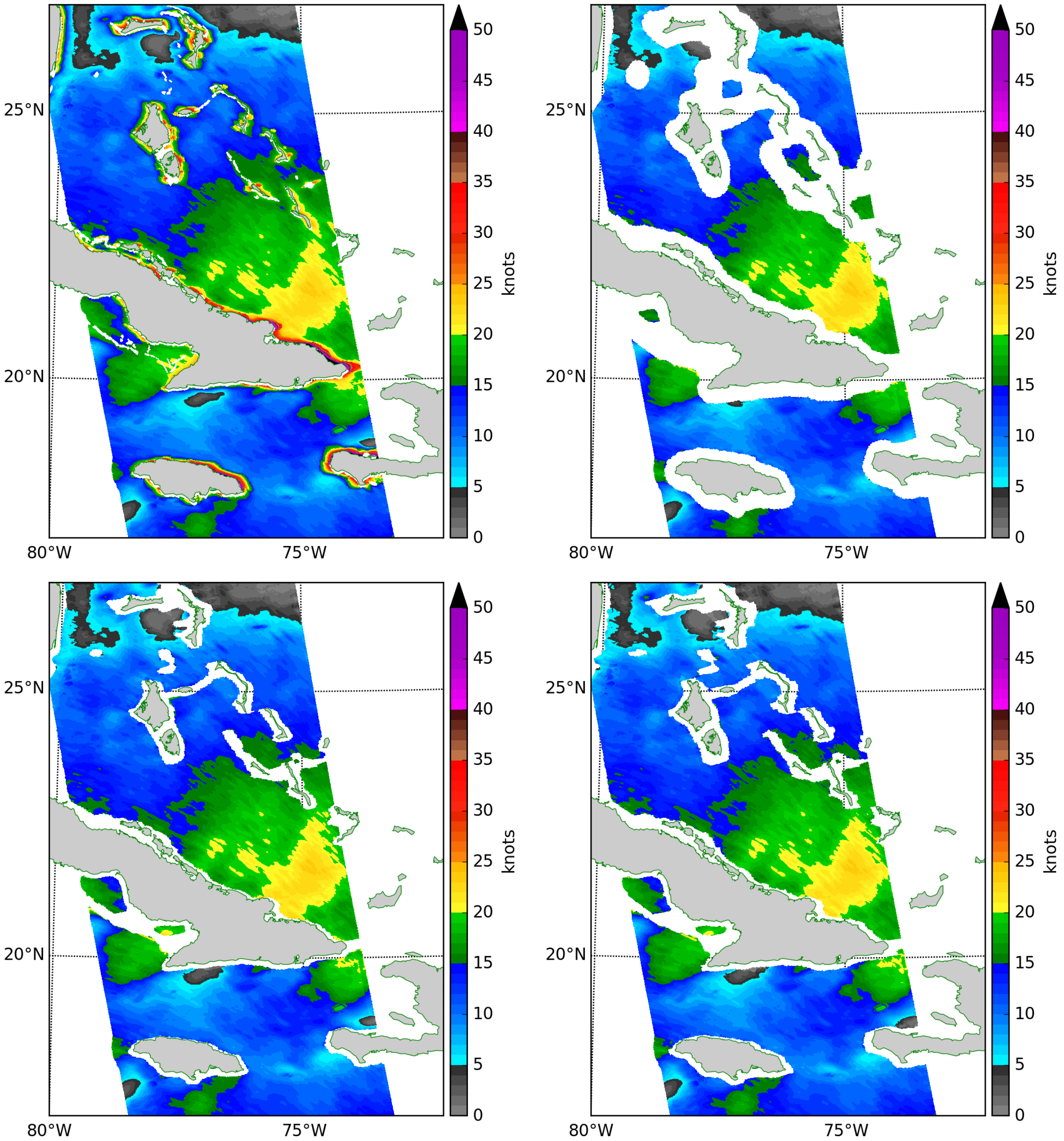

Figure 5.6: UHR winds with no land contamination mitigation (top left), with a distance threshold of 30 km (top right), with a constant LCR threshold of −20 dB (bottom left) and with a dynamic LCR threshold (bottom right). ASCAT-A data are from an ascending pass on 2013-02-05, orbit 32682, right swath.

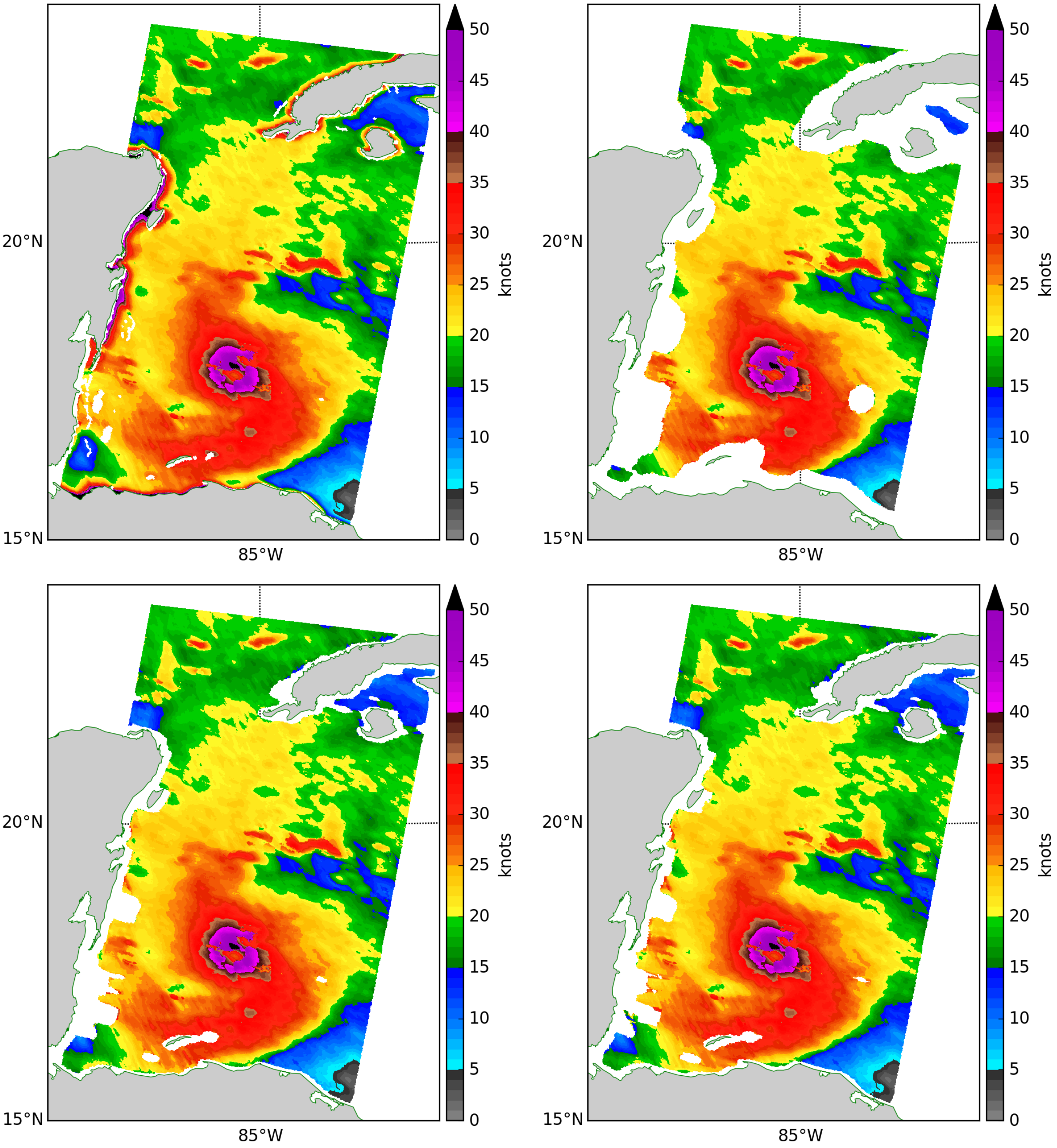

Figure 5.7: UHR winds with no land contamination mitigation (top left), with a distance threshold of 30 km (top right), with a constant LCR threshold of −20 dB (bottom left) and with a dynamic LCR threshold (bottom right). ASCAT-A data are from a descending pass on 2011-10-26, orbit 26040, right swath.

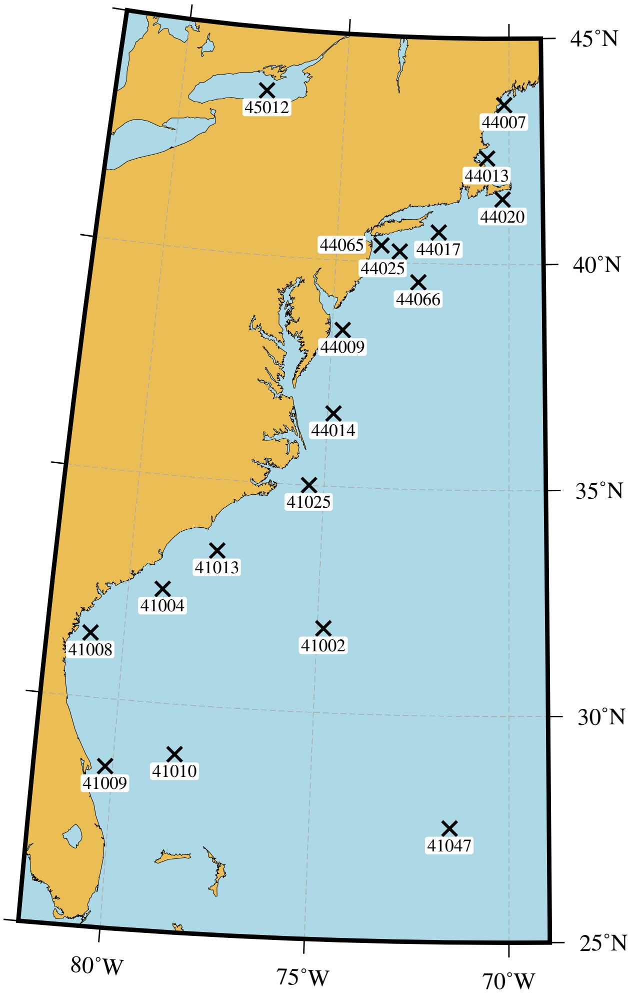

Figure 5.8: The buoy locations and ID numbers used for near-coastal validation.

relative humidity. Only buoy measurements with sufficient quality-controlled information are used, and only buoy wind speeds above 5 m/s are considered.

Passes from both ASCAT-A and ASCAT-B are used to increase the number of collocations between the buoys and the ASCAT instruments. Where a collocation is found, all ASCAT UHR WVCs within 10 km of the reported buoy location are averaged together. Because the buoy winds are reported every 10 min, the largest temporal difference between a collocation is 5 min.

The buoy and ASCAT collocations are collected for the date range of 2014-07-01 to 2015-06-30. In addition to collecting the L2W winds, three variations of UHR processing are included: `UHR-none`, which does not perform any land contamination mitigation; `UHR-mdl`, which discards all σ° measurements within 30 km of land from UHR processing; and `UHR-lcr`, which uses LCR processing with a dynamic LCR threshold.

The L2W product has previously been validated using buoy measurements [71], so this comparison is expected to yield similar results. The `UHR-none` product is anticipated to perform poorly near land due to land contamination but have the greatest number of collocations. The `UHR-mdl` represents a best-case situation where no land contamination is present, but it has a reduced number of collocations. In order to validate the removal of land contamination, the `UHR-lcr` product is predicted to have similar statistics as the L2W and `UHR-mdl` cases, but with more collocations than `UHR-mdl`.

A comparison of the ASCAT and buoy wind speeds is shown in Fig. 5.9 for all four cases. The tendency of ASCAT winds to slightly underestimate high wind speeds has been noted previously [71]. Land contamination is readily visible in the `UHR-none` case, where many ASCAT wind speeds that are larger than the buoy wind speeds are present. However, no evidence of land contamination is present in any of the other three cases. These three cases are very similar to each other, although the `UHR-mdl` and `UHR-lcr` correlation coefficient and slope fit the buoy data slightly better than the L2W data does. The ASCAT and buoy wind directions are likewise compared in Fig. 5.10. All four subplots are very similar, indicating that land contamination does not affect wind direction as strongly as it does wind speed. Further, the comparison of UHR and buoy wind directions is very similar to the L2W comparison.

The wind speed residual, or difference between ASCAT and buoy wind speed, is also computed. For bins of buoy wind speeds, the mean and standard deviation of the residuals are shown in Fig. 5.11. As expected, the large bias and standard deviation for the `UHR-none` case, especially at low wind speeds, are evidence of land contamination. The means and standard deviations for the other three cases are very similar to each other, although the UHR results have a lower standard deviation than the L2W results. Additionally, the L2W product has a larger bias at buoy wind speeds of about 5 m/s, which is also present—and larger—for `UHR-none`. However, this bias is not present for `UHR-mdl` nor `UHR-lcr`. For brevity, the wind direction residuals are not shown but are similar for all four cases.

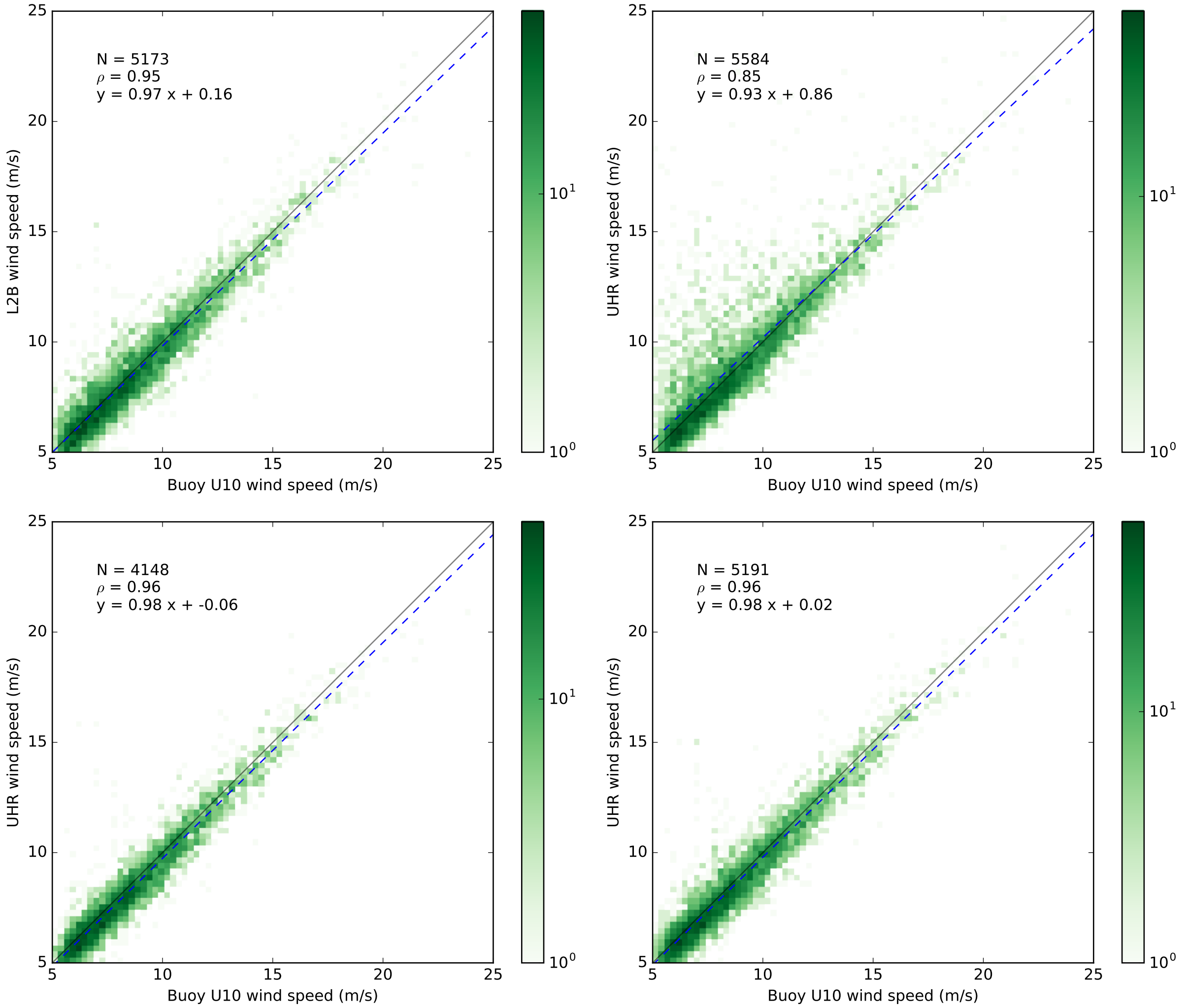

Figure 5.9: ASCAT wind speeds compared to buoy wind speeds. The number of collocations (N), correlation coefficient (ρ), and linear fit ($y = mx + b$) are shown for each case. Top left: `L2W`; top right: `UHR-none`; bottom left: `UHR-MDL`; bottom right: `UHR-LCR`.

Finally, the wind speed residuals are shown in Fig. 5.12 as a function of distance to land. The results at distances greater than about 20 km are identical, indicating that land contamination is not a factor at these distances. Within 20 km of land, the `UHR-none` product has a large bias and standard deviation error that each increase as the distance to land decreases. This is expected since the land contamination increases when closer to land. The L2W case, on the other hand, has a bias within 1 m/s consistently for all coastal distances. As expected, no collocations near land exist for `UHR-mdl`. The `UHR-lcr` product

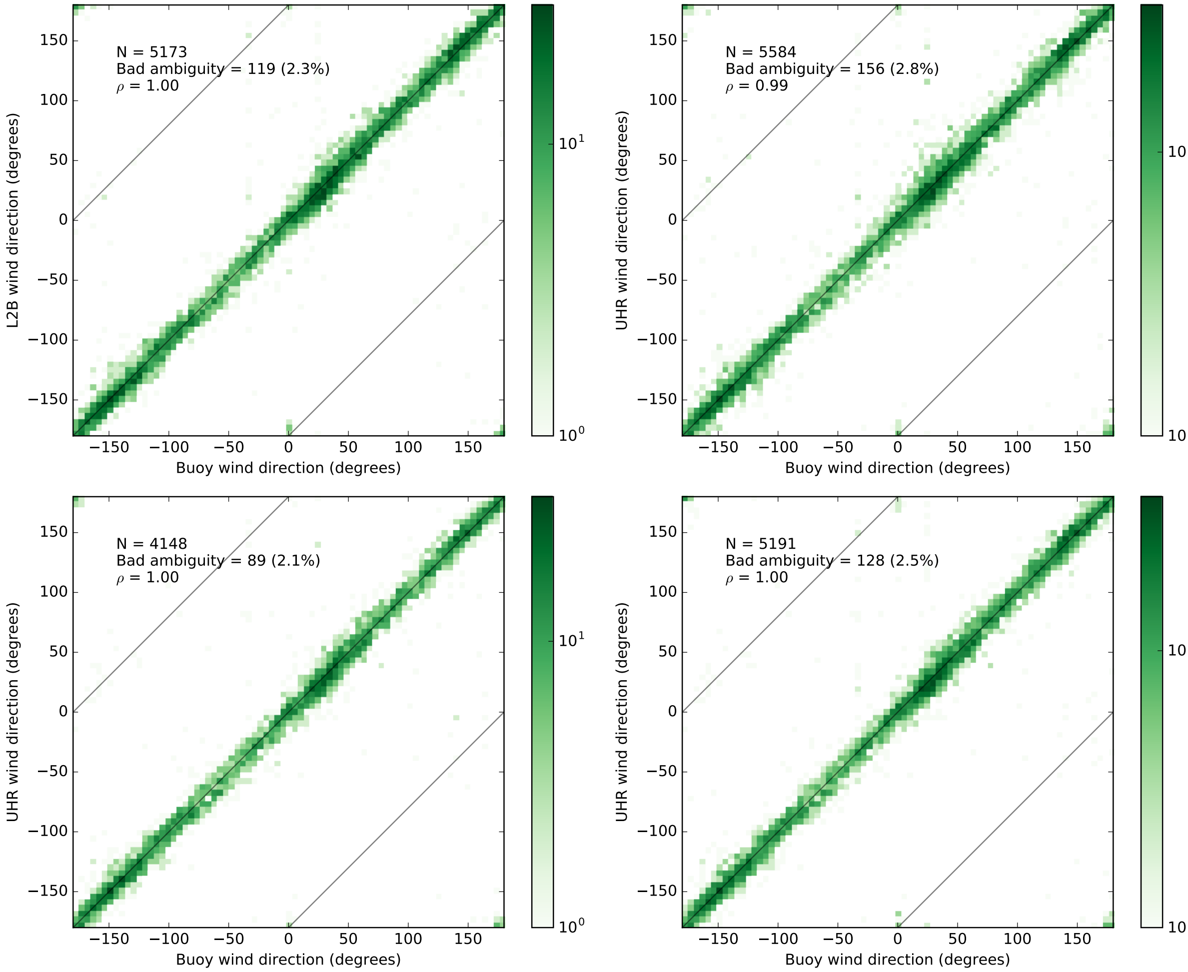

Figure 5.10: ASCAT wind directions compared to buoy wind directions. The number of collocations (N), correlation coefficient (ρ), and number of $\approx 180°$ differences are shown for each case. Top left: `L2W`; top right: `UHR-none`; bottom left: `UHR-MDL`; bottom right: `UHR-LCR`.

has collocations within 20 km, and the bias and standard deviations are similar to the L2W results. This is the desired result.

I conclude based on these collocations with near-coastal buoy measurements, that the LCR method is effective at removing land contamination while retaining a large number of uncontaminated near-coastal wind estimates. With no land contamination mitigation, the UHR product overestimates the wind speeds and increases the retrieval error. In both the `UHR-mdl` and `UHR-lcr` cases, the statistics of the comparisons with buoy winds are very similar to the conventional resolution L2W winds. That is, no evidence suggests the UHR winds to be noisier or to contain more error with respect to the buoys. In fact, the residual

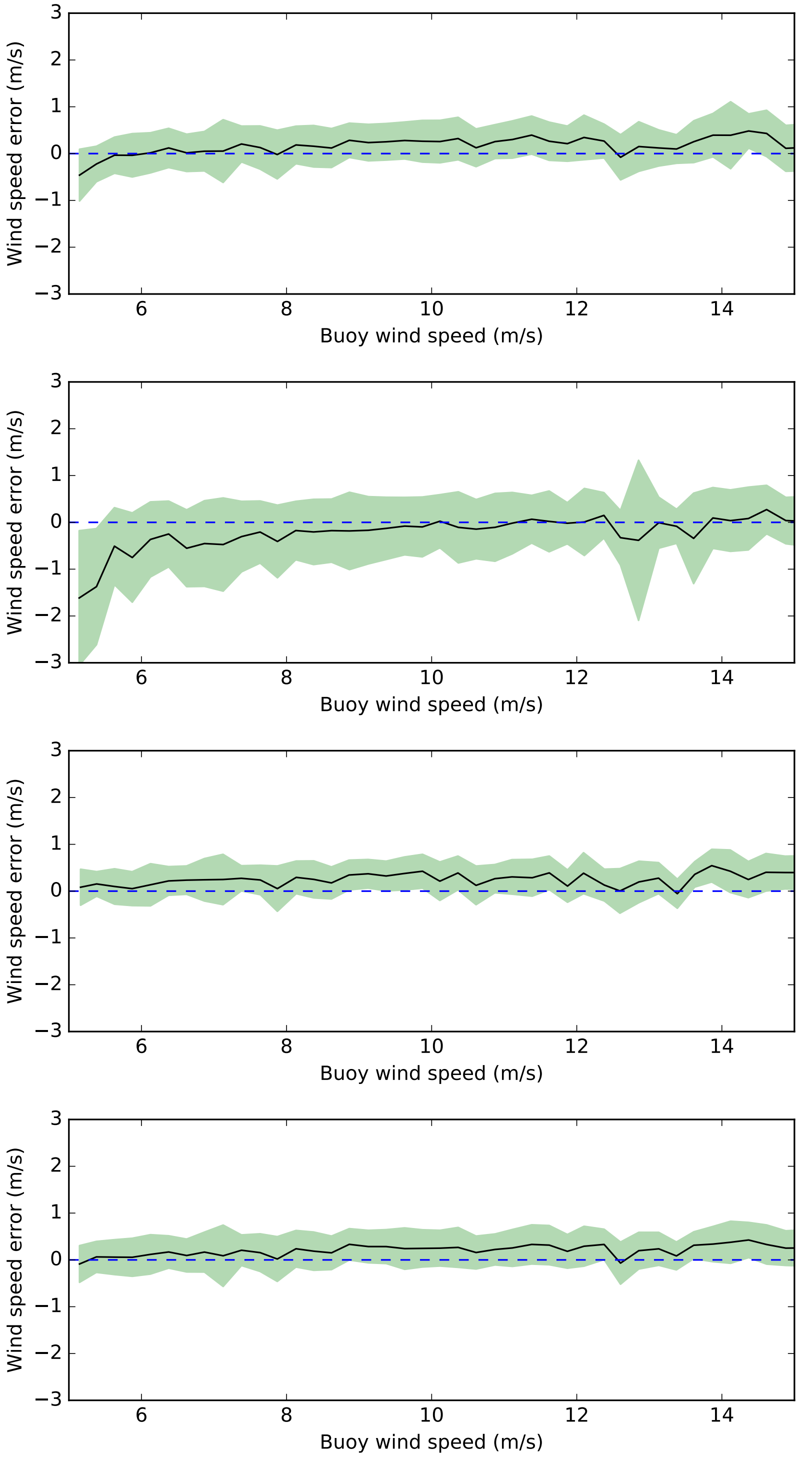

Figure 5.11: The mean and standard deviation of the difference between ASCAT wind speeds and buoy wind speeds. Top to bottom: `L2W`, `UHR-none`, `UHR-MDL`, and `UHR-LCR`.

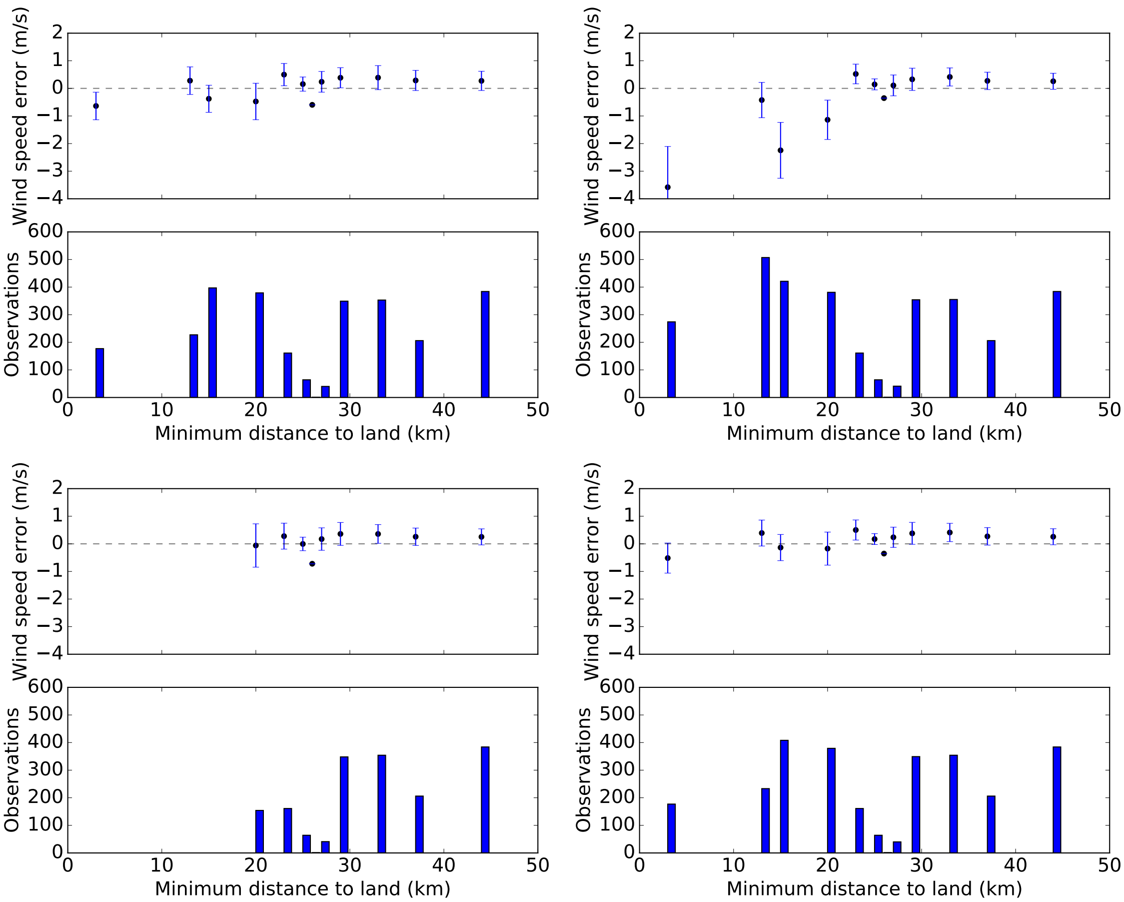

Figure 5.12: As a function of distance to land, the mean and standard deviation of the difference between ASCAT wind speeds and buoy wind speeds. The number of collocations at each distance is also shown. Top left: `L2W`; top right: `UHR-none`; bottom left: `UHR-MDL`; and bottom right: `UHR-LCR`.

speed error statistics are somewhat lower for UHR than for L2W. This may be due to some uncorrected land contamination present in the L2W product.

5.5 Summary

This chapter has demonstrated an additional application of the SRF: the computation of the LCR for each ASCAT measurement in conjunction with a high-resolution land map. The LCR is a useful approach to withhold land-contaminated σ° measurements from wind retrieval since it relies on the actual measurement footprint rather than a worst-case distance threshold. This enables wind retrieval much closer to land.

The near-coastal ASCAT wind estimates are validated through comparison against buoy-measured winds. Land contamination strongly impacts the retrieved wind speed, but wind direction appears less affected. The wind distribution, as examined through the mean and standard deviation of the ASCAT-buoy wind residuals, is shown to have large errors when land contamination is not avoided. With a traditional distance threshold to address land contamination, the UHR wind residuals are similar to—and somewhat better than—the L2W wind residuals. This effectively represents no land contamination. The wind residuals when using LCR have similar statistics, indicating that land contamination, if present, is negligible. This validates the LCR approach with ASCAT UHR winds.

While this chapter applies the LCR to UHR winds, it may be similarly applied for the conventional resolution L2W wind product. At present, the LCR for each measurement must be computed as part of the UHR processing, but it is anticipated that this computation will be part of the ASCAT ground processing at EUMETSAT and reported in the L1B data.

Chapter 6

Applications of Enhanced Resolution Backscatter Images

In this chapter, two applications that utilize the enhanced-resolution σ° data from Chapter 4 and enhanced-resolution wind (UHR) data from Chapter 5 are demonstrated. The first, in Section 6.1, maps the spatial extent of the 2010 Deepwater Horizon oil spill. The second, in Section 6.2, describes the azimuth modulation of ASCAT and QuikSCAT backscatter over East Antarctica.

6.1 Deepwater Horizon Oil Spill

The oil spill from the *Deepwater Horizon* oil rig in the Gulf of Mexico is one of the largest environmental disasters in recent history. The consequences from the roughly 4.4 million barrels leaked [72] continue long after the 15 July 2010 capping of the well. A time-series estimate of the extent and shape of the oil on the ocean surface is beneficial for estimating the amount of oil as a function of time and its impact on ocean life and human industries.

Active microwave sensors are often used for remote detection of oil spills by virtue of their all-weather performance in both day and night conditions. Historically, Synthetic Aperture Radar (SAR) instruments have been used since the spatial resolution—on the order of a hundred meters or less for a spaceborne SAR—is fine enough to map many oil spills [50–53]. Scatterometers such as ASCAT have a coarser spatial resolution. Nevertheless, the processes that enable oil detection using SAR data are the same for scatterometer data.

The spatial extent of the 2010 Deepwater Horizon oil slick is large enough to be resolvable by the enhanced-resolution reconstructed ASCAT data. By exploiting the effects of surface oil on the radar backscatter from ocean waves, the surface extent may be mapped by examining processed data from ASCAT. This section presents a method for mapping the surface oil extent using ASCAT by determining the difference between predicted and observed quantities. Predicted wind is determined from numerical weather predicted (NWP) winds provided by the European Centre for Medium-Range Weather Forecasting (ECMWF). ASCAT measures backscatter. A suitable threshold is chosen to classify ocean regions as oil-affected or oil-free. The mapped surface oil extent is validated using data from other sensors. Lacking information on oil thickness or volume, no attempt is made to estimate thickness or volume.

The methodology for surface oil extent mapping is described in Section 6.1.1. Results for selected case studies are shown, and the performance of the methods is evaluated in Section 6.1.2. To my knowledge, this is the first application of spaceborne scatterometry to detect oil spills.

6.1.1 Method

Surface oil is detectable given sufficient differences between the observed and predicted wind or backscatter. The difference in wind, or wind error, is found by comparing the ASCAT-retrieved winds with ECMWF winds. Similarly, the difference in backscatter, or backscatter error, is determined by comparing ASCAT σ° measurements with predicted σ° values derived from ECMWF winds. If the error is greater than some threshold, the region is flagged as having surface oil. The threshold is determined through minimization of an objective function.

Wind error

For comparison wind data, ECMWF U_{10} is used. In this subsection, the notation U_{10} refers to ECMWF winds and $\hat{U}_{10}$ represents ultra-high resolution (UHR) winds retrieved from ASCAT σ° (UHR winds were described above in Section 5.1). ECMWF winds have a temporal resolution of six hours and a spatial resolution of 1°x1°. The two ECMWF wind fields nearest in time to an ASCAT pass, or rev, are bilinearly interpolated in space to match the ASCAT wind locations, and then interpolated in time to the ASCAT pass. Thus the U_{10} is trilinearly interpolated to match each corresponding $\hat{U}_{10}$.

Although the interpolated U_{10} has the same grid spacing of $\hat{U}_{10}$, it has limited high-frequency spatial content. Taking the difference between U_{10} and $\hat{U}_{10}$ therefore removes the winds with low spatial frequency but preserves any small-scale structure. The wind speed error $\epsilon_{|U_{10}|}$ is defined as

$$\epsilon_{|U_{10}|} = |U_{10}| - |\hat{U}_{10}|, \tag{6.1}$$

and the wind direction error $\epsilon_{\angle U_{10}}$ is defined as

$$\epsilon_{\angle U_{10}} = \angle U_{10} - \angle \hat{U}_{10}. \tag{6.2}$$

Due to instrument noise and biases in ECMWF winds versus ASCAT winds, $\epsilon_{|U_{10}|}$ and $\epsilon_{\angle U_{10}}$ are rarely zero. However, the wind speed error $\epsilon_{|U_{10}|}$ is anticipated to be positive in regions affected by surface oil since the dampened σ° from the oil is manifested after wind retrieval as lower estimated wind speed. Thus, large positive values of $\epsilon_{|U_{10}|}$ are used as a metric to map the oil surface extent. The effect of oil on wind direction is unclear, but large $\epsilon_{\angle U_{10}}$ could indicate the presence of oil.

Backscatter error

ASCAT σ° is reconstructed on on a grid spacing of 4.45 km using AVE for each look separately (fore, mid, and aft). The predicted backscatter is derived from ECMWF winds, which are trilinearly interpolated to match the ASCAT AVE grid. The interpolated winds are input to the CMOD5.n GMF [7] using the observation geometry to find the predicted backscatter for each of the three looks. The difference between the predicted backscatter, σ°, (from ECMWF winds) and the measured backscatter, $\widehat{\sigma^\circ}$, (from ASCAT) for each look k is

$$\sigma^\circ_k - \widehat{\sigma^\circ}_k = \epsilon_k, \tag{6.3}$$

where ϵ_k is the error for look k. As with wind error, some error is anticipated from noise, although the predicted value of ϵ_k is positive in the presence of oil.

The three error look terms are combined using the ℓ_2 norm of the vector $\vec{\epsilon} = [\epsilon_{\text{fore}}\ \epsilon_{\text{mid}}\ \epsilon_{\text{aft}}]^T$:

$$\| \vec{\epsilon} \|_2 = \sqrt{\epsilon_{\text{fore}}^2 + \epsilon_{\text{mid}}^2 + \epsilon_{\text{aft}}^2}. \tag{6.4}$$

The backscatter error is defined as Eq. (6.4), which is used as a metric to map the extent of the surface oil. While the fore and aft measurements are at similar incidence angles, the mid beam σ° is at a lower incidence angle range and is, therefore, generally brighter. Weighting the squared error contributions separately could be used to account for this difference. However, here, equal weights are used for all three looks.

Oil extent validation

Oil coverage products from the Experimental Marine Pollution Surveillance Report (EMPSR) are used to validate the results. The EMPSR is an experimental product produced by the National Oceanic and Atmospheric Administration (NOAA). Analysts interpret SAR and visible imagery from satellites to estimate the surface oil extent of the spill [73]. EMPSR does not report the oil thickness or volume.

The EMPSR product used is the daily composite shapefile, a vector-based geospatial representation of surface oil extent based on the available satellite imagery for the day. EMPSR products are not available every day, so only ASCAT passes that coincide with EMPSR data are used.

Threshold determination

The backscatter and wind speed errors are thresholded to classify regions as either oil-affected or oil-free. The threshold value for each pass is determined by minimizing a objective function. I choose a simple function to express the relationship between probability of false alarm versus probability of detection. The objective function is defined as the weighted combination of two values: the number of oil-flagged pixels that fall within the EMPSR region limits and the number of oil pixels that are outside the EMPSR region. This is expressed as

$$f(\nu) = 1/g + \alpha b, \tag{6.5}$$

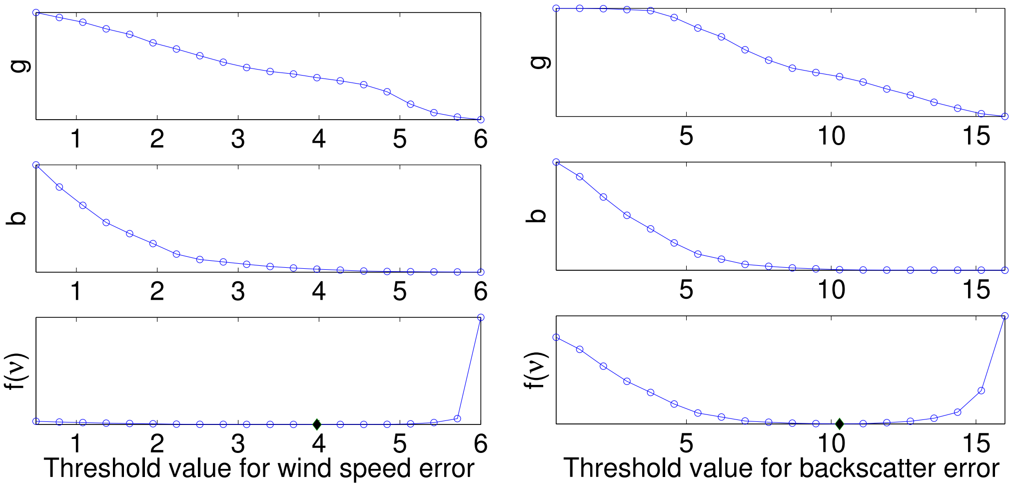

(a) **(b)**

Figure 6.1: The threshold objective function and its components for wind speed error (a) and backscatter error (b) for ASCAT rev 19221 (2010-07-03). The upper and mid subplots show values of g and b, the number of pixels inside and outside the EMPSR region classified as oil. The lower subplots show $f(\nu)$, the objective function value. Vertical axis scaling is arbitrary. The minimum of the function is indicated as a solid diamond.

where ν is the threshold value, $f(\cdot)$ is the objective function, g is the number of correctly classified pixels, b is the number of incorrectly classified pixels, and α is a weighting parameter. The weighting factor α may be set to an appropriate metric weighting, for example to achieve some desired probability of false alarm rate. For this dissertation, I subjectively choose $\alpha = 1 \times 10^{-5}$.

For both backscatter and wind speed errors, the threshold level ν for each pass that minimizes Eq. (6.5), the objective function, is found. Figure 6.1 shows values of g, b, and f for different threshold levels ν for a typical ASCAT pass. The minimum of $f(\nu)$ is indicated on the figure.

6.1.2 Results

The Deepwater Horizon oil spill is located around a latitude of 29 ° N. For ASCAT, a maximum of two passes per day is possible (ascending and descending) at this location, but in practice only about eight passes per 10-day period adequately cover the spill region. For the duration of the oil leak (from 2010-04-21 to 2010-08-25), 204 ASCAT passes over the spill region are available. Of these, 118 have corresponding EMPSR data, and 11 are selected as case studies. For each ASCAT pass over the oil spill region, interpolated ECMWF winds are compared with ASCAT-derived winds to find wind errors $\epsilon_{|U_{10}|}$ and $\epsilon_{\angle U_{10}}$. The measured σ° for each look is compared with the predicted σ° obtained from interpolated ECMWF winds and the CMOD5.n GMF to obtain the backscatter error. Oil extent estimates are found after thresholding the errors, where error greater than the threshold is classified as oil. These are analyzed below. A case study is also presented comparing backscatter error with measured backscatter.[1]

Wind error

As described above, the wind speed error and wind direction error are computed for all available ASCAT passes over the oil spill region. From one of the chosen case studies, the wind errors are shown in Fig. 6.2. Negative wind speed errors are discarded to reflect the expectation of positive error values caused by surface oil. The large values of $\epsilon_{|U_{10}|}$ near the center map the surface oil extent. Unfortunately, no EMPSR data is available on this particular day for validation.

The case studies examined suggest that the wind direction error is not as useful as wind speed error in surface oil mapping. In the best cases, wind direction error varies widely over a small region that is a subset of the oil region mapped by wind speed error. Figure 6.2 is a rare case where the wind direction error is correlated well with the oil spill. Wind direction error may be useful for determining the regions most affected by oil.

For comparison, the wind speed error is shown for two ASCAT passes in Fig. 6.3a and Fig. 6.3c. The wind speed error for both passes strongly correlates with the main body of the oil spill. Smaller-scale oil features are not detectable, however. Some false positives occur south of the mapped oil. These are primarily due to low wind speed oil look-alikes. However, for the main body of surface oil, results from these and other passes show wind speed error is a good match with the EMPSR data.

---

[1] Although the methodology is still applicable, the oil spill results shown below utilize a historical SRF estimate [24] and predate revised work on the SRF presented in Chapter 3.

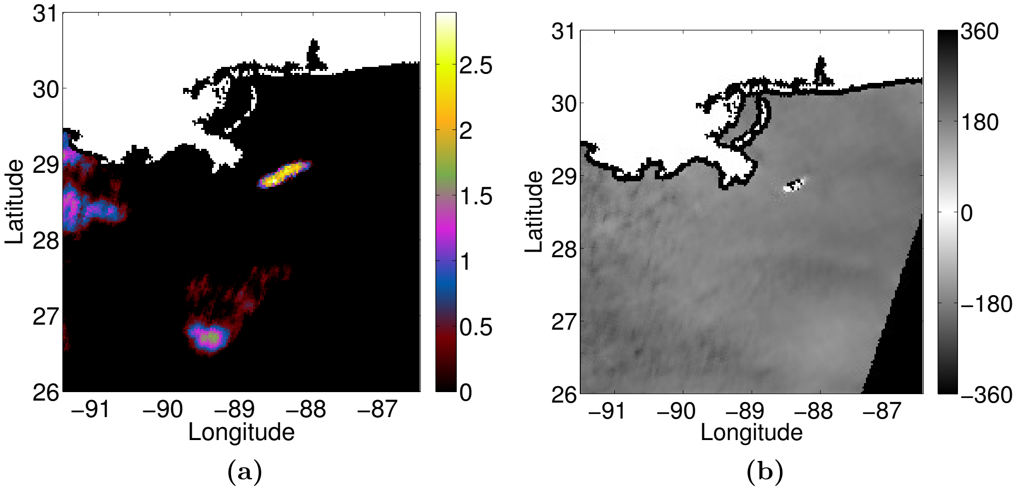

Figure 6.2: Wind speed error and wind direction error for rev 18298 (2010-04-29). No EMPSR data is available to validate oil extent for this day. Wind speed errors are clipped to positive error only, i.e., pixels with ECMWF wind speeds less than ASCAT wind speeds are set to zero. Land and near-land ocean regions are masked off.

Backscatter error

The backscatter error $\|\vec{\epsilon}\|_2$ is found for all available ASCAT passes over the oil spill. The backscatter error is shown for two ASCAT passes in Fig. 6.3b and Fig. 6.3d. Negative backscatter error is discarded in these and other figures since only positive values are anticipated to indicate surface oil. The EMPSR data is shown by the white outlines. The large backscatter errors closely match the EMPSR data.

A comparison of the various metrics used to map the oil spill is shown in Fig. 6.4. The wind speed error (a) and backscatter error (c) map the bulk of the oil similarly. The differences between the two are typical of other passes and are discussed more below. The wind direction error is shown in (b). The direction error is largely uniform except for large errors near the oil rig location (not marked in the figure). Typically, these large direction errors are not found in other locations. It appears that the wind direction error only detects regions most affected by oil. For most ASCAT passes, both wind speed error and backscatter error validate well with EMPSR data.

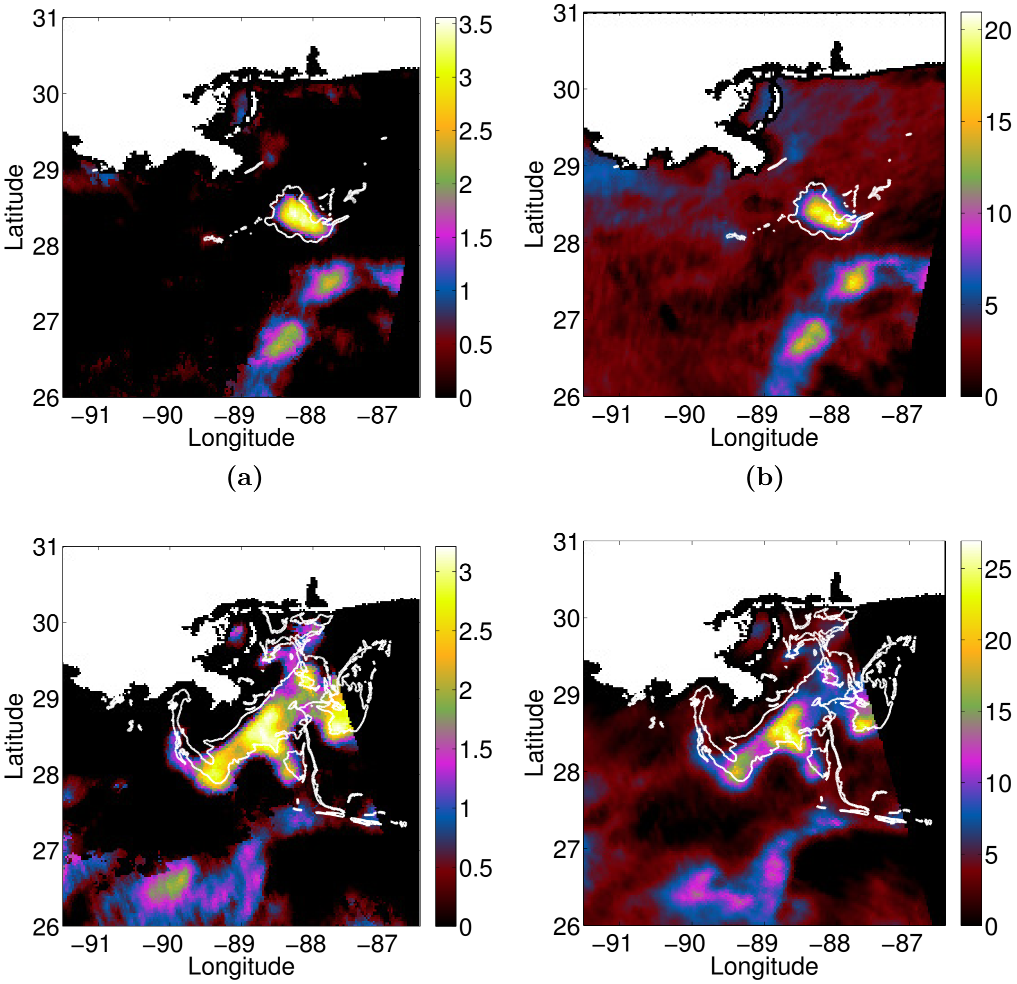

(a) (b)

(c) (d)

Figure 6.3: Wind speed and backscatter error for two ASCAT passes. The top row is ASCAT rev 19363 (2010-07-13), and the bottom row is ASCAT rev 18745 (2010-05-31). The left column shows the wind speed error and the right column shows the backscatter error. EMPSR data is included in all subfigures as a white outline for validation. Negative errors are clipped to zero, as indicated in the text.

Backscatter versus backscatter error case study

As the previous results show, mapping the oil extent using wind speed error or backscatter error is generally effective. To illustrate the advantage of finding the backscatter error rather than using only the measured backscatter, the results of ASCAT rev 19221 (2010-07-03) are presented as a case study.

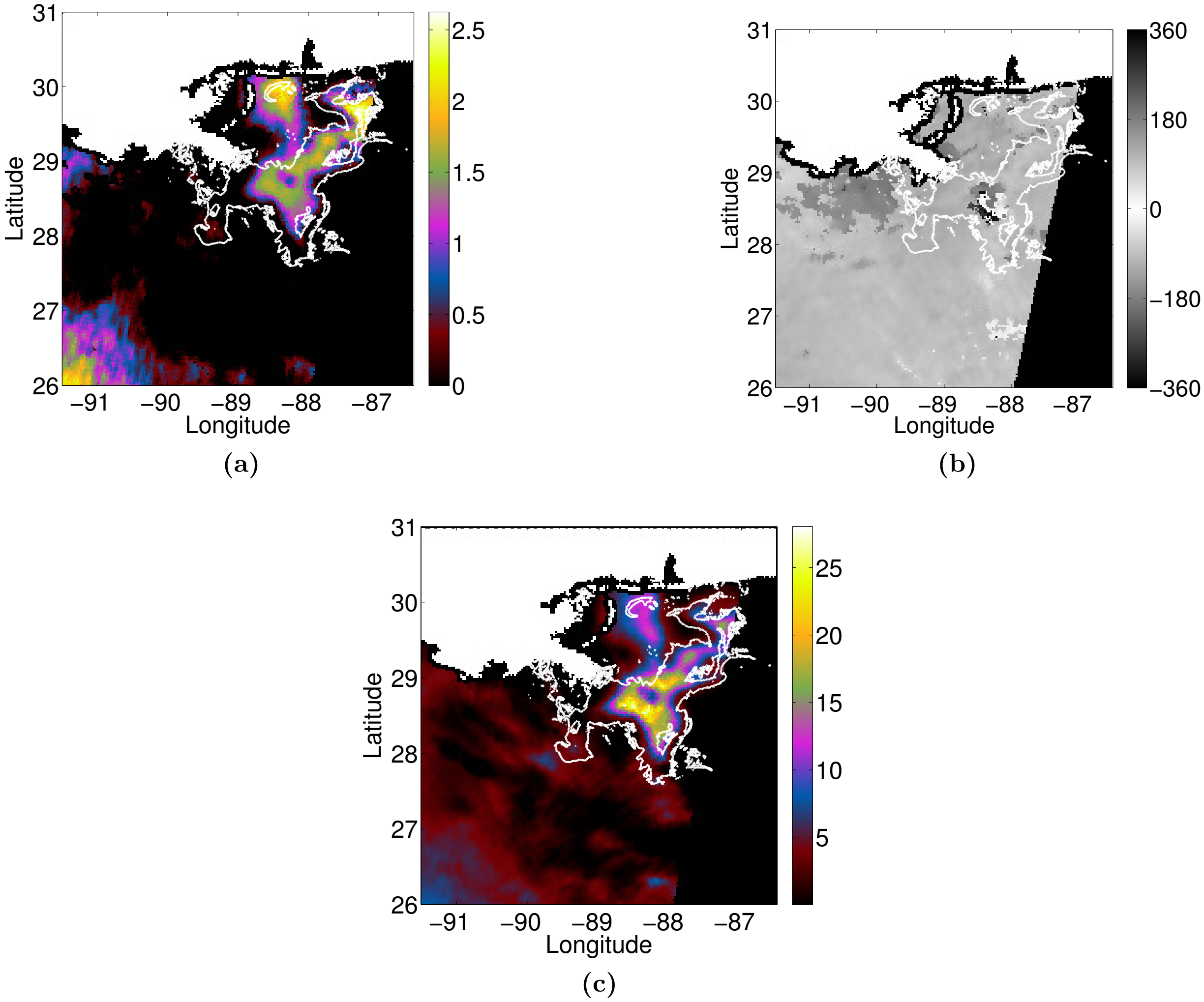

(a)

(b)

(c)

Figure 6.4: Wind and backscatter error for ASCAT rev 18880 (2010-06-09). The wind speed error is in (a), the wind direction error in (b), and backscatter error in (c). In all subfigures, the EMPSR data is outlined in white for comparison. Negative values of backscatter error and wind speed error are discarded, as explained in the text.

Figure 6.5 shows the high-resolution σ° field over each of the three looks for an ascending pass of ASCAT. In these images, two potential oil regions can be seen: one east of the Mississippi River Delta and one further south of the delta. The regions are noted with dashed ellipses. Similarly, Fig. 6.6 shows the difference between the measured and predicted backscatter for each of the three looks. In Fig. 6.6, the region south of the delta with low wind speeds is accounted for, leaving only the oil region east of the delta visible.

Without using the predicted backscatter, combining the three looks of Fig. 6.5 using the ℓ_2 norm results in Fig. 6.7a. The middle look (center image of Fig. 6.5) spans a lower

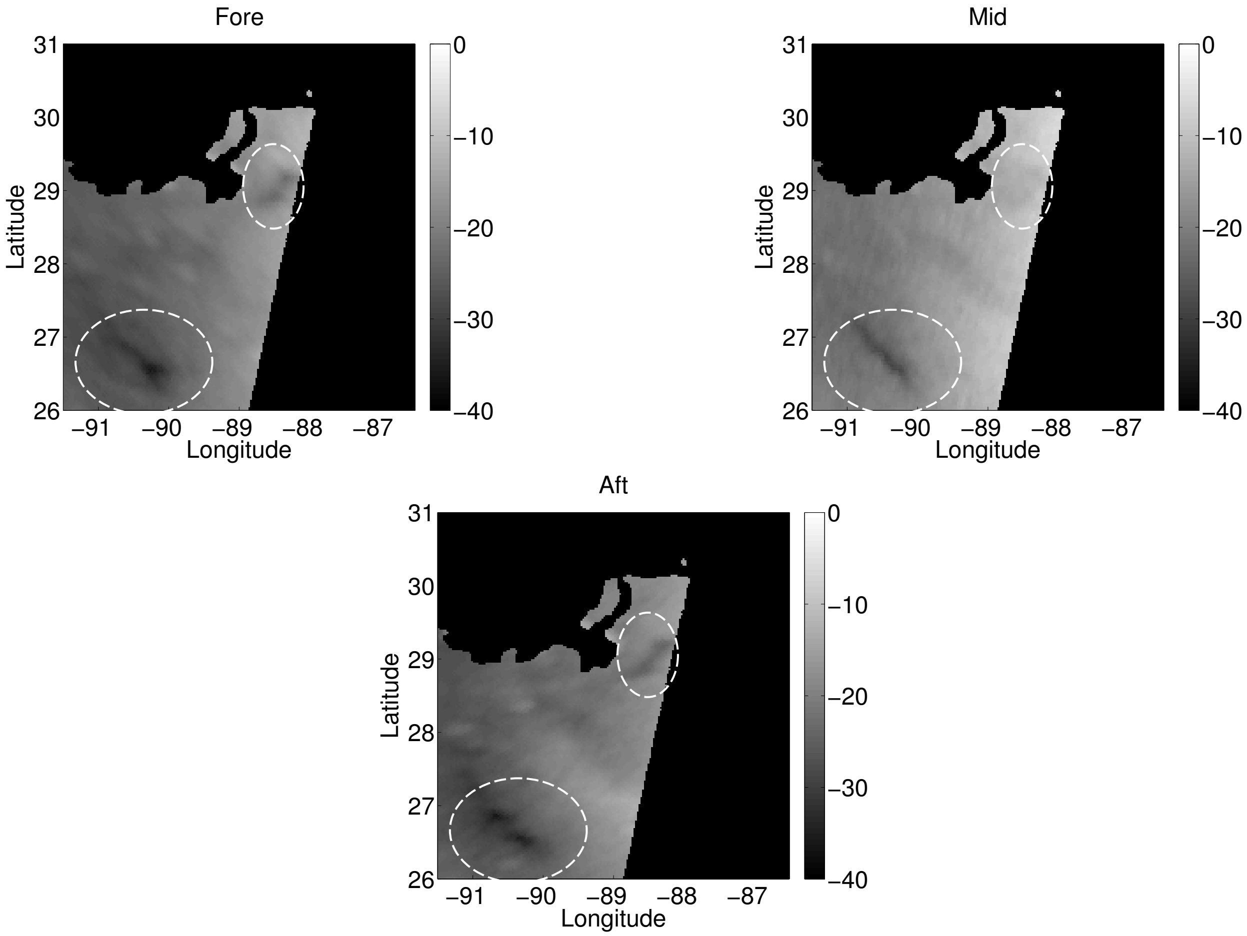

Figure 6.5: ASCAT σ° (in dB) fore, middle, and aft looks for rev 19221 (2010-07-03). Fore and aft looks span incidence angles of 36°–55°, and the middle look spans a range of 27°–44°. The fall off of σ° with incidence angle accounts for the brightness variations across the swath. The locations of the two oil spill candidate regions are indicated with dashed ellipses.

incidence angle range than the other two, leading to poor detection of the first oil candidate region. The ℓ_2 norm of the three looks has a greater value for the second candidate region than the first. The second region is a false positive due to low wind speeds in the area.

Using Eq. (6.4) to merge the three looks of Fig. 6.6 to find the backscatter error results in Fig. 6.7b. The white outline is the EMPSR product for the day. In this case, the results agree well with the largest EMPSR oil region, while the smaller regions near the coast are not as well detected.

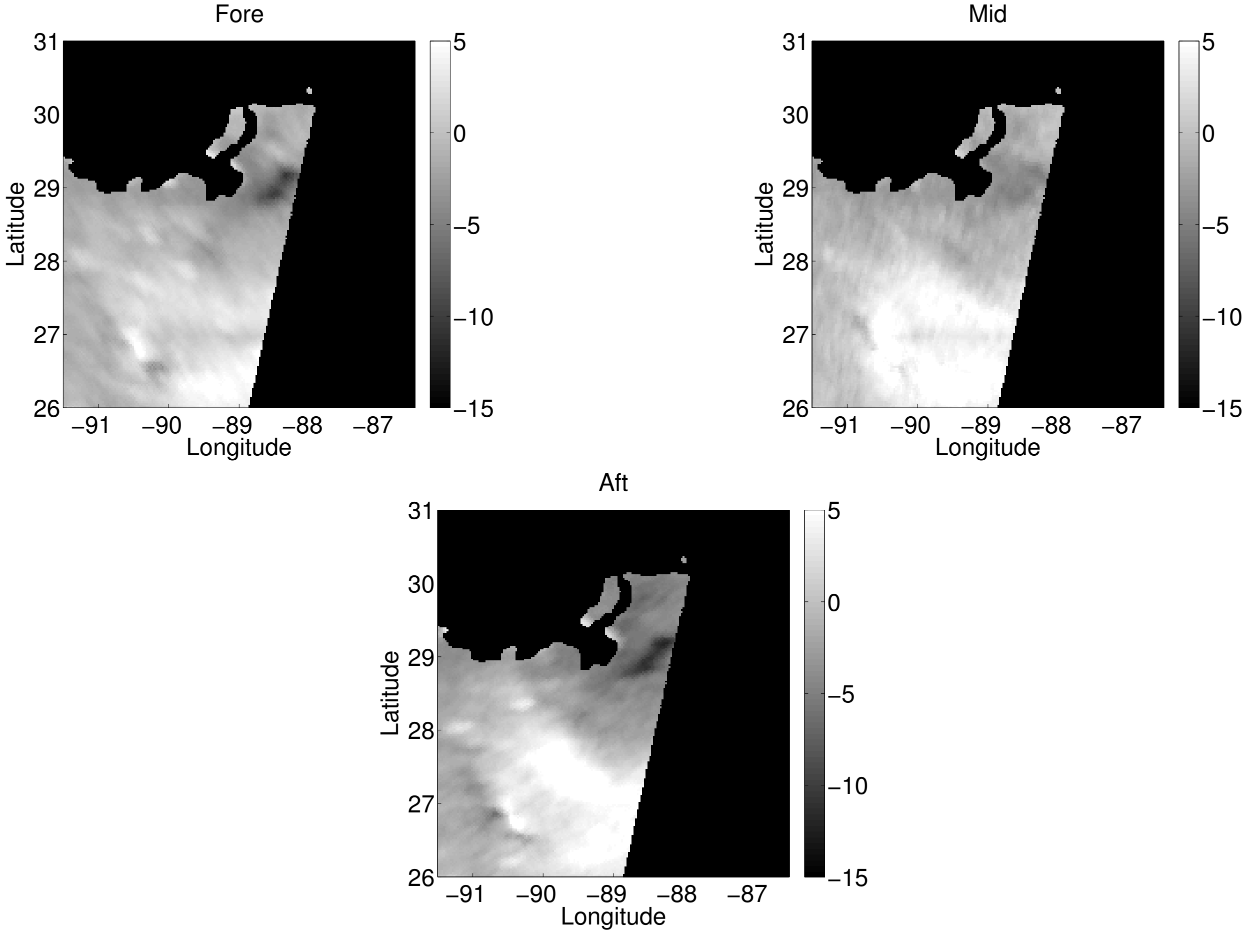

Figure 6.6: Difference in dB between measured and predicted σ° for ASCAT rev 19221 (2010-07-03). Compare with Fig. 6.5. The oil region is not as visible in the mid look due to the different incidence angle between the fore/aft and mid looks.

Discussion

The EMPSR results corroborate the thresholded wind speed error and backscatter error during the middle of the spill (late April – mid July), but they are less effective near the beginning or end of the spill. It appears that at these times, the presence of surface oil does not dampen σ° enough to be detectable by ASCAT. This could be due to the oil collection/burning efforts, weather conditions, or other factors.

Each pixel in the figures corresponds to an area of the ocean of about $20\,\text{km}^2$. It is unlikely that an area of that size is uniformly affected by oil, especially on the boundary of the spill. Thus, the true oil extent can only be approximated by ASCAT.

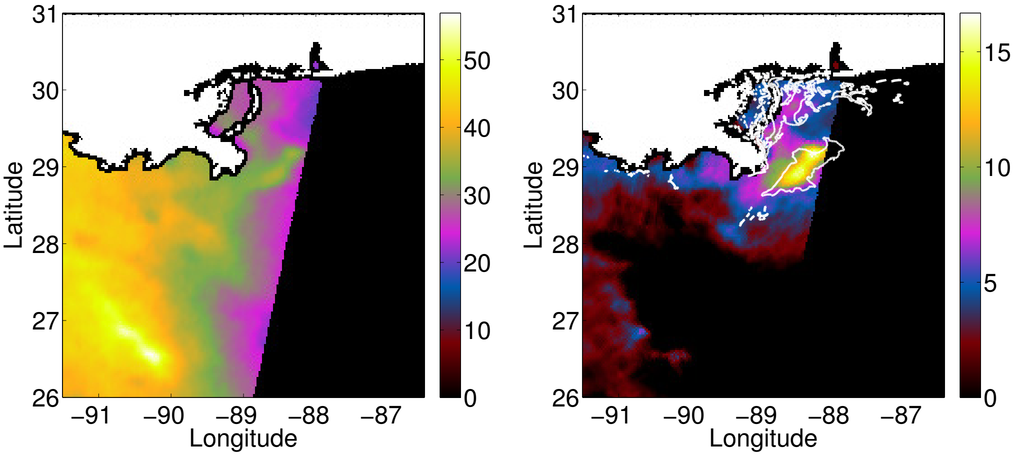

(a) **(b)**

Figure 6.7: The ℓ_2 norm of the measured σ° in (a), and the ℓ_2 norm of the difference between measured and predicted σ° in (b). Data from ASCAT rev 19221 (2010-07-03) is used, along with interpolated ECMWF winds for (b). Land is masked out and near-coastal regions are set to 0 to remove biased wind estimates. The bright area in (b) indicates dampened σ° measurements due to the presence of surface oil. The white outline is the EMPSR analysis for the surface oil extent.

The wind direction error appears to only map a much smaller extent than that mapped by the wind speed or backscatter errors. Many ASCAT passes do not have any significant wind direction error, but for the passes that do, the errors often appear near the oil rig location, perhaps correlated with regions with thicker surface oil. This hypothesis cannot be validated with EMPSR data, since no measurements of oil volume or thickness are reported in the EMPSR dataset.

Wind speed error and backscatter error each correlate well with the EMPSR oil extent. The main body of surface oil is detectable by either of these methods, but smaller regions further from the center of the spill are usually less detectable. The biggest difference between wind speed error and backscatter error is the noise floor of the non-oil regions. The backscatter error images have a much higher noise floor than the wind speed error images. However, the wind speed error images have more false positives than the backscatter error images. When finding the optimum threshold value, these false positives tend to dominate the effects of the higher noise floor in the backscatter error images.

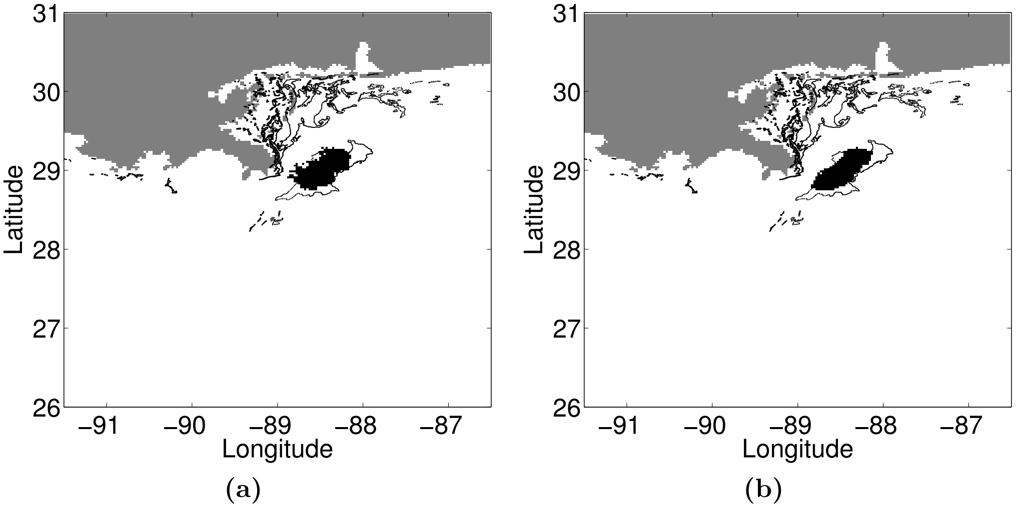

(a) **(b)**

Figure 6.8: The mapped oil extent using wind speed error (a) and backscatter error (b) for ASCAT rev 19221 (2010-07-03). The gray region is land and the black region is the error exceeding the chosen threshold. For comparison, the EMPSR region outline is overlaid on the figures as black lines.

The optimum threshold is selected for each pass, as described previously. Using this threshold, a comparison of detected oil with EMPSR data is shown in Figs. 6.8 and 6.9 for two different ASCAT passes. The chosen threshold maximizes true positives (flagged pixels within the EMPSR boundary) and minimizes false positives (flagged pixels outside the EMPSR boundary) with relative weighting controlled by α in Eq. (6.5). These results are typical of other passes. Generally, thresholded backscatter error has fewer false positives than thresholded wind speed error. A subset of the processed thresholded backscatter error images is shown in Fig. 6.10. While the oil spill is mapped well by many of the passes, other passes contain wind speed-induced oil look-alikes. The low wind speeds of these regions (about 3 m/s or less) make oil detection difficult with the methods presented here.

6.1.3 Conclusion

Though originally designed for only low-resolution ocean wind measurements, ASCAT can be used to map the surface extent of large bodies of oil on the ocean surface. The detection of ocean surface oil by active microwave instruments is based on a contrast of σ° over oil-affected areas and oil-free areas. Moderate wind speeds sufficiently roughen the ocean

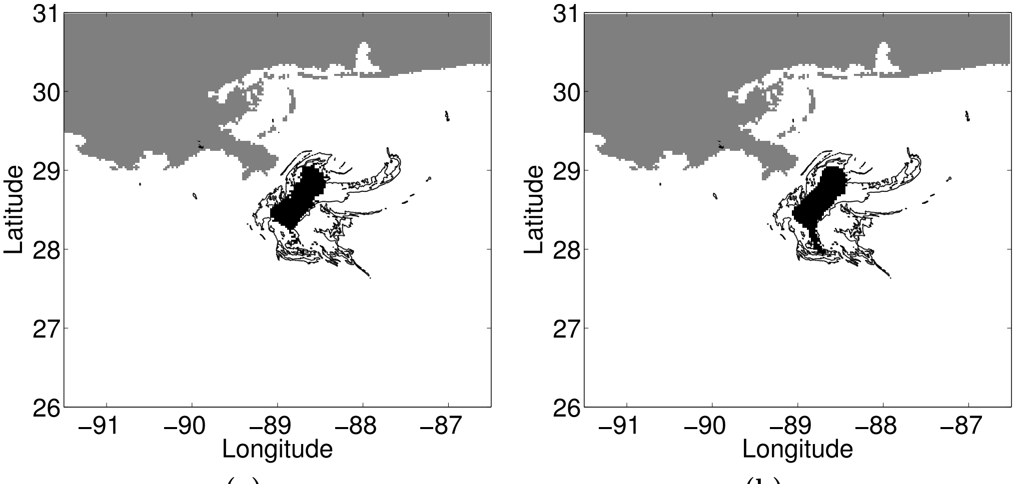

(a) **(b)**

Figure 6.9: The mapped oil extent using wind speed error (a) and backscatter error (b) for ASCAT rev 19434 (2010-07-18). The gray region is land and the black region is the error exceeding the chosen threshold. For comparison, the EMPSR region outline is overlaid on the figures as black lines.

surface to provide this contrast. A comparison of σ° values while accounting for the wind over the oil improves the detection.

Accounting for the wind may be done directly in the wind domain, or it may be done in the backscatter domain by finding the predicted backscatter based on the reference winds and the GMF. Both approaches have been explored in this chapter. The methods presented account for the near-surface wind by using the ASCAT GMF in conjunction with NWP winds to compute several oil-mapping metrics: $\epsilon_{|U_{10}|}$, the wind speed error, $\epsilon_{\angle U_{10}}$, the wind direction error, and $\| \vec{\epsilon}_{\sigma^\circ} \|_2$, the norm of the backscatter errors.

The wind speed error and backscatter error both match EMPSR products to a higher degree than wind direction error. While the amount of true positives are typically similar between the two, wind speed error generally has more false positives than backscatter error and backscatter error exhibits a higher noise floor. Both metrics are useful for mapping surface oil extent, but using a binary threshold to categorize the pixels generally is more effective using thresholded backscatter error. The wind direction error $\epsilon_{\angle U_{10}}$ may provide some indication of where the surface oil is most dense.

Figure 6.10: A selected time-series of mapped oil. Each image is the thresholded backscatter error for the date indicated in the upper left corner. The ASCAT pass may not completely cover the region on a given day, leading to a diagonal crop in some of the images.

Small oil regions in EMPSR data are not usually resolvable in wind speed and backscatter errors. However, the main body of surface oil is mapped effectively. The backscatter error and wind speed error results presented show a good match with conventional oil detection techniques making use of multiple sensors as reported in the EMPSR product. False positives, or oil look-alikes still arise owing to the limitations of working with a single instrument, but the occurrence of wind-related false alarms is diminished. Results validate well with EMPSR results except for the very beginning and end of the spill.

The oil spill mapping presented in this section is a novel application of scatterometer data. Oil spill detection with a scatterometer is only suitable for the rare large-area event such as the Deepwater Horizon spill. Thus, scatterometers have not been previously used to map oil spills. The use of NWP winds to reduce false positives in the oil detection process is also a novel application. Oil spill detection with SAR data has previously used wind speed in order to account for low-wind-speed oil look-alikes, but these wind speeds are usually obtained from the SAR data itself or from collocated scatterometer measurements.

6.2 Azimuth Angle Modulation

Each σ° measurement from a scatterometer has an associated incidence angle θ and azimuth angle ϕ. For most land and ice surfaces, σ° depends only on incidence angle, not on azimuth angle. However, in regions of East Antarctica associated with megadunes and sastrugi, a strong azimuth dependence is induced due to the physical structures [20]. Conversely, wind-glaze regions in Antarctica are expected to have little azimuth modulation [1]. This azimuth angle modulation has been modeled previously as a second- or fourth-order Fourier series [19–21, 37, 74].

Previous work has explored the azimuth modulation of scatterometer data. Data from the ASCAT scatterometer are used in [19], where a variety of models are evaluated to fit the incidence and azimuth angle dependence of the σ° data. Physical interpretations for the observed azimuth variation are explored in [20, 75] using data from the QuikSCAT and ERS scatterometers. Modeling the azimuth modulation as a Fourier series, the first-order term typically correlates with the local slope of the surface whereas the second-order term correlates with sastrugi carved into the ground due to persistent katabatic winds.

An important application azimuth angle modulation of Antarctica is to map the distribution of physical structures such as sastrugi or wind glaze over the Antarctic ice sheet. Wind-glaze areas, for example, represent areas with a near-zero change in surface mass balance: the accumulation and ablation of snow and ice over these regions nearly equals each other [1]. Until recently these local lows in surface mass balance were not included in estimates of the changes in the Antarctic ice sheet. Accounting for these regions revises estimates of the changes in Antarctica, which in turn are indications of climate change.

Although this dissertation focuses on the ASCAT scatterometer, for comparison in this chapter, data from the QuikSCAT scatterometer is also considered. QuikSCAT (1999–2009) is a scanning pencil-beam scatterometer at Ku band (13.4 GHz). Because of its different measurement geometry, QuikSCAT observes σ° at only two incidence angles (47° and 54°) but has complete azimuth angle coverage. ASCAT, as described in Chapter 2, covers a wide range of incidence angles but only a few azimuth angles. While ASCAT only measures σ° at vertical polarization (VV), QuikSCAT measures both vertically and horizontally polarization (VV and HH) σ°. QuikSCAT reports two types of measurements: “egg” data, where the measurement SRF is essentially the antenna response, and “slice” data, which subdivides the antenna pattern using range-Doppler processing [76]. Slice data has a finer spatial resolution but is noisier than egg data.

In this section the azimuth modulation of ASCAT and QuikSCAT data is described using a Fourier series fit. Enhanced-resolution σ° reconstruction using the AVE algorithm is applied in conjunction with the SRF to estimate the incidence and azimuth dependence of σ° for each pixel. The backscatter model used in this section is reviewed in Section 6.2.1 and the procedure to estimate the azimuth modulation model parameters is described in Section 6.2.2. Results are shown in Section 6.2.3. Section 6.2.4 concludes.

6.2.1 Backscatter Model

The dependence of σ° on θ over land and ice is modeled as a linear fit, described by Eq. (2.14) and repeated here for convenience:

$$\sigma^\circ(\theta) = \mathcal{A} + \mathcal{B}(\theta - 40^\circ). \tag{6.6}$$

Since QuikSCAT does not have sufficient incidence angle coverage, QuikSCAT $\mathcal{B}$ is treated as zero and $\mathcal{A}$ is simply the mean σ° for the pixel. A previous azimuth modulation study [20] uses an M-order Fourier series to fit the residual backscatter after estimation of $\mathcal{A}$ and $\mathcal{B}$:

$$\sigma^\circ(\theta,\phi) = \sigma^\circ(\theta) + \sigma^\circ(\phi) \tag{6.7}$$

$$= \mathcal{A} + \mathcal{B}(\theta - 40^\circ) + \sum_{k=0}^{M} B_k \cos(k\phi) + C_k \sin(k\phi). \tag{6.8}$$

To aid in interpreting the results, the sine and cosine coefficients are converted from a rectangular coordinate system to polar coordinates:

$$m_k = \sqrt{B_k^2 + C_k^2} \tag{6.9}$$

$$\varphi_k = \tan^{-1}(C_k/B_k). \tag{6.10}$$

Thus m_k and φ_k are the k-th order azimuth modulation magnitude and phase, respectively. (The term B_0 is an azimuth-modulation bias and is expected to be small; C_0 is defined to be zero.) Although several azimuth modulation models were considered, in this chapter a fourth-order Fourier series is used with the third-order terms set to zero.

6.2.2 Model Parameter Estimation

The estimation of the model parameters is performed in two steps. First, the σ° measurements are corrected to remove the mean value and θ dependence (i.e., the $\mathcal{A}$ and $\mathcal{B}$ values). Then, from the residual σ° values, the azimuth dependence is estimated. Let the vectors $\vec{\sigma_j^\circ}$, $\vec{\theta_j}$, $\vec{\phi_j}$ and $\vec{h_j}$ represent the measurement values and SRF values for pixel j. These are processed using the AVE reconstruction algorithm (described in Section 2.3.3 by Eq. (2.26) and applied to ASCAT data in Chapter 4) to estimate $\mathcal{A}$ and $\mathcal{B}$ for each high-resolution pixel j.

After estimation of $\mathcal{A}_j$ and $\mathcal{B}_j$, the azimuth modulation coefficients for the pixel are computed using a linear least-squares approach. The matrix equation

$$A\mathbf{x} = \mathbf{b} \tag{6.11}$$

is solved for $\mathbf{x}$ in the least-squares sense. The vector $\mathbf{x}$ contains the coefficients to estimate:

$$\mathbf{x} = [B_0, B_1, C_1, B_2, C_2, B_4, C_4]^T, \tag{6.12}$$

and the vector $\mathbf{b}$ contains the residual σ° values after correcting for the estimated $\mathcal{A}$ and $\mathcal{B}$ values:

$$\mathbf{b} = \vec{\sigma_j^\circ} - \mathcal{A}_j + \mathcal{B}_j(\vec{\theta_j} - 40^\circ), \tag{6.13}$$

and the matrix A contains column vectors:

$$A = [\vec{1}\ \cos(\vec{\phi_j})\ \sin(\vec{\phi_j})\ \cos(2\vec{\phi_j})\ \sin(2\vec{\phi_j})\ \cos(4\vec{\phi_j})\ \sin(4\vec{\phi_j})\ ]. \tag{6.14}$$

Since the length of the column vectors is much larger than 7 (there are 7 coefficients to estimate), the system of equations is overdetermined. The equation $A\mathbf{x} = \mathbf{b}$ is solved for x in the least-squares sense (e.g., through decomposition of A using QR or SVD).

However, in order to incorporate information about the SRF values, the formulation above is modified to weight the measurements by their SRF values. The normal equations are updated to

$$A^T A\mathbf{x} = A^T\mathbf{b} \Rightarrow A^T H A\mathbf{x} = A^T H\mathbf{b}, \tag{6.15}$$

where H is the diagonal matrix that contains the SRF values h_{ij} for the pixel j:

$$H = \begin{bmatrix} h_{1j} & & & \\ & h_{2j} & & \\ & & \ddots & \\ & & & h_{Mj} \end{bmatrix}. \tag{6.16}$$

Now, instead, the matrix equation

$$B\mathbf{y} = \mathbf{c} \tag{6.17}$$

is solved for $\mathbf{y}$ using a least-squares approach, where $B = A^T H A$, $\mathbf{y} = \mathbf{x}$, and $\mathbf{c} = A^T H\mathbf{b}$.

Table 6.1: The estimated azimuth modulation magnitude and phase coefficients for the data shown in Fig. 6.11. The m_k terms are in dB and the φ_k terms are in degrees.

Coef.	ASCAT	Egg	Slice
m_1	1.42	1.13	1.31
m_2	4.97	2.65	2.58
m_4	1.77	1.49	1.68
φ_1	154	−46	−47
φ_2	87	92	95
φ_4	−165	−164	−161

6.2.3 Results and Discussion

ASCAT and QuikSCAT data are collected over the Antarctic region for the same date range: days 211–240, 2009 (2009-07-30 to 2009-08-28). This 30-day range is during the Austral winter when no significant melt or refreeze is expected. For comparison to ASCAT, only the VV data from QuikSCAT is used. AVE on a 3.125 km grid spacing is used to estimate the azimuth modulation coefficients. GRD on a 12.5 km grid spacing is also performed to estimate the azimuth modulation parameters at conventional resolution.

Pixel results

A single high-resolution pixel is first selected, located at $-67.99\,^\circ$N $126.48\,^\circ$E. The residual backscatter (i.e., after removing the estimated $\mathcal{A}$ and $\mathcal{B}$ values) at this pixel as a function of azimuth angle is shown in Fig. 6.11 for ASCAT, QuikSCAT eggs, and QuikSCAT slices. The fourth-order Fourier series fit is also displayed, and the estimated coefficient values listed in Table 6.1. In Fig. 6.11, the difference in sampling geometry between ASCAT and QuikSCAT is apparent: for ASCAT, only a few groups of azimuth angles are sampled, but the QuikSCAT azimuth angle coverage is much more dense, with no large gaps present. The QuikSCAT slice values are also much noisier than the QuikSCAT egg values: the residual backscatter values have more vertical spread. Notwithstanding the noise, the Fourier series fits for the two QuikSCAT cases are similar in this case. (This is not true for all pixels in the region.)

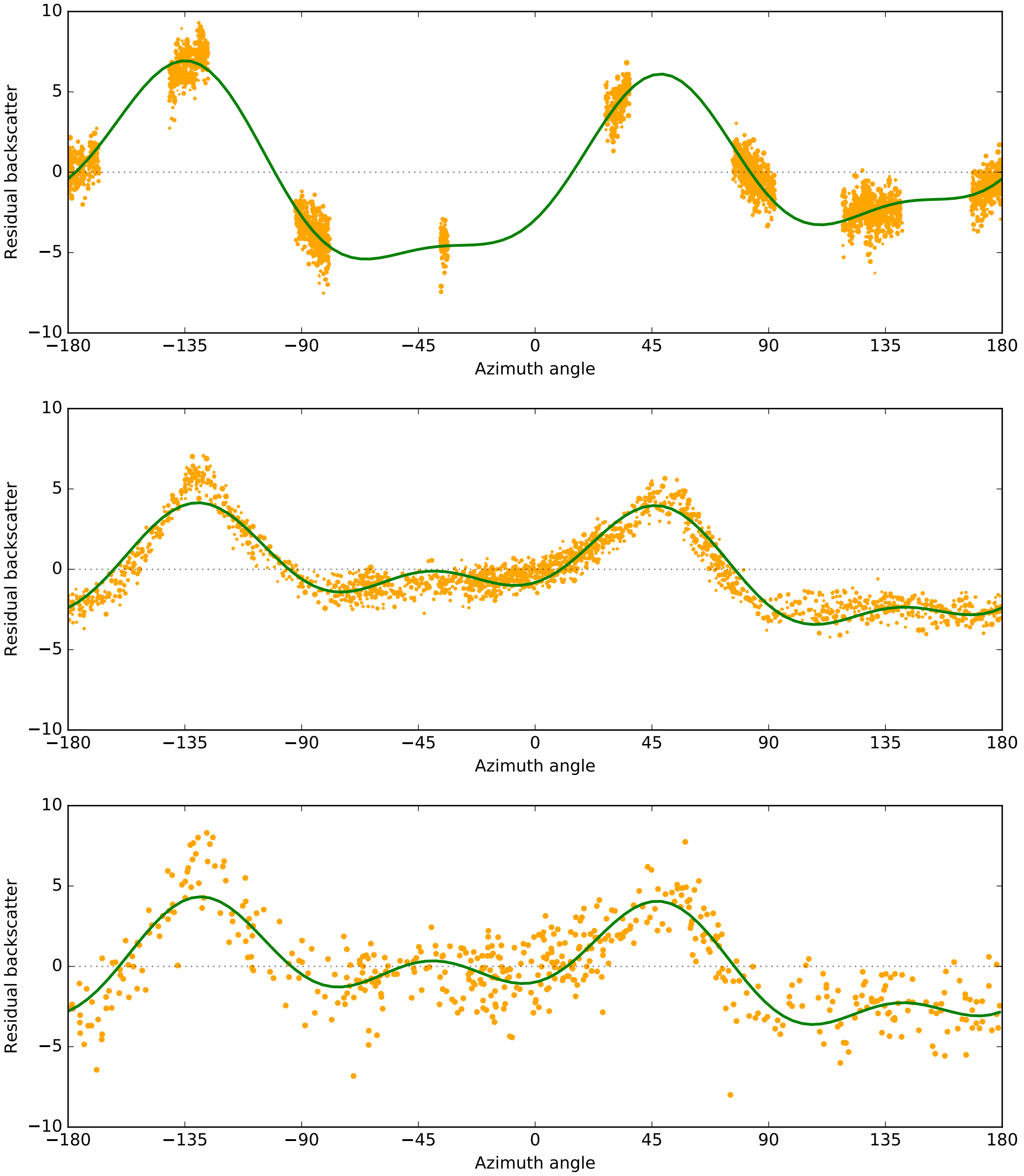

Figure 6.11: Residual backscatter values and fourth-order Fourier series fit to the data. Top to bottom: ASCAT, QuikSCAT eggs, QuikSCAT slices.

Comparing the ASCAT and QuikSCAT values, in all three cases two large peaks are present at about −135° and 45°; however, ASCAT does not have any σ° measurements directly at the center of the 45° peak, only on either side. Conversely, the valley between −90° and 0° is much lower for ASCAT, at about −5 dB, than for QuikSCAT, at about −1 dB. Also, between about 120° and −160°, the QuikSCAT data has a "valley" at about −3 dB, but for ASCAT, it starts to slope upward at 135°. While the two peaks are similar in position and magnitude, the behavior between the peaks is different for QuikSCAT and ASCAT, leading to different estimated values, most significantly larger estimated magnitude terms m_k.

Region results

The azimuth modulation parameters are estimated for the entire Antarctic region, masking out ocean and sea ice. Figure 6.12 displays m_1, m_2, and m_4, the modulation magnitudes, and Fig. 6.13 displays φ_1, φ_2, and φ_4, the modulation phases. Only ASCAT and the QuikSCAT egg data are shown, because the QuikSCAT slice data (not shown) is too noisy.

For all images shown in Figs. 6.12 and 6.13, the estimated values are less accurate closer to the South Pole at the center of the images. This is due to the polar orbits of QuikSCAT and ASCAT and their measurement geometry. South of about 78 ° S, the Earth is only measured by one of the two ASCAT swaths, and south of about 89 ° S, neither swath observes the Earth surface. Between these two latitudes, ASCAT samples σ° at fewer azimuth angles, so the estimated coefficients are less reliable since they suffer from over-fitting. A circular discontinuity is visible at 78 ° S. QuikSCAT does not have such a sharp discontinuity, but it still samples fewer azimuth angles at extreme latitudes, leading to poor estimates of the azimuth modulation parameters.

As illustrated for one pixel in Fig. 6.11, the second-order magnitude is generally much larger than the first-order and fourth-order magnitudes. This is visible in Fig. 6.12, where different colorbar ranges are used. Also observed in Fig. 6.11 and tabulated in Table 6.1 for a single pixel, the m_1, m_2, and m_4 values are smaller for QuikSCAT than for ASCAT. This holds true in Fig. 6.12 for the entire region, where the modulation magnitudes are larger from ASCAT than from QuikSCAT. In Fig. 6.13, the estimated phases φ_2 and φ_4 are

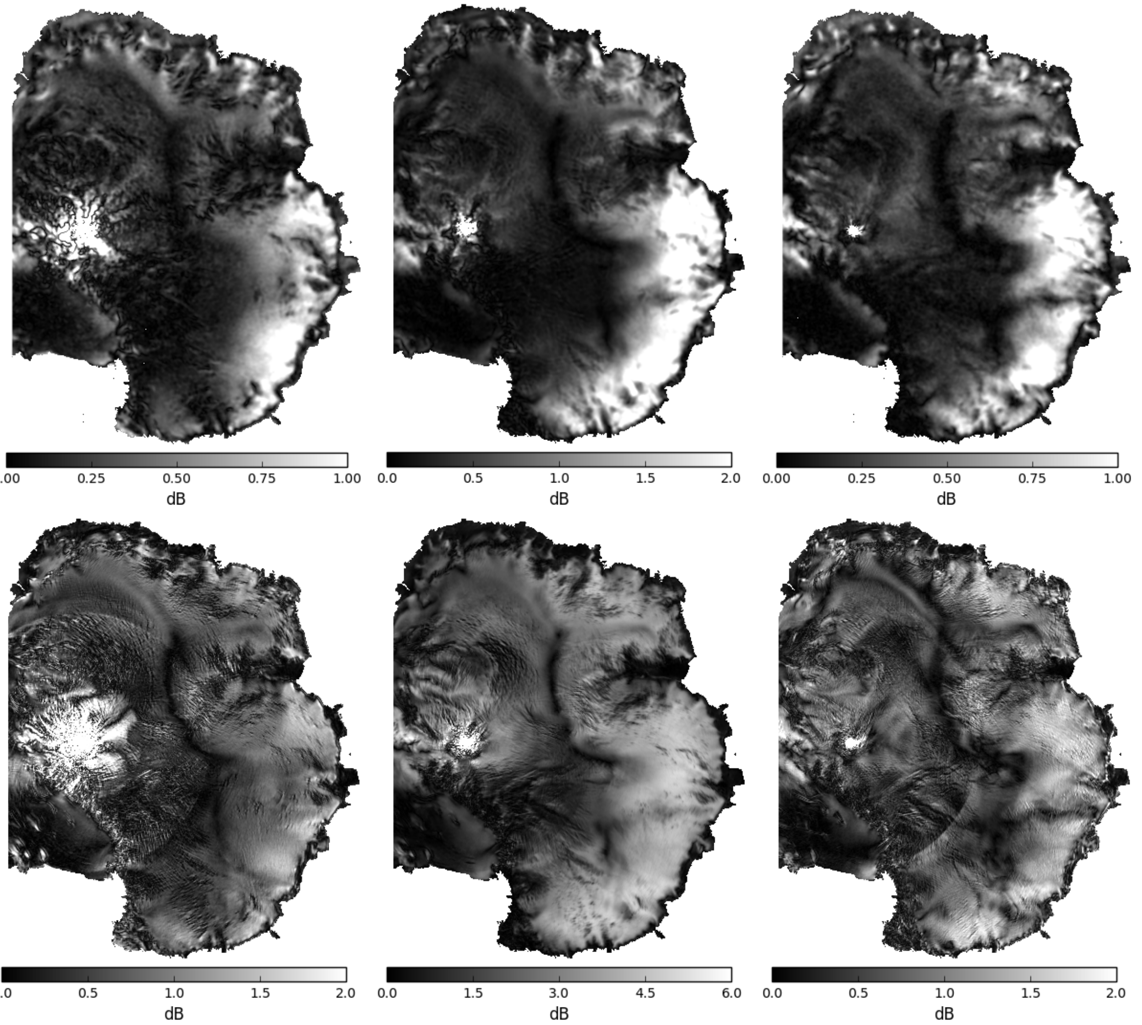

Figure 6.12: The m_1 (left column), m_2 (middle column), and m_4 (right column) azimuth modulation coefficients over Antarctica, 30 days of data. Top row: QuikSCAT eggs, bottom row: ASCAT.

very similar between QuikSCAT and ASCAT. However, the QuikSCAT-derived φ_1 images are often roughly 180° different from ASCAT. The larger modulation magnitude at C band versus Ku band was previously noted in [37] for Greenland, although a comparison was not conducted for Antarctica.

The azimuth modulation parameters estimated from ASCAT and QuikSCAT data share many common features. Areas of higher or lower magnitude, for example, are present in both cases. The consistency of the behavior of magnitudes and phases between ASCAT and QuikSCAT is evidence that the observed azimuth angle modulation is not a scatterometer

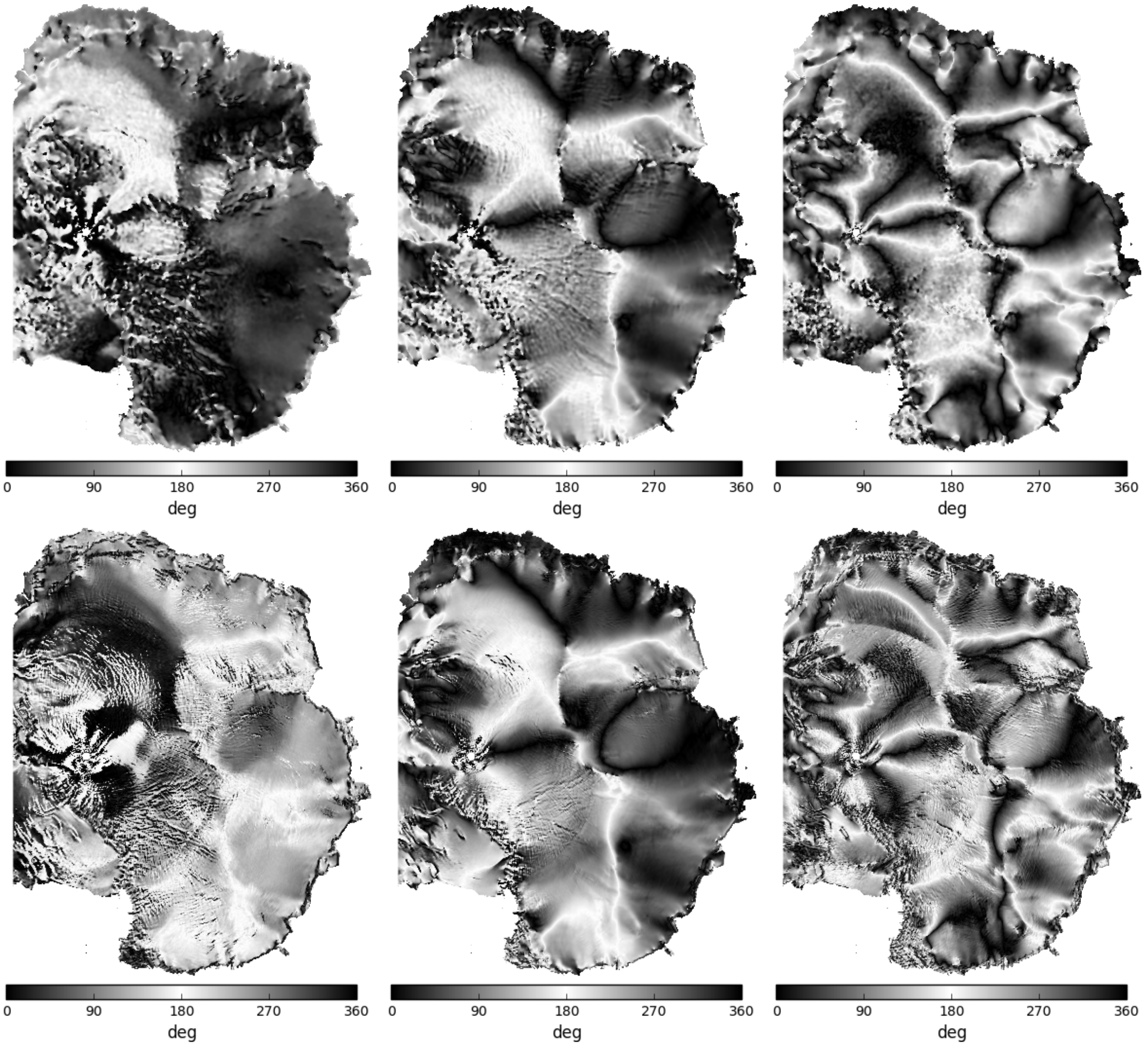

Figure 6.13: The φ_1 (left column), φ_2 (middle column), and φ_4 (right column) azimuth modulation coefficients over Antarctica, 30 days of data. Top row: QuikSCAT eggs, bottom row: ASCAT.

calibration error or a sampling artifact, but it is due to shared geophysical structures. However, differences exist between the terms estimated by ASCAT and QuikSCAT, even though the two scatterometers observe the same region over the same time range.

The source of the differences is hypothesized to be geophysical. QuikSCAT operates at a wavelength of 2.2 cm, whereas ASCAT is at 5.7 cm. The structures in the Antarctic ice sheet that are responsible for azimuth modulation (e.g., sastrugi and megadunes) scatter more strongly at the C-band wavelength of ASCAT than at the Ku-band wavelength of QuikSCAT.

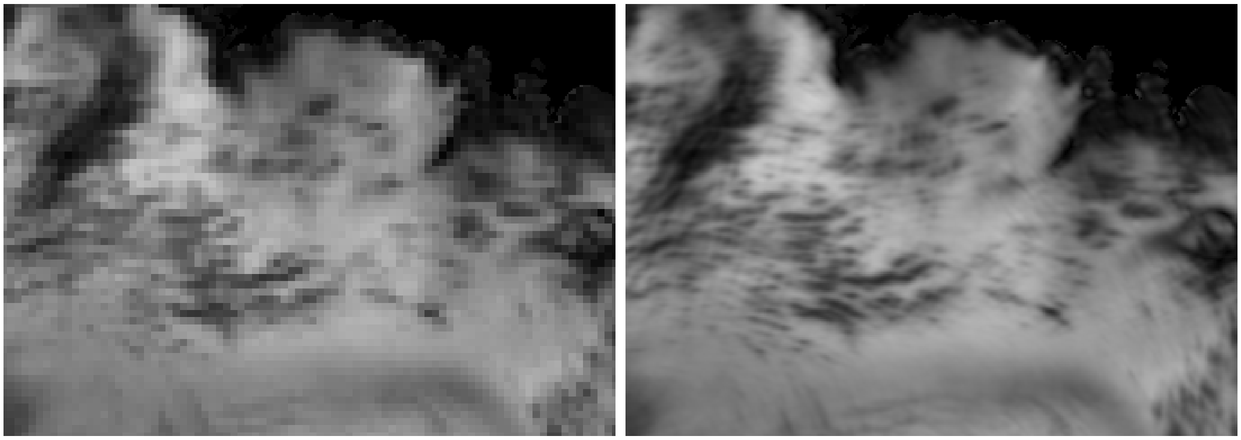

Figure 6.14: A region in Enderby Land. Left: m_2 using GRD on a 12.5 km grid, right: m_2 using AVE on a 3.125 km grid. Color scale ranges from 0 dB to 6 dB.

Additionally, the penetration depth of snow and ice is more shallow for QuikSCAT than ASCAT, so ASCAT is subject to more volume scattering than QuikSCAT.

Further study is warranted to understand the reasons behind the differences in azimuth modulation observed by QuikSCAT and ASCAT. However, the enhanced-resolution estimation of the modeled azimuth modulation parameters is an important step. Both QuikSCAT and ASCAT data are consistently produced on the same high-resolution grid using the same Fourier series estimation.

Resolution comparison

The smaller grid spacing of the enhanced-resolution images (AVE on a grid spacing of 3.125 km) versus the conventional-resolution images (GRD on a grid spacing of 12.5 km) enables resolving smaller features. Two examples each comparing the AVE and GRD m_2 images are shown in Figs. 6.14 and 6.15. The m_2 coefficient is selected for display due to its large range. While the m_2 values are very similar for both AVE and GRD, many small features evident in the AVE images are less clearly defined or not present at all in the GRD images.

Figure 6.14 contains a region from Enderby Land, where there are many small "spots" of low m_2 value within a larger area of higher m_2 value. These spots are much better defined in the AVE image at 3.125 km. In the center-left of the image is a cluster of many spots,

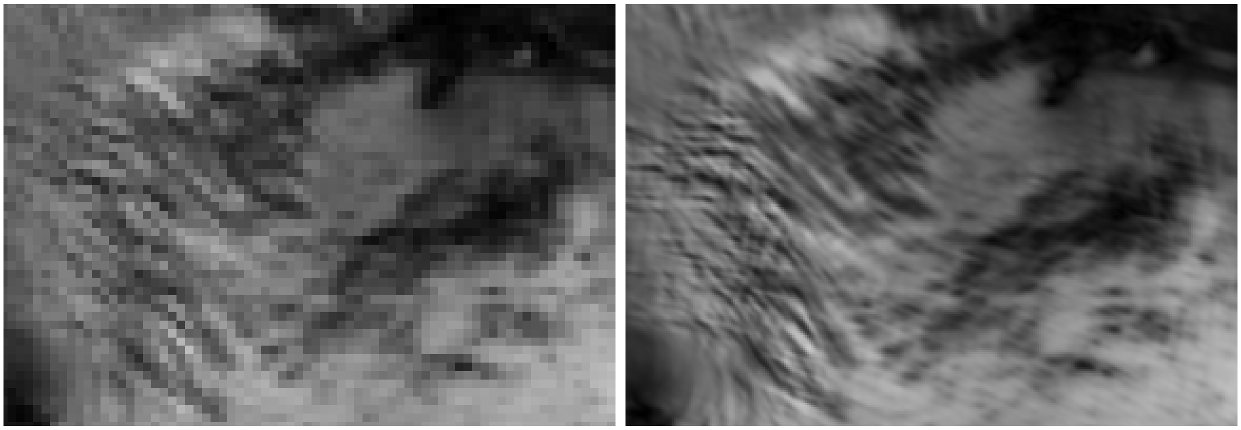

Figure 6.15: A region near MacRobertson Land. Left: m_2 using GRD on a 12.5 km grid, right: m_2 using AVE on a 3.125 km grid. Color scale ranges from 0 dB to 6 dB.

which in the GRD image at 12.5 km cannot be individually separated but which are resolvable in the AVE image.

Figure 6.15 shows a region near MacRobertson Land and contains some similar features. As with Fig. 6.14, many darker regions appear surrounded by a lighter background, and the ability to resolve these features is improved using AVE rather than GRD. In the GRD image, many of these spots merge together, but they are individually defined in the AVE image. In the center left are “ripples” with varying wavelengths of about 18 km to 35 km.

For most of East Antarctica, the azimuth modulation model parameters do not change significantly on the scale of about 50 km or less. However, there are some regions where the 3.125 km grid spacing is a clear benefit versus the 12.5 km spacing, such as shown in Figs. 6.14 and 6.15. Although the resolution improvement is not needed for the entire region, the AVE method has a lower pixel variance (see Section 4.4) and helps reduce noise since more measurements are used per pixel than GRD.

Wind-glaze regions

A geophysical feature in East Antarctica of interest is the existence of wind-glaze regions. These are areas where the snow surface is polished smooth by blowing snow. Wind-glaze regions are expected to exhibit little to no azimuth modulation [1]. A map indicating wind-glaze regions is shown in Fig. 6.16.

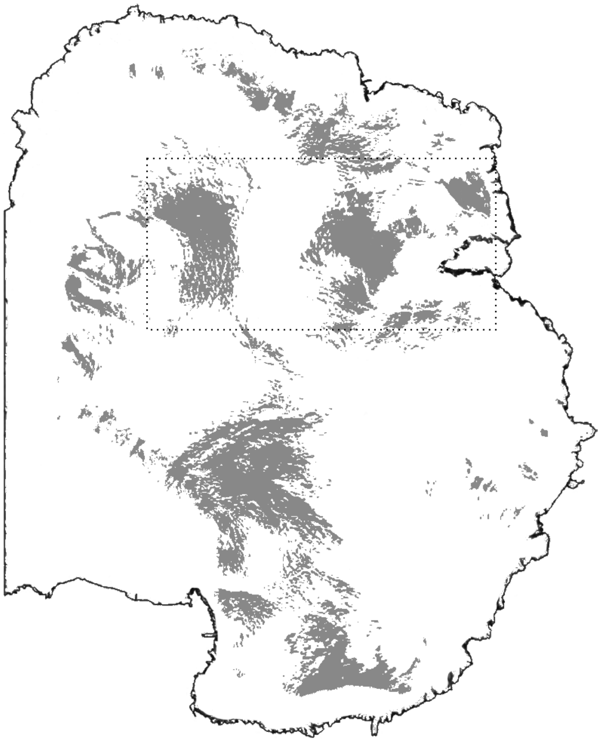

Figure 6.16: Regions of East Antarctica, where the shaded areas indicate regions containing wind glaze. Adapted from [1].

From Fig. 6.16, two areas of wind glaze are selected, as indicated by the dotted box. The ASCAT and QuikSCAT modulation magnitude parameters are shown in Fig. 6.17. The left sides of the images contain a wind-glaze region. The wind-glaze region is most identifiable in the ASCAT m_2 image. Within the wind-glaze region, the m_2 values are lower but contain significant variability. The wind-glaze region at the right of the images also has lower m_k values but retains a great deal of texture. The affected region appears smaller than that mapped in Fig. 6.16.

Most wind-glaze regions are identifiable in the m_2 images due to lower values and a spotted appearance. Other regions, however, still exhibit a large degree of azimuth modulation.

Although the wind-glaze regions mapped in [1] are visible to some extent in the azimuth modulation magnitude images, the values of the ASCAT m_2 parameter subjectively most resemble the wind-glaze regions. Within the mapped regions, the azimuth modulations values are not uniformly dampened: large values of azimuth modulation occasionally exist and significant "spotting" and other texture is also present at these locations. This suggests a

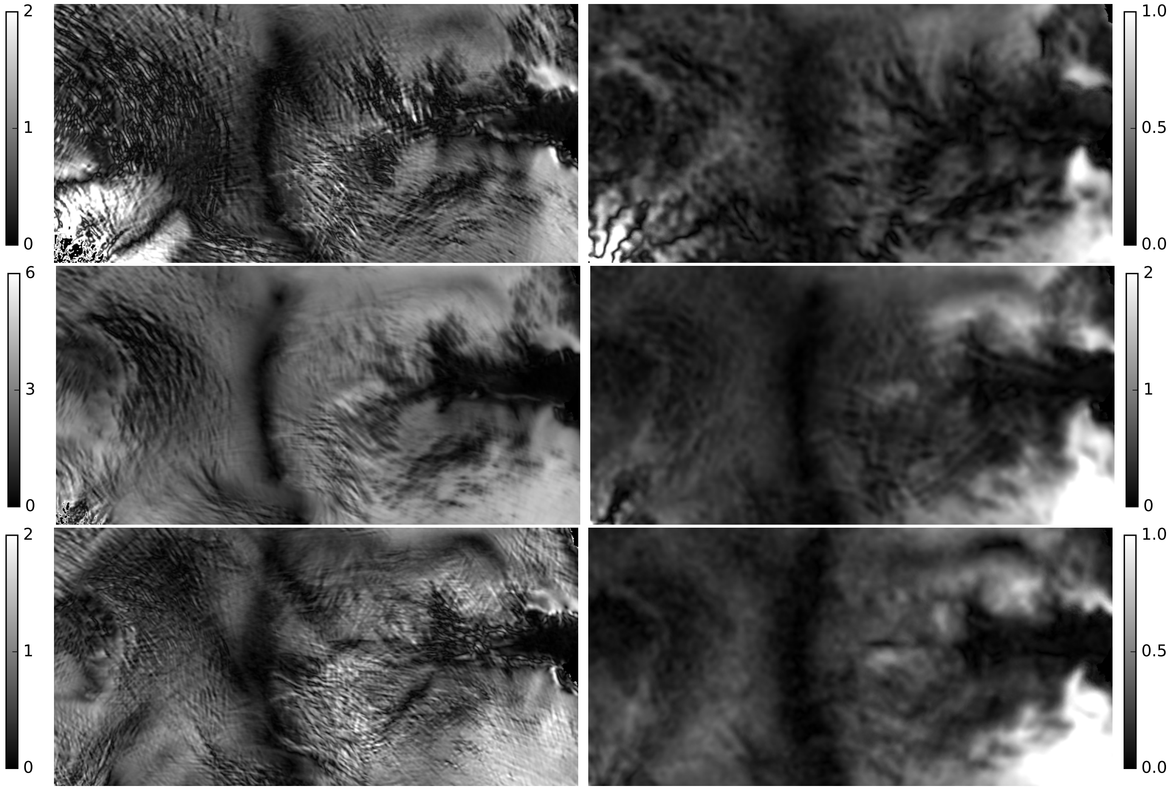

Figure 6.17: ASCAT (left column) and QuikSCAT egg (right column) m_1 (top), m_2 (middle), and m_4 (bottom) images over the area contained by the dotted box in Fig. 6.16. Note that color scales for the images differ to increase image contrast.

more complicated behavior at these regions, possibly indicating the coexistence of sastrugi or other features so that the mapped wind-glaze regions are not spatially uniform as suggested by [1].

6.2.4 Conclusion

While σ° does not vary as a function of azimuth angle for most land regions, for East Antarctica, σ° is strongly dependent on the azimuth angle. This is due to geophysical features in the Antarctic ice sheet that strongly scatter back microwave energy depending on the look angle.

The azimuth modulation, or anisotropy, in the observed scatterometer σ° data over East Antarctica is modeled with a Fourier series. This is an extension of the AVE method that permits high-resolution estimation of the Fourier series model parameters. Both ASCAT and QuikSCAT data are considered, although QuikSCAT slice data is ultimately not used due to its noise.

The estimated azimuth modulation magnitude and phase terms are very similar when comparing ASCAT and QuikSCAT data, though some differences exist. A large difference is that the ASCAT data exhibit a much larger azimuth modulation magnitude than the QuikSCAT data. This is attributed to geophysical structures that are azimuthally anisotropic, yet play a larger role at C-band (5.7 cm) for ASCAT than at Ku-band (2.2 cm) for QuikSCAT.

Previously mapped wind-glaze regions are also evaluated for azimuth modulation. I find in both ASCAT and QuikSCAT data that though less azimuth modulation is typically present within regions of wind glaze, the regions exhibit significant variability. Some pixels (each with an area of $9.8\,\mathrm{km}^2$) may contain a magnitude of modulation several dB.

The results presented here demonstrate the consistency of East Antarctic backscatter azimuth modulation at two radar bands and also illustrate the differences. Further, regions of wind glaze are shown to contain variable azimuth modulation. Future work to better explain the reasons for the differences at C and Ku bands is needed.

Chapter 7

Conclusion

7.1 Summary

This dissertation addresses the production of enhanced-resolution data from the ASCAT scatterometer and describes some geoscience applications of these results. Chapter 1 describes the scope of this dissertation and Chapter 2 presents background information for this work. The ASCAT measurement spatial response function (SRF) is discussed in Chapter 3. The major components that affect the SRF are presented in order to model the SRF. This serves as a reference from which a parameterized SRF approximation is developed. The parameterized SRF is much faster to compute and has negligible approximation error for its applications in this dissertation. Both SRF estimates are validated to ensure their accuracy.

The SRF is used for the AVE and SIR image reconstruction algorithms in Chapter 4. These algorithms reconstruct the σ° of the Earth's surface based on the ASCAT measurements. They are also evaluated along with the conventional gridding approach (termed here, GRD) to determine the spatial resolution of the resulting σ° images. The pixel mean, variance, and autocovariance are also compared for the GRD, AVE, and SIR methods. Reconstruction parameters for ASCAT are also considered, resulting in a choice of 30 iterations of SIR and a non-quantized SRF. The appropriate pixel size for the reconstructed σ° images is also considered.

The SRF is additionally required to determine the land contribution ratio (LCR) of a σ° measurement. The LCR for ASCAT is shown in Chapter 5, in addition to ultra-high resolution (UHR) ASCAT wind estimates. UHR wind is created from enhanced-resolution σ° images using a single pass of data. The LCR is used to enable near-coastal wind retrieval in UHR data. This is an improvement over a traditional distance-based threshold, which is overly restrictive and withholds more land-contaminated σ° measurements from wind retrieval than necessary. With the LCR of each measurement characterized, land contamination is addressed on a per-measurement basis instead of a strict distance-from-land measure. Additionally, a dynamic LCR threshold is created in order for the level of acceptable land contamination to be directly related to a maximum error level. The near-coastal UHR winds are compared against buoy-measured winds. This validates the LCR approach since no land contamination is apparent in the UHR data when using the LCR approach. Also, when compared to the buoy data, the UHR data is as good as—or slightly better than—the conventional resolution ASCAT wind product.

Two geoscience applications of enhanced-resolution σ° and wind data are explored in Chapter 6. The first uses both backscatter and wind data to map the surface extent of the 2010 Deepwater Horizon oil spill. The oil spill was large enough to be resolvable by ASCAT; the impact of the oil is visible in the σ° measurements and by extension the retrieved wind speeds as well. Numerical weather predicted (NWP) winds are used as a comparison dataset to account for changes in σ° due to wind speeds. This increases the effectiveness of detecting surface oil. The results validate well against other sources, especially for the central body of oil. For smaller regions further from the source of the leak, the oil is not as detectable in ASCAT data. The second geoscience application in Chapter 6 is the mapping of the azimuth angle anisotropy in East Antarctica. This is performed for ASCAT data as well as for the QuikSCAT scatterometer. The ASCAT and QuikSCAT azimuth modulation parameters are largely similar yet have significant differences: the magnitude of the azimuth modulation is much larger for ASCAT (at C band) than for QuikSCAT (at Ku band). The azimuth modulation parameters are stable over time, suggesting that the differences between ASCAT and QuikSCAT are not transitory or a result of sampling differences, but are due to geophysical differences at the scale of the two wavelengths.

7.2 Contributions

The unique contributions of this dissertation are enumerated below:

ASCAT SRF The ASCAT measurement SRF is accurately characterized. The ASCAT SRF has not been previously described nor distributed in the open literature. This necessitates understanding the ASCAT design in order to identify and model the major components of the SRF. These include the antenna response, the onboard range-Doppler processing, and the along-track pulse averaging. Although I obtain the designed antenna response from EUMETSAT, the effect of the onboard processing is “reverse-engineered” based on the available documentation of how ASCAT operates.

In order to reduce the computational load of evaluating the full SRF for each measurement, I parameterize an approximation of the SRF. Although it is possible to opt for a simple approximation, such as modeling the SRF as the combination of two Gaussian functions, or only modeling a quantized SRF (such as the $-3\,\mathrm{dB}$ contour shape), I instead develop a more thorough parameterization that uses low-order polynomials to describe the SRF accurately down to $-10\,\mathrm{dB}$ from the peak. This is more accurate than required for image reconstruction using AVE and SIR, but it ensures an accurate estimation of the LCR value.

Both the reference and parameterized SRFs are validated. Some validation was performed in conjunction with EUMETSAT, but I validate the SRF estimate by comparing the predicted and actual σ° measurements using the estimated SRF, as well as against alternate SRF descriptions known to be less accurate.

Image reconstruction I apply the GRD, AVE, and SIR algorithms to ASCAT, including determining a suitable number of SIR iterations, selecting a reconstruction pixel size, and choosing between the full or quantized SRF. Although these algorithms are not novel to this dissertation, I perform a more comprehensive analysis and comparison than previously conducted.

The first- and second-order pixel statistics are derived for GRD and for AVE and validated through simulation. The pixel statistics for SIR are also computed through simulation and compared against the GRD and AVE values. This enables a more objective comparison of GRD, AVE, and SIR than previously performed. Further, the analysis pays special focus to AVE, which in previous work was neglected in favor of SIR. By comparing AVE and SIR directly, I am able to conclude, for example, that SIR has a small bias not present in AVE, but that SIR has a lower variance than AVE. Also, the correlation between an AVE or SIR pixel and its neighboring pixels is computed. This leads to the observation that AVE typically has a smaller correlation area than AVE, but its shape is more irregular than SIR.

Although difficult to precisely quantify the spatial resolution of GRD, AVE, and SIR, I use a simple spectral analysis for each case. This enables the observation that AVE and SIR have similar high-frequency content, but that SIR better recovers the high-frequency content that is attenuated in AVE. This appears to be a tradeoff with some additional high-frequency noise.

Near-coastal winds The idea of applying the LCR for land contamination mitigation is not unique to this dissertation as it has previously been used for QuikSCAT data. However, I modify and simplify the dynamic LCR thresholding approach and successfully apply it to ASCAT. Additionally, I set the LCR threshold to vary as a proportion of the ocean-only error.

Some buoy validation has previously been performed for QuikSCAT UHR winds and for conventional resolution ASCAT, but this dissertation is unique in using buoys to validate UHR ASCAT winds. The buoys are specially selected to evaluate whether land contamination is present or not in the UHR winds.

Oil spill mapping Oil spills have previously been mapped using SAR data, but to my knowledge, this dissertation is unique in using scatterometer data to map an oil spill. This is likely due to two factors: (1) the coarser spatial resolution of scatterometers compared to SAR limits the utility of scatterometers for typical oil spills; and (2) the Deepwater Horizon oil spill is atypical because it spanned a very large surface area for many days.

In addition, the impact of wind speed oil look-alikes is reduced by using numerical weather predicted (NWP) winds as part of the oil detection process rather than relying on a backscatter contrast alone. This approach also appears to be unique.

Azimuth modulation The azimuth angle modulation of σ° in East Antarctica has previously been described and measured using instruments such as ASCAT and QuikSCAT, but a direct comparison between the ASCAT and QuikSCAT data has not been described before.

I also weight the parameter estimation by the SRF values (similar to the AVE algorithm), which has not been performed previously.

7.3 Publications

The research described in this dissertation has either been published or is currently in review. An early description of the ASCAT SRF and the application of SIR to ASCAT data was presented at an IEEE conference [24]. This is superseded by the work described in Chapters 3 and 4; the material in Chapter 3 is in review for inclusion in *IEEE Transactions on Geoscience and Remote Sensing* [63], and the material in Chapter 4 has been peer reviewed and accepted for publication in *IEEE Transactions on Geoscience and Remote Sensing* [77]. The research in Section 6.1 for the Deepwater Horizon oil spill was presented at an IEEE conference [78] and published in *IEEE Transactions on Geoscience and Remote Sensing* after peer review [79]. The azimuth modulation research in Section 6.2 in currently in review for *IEEE Geoscience and Remote Sensing Letters* [80]. Finally, the material in Chapter 5 is currently in review for *IEEE Transactions on Geoscience and Remote Sensing* as part of a larger paper that analyzes and validates ASCAT UHR winds [81].

7.4 Future Research

Over the course of completing the research documented in this dissertation and elsewhere, I identify the following avenues of future research:

- The ASCAT SRF as described in Chapter 3 is sufficiently accurate for the applications in this dissertation, but increased accuracy may be desired in the future. One aspect of ASCAT that was not included, for example, is the filter used on the received signal. This does not appear to significantly affect the SRF, but it may be responsible for some small changes in the SRF. The SRF computation includes some approximations, such as assuming a spherical Earth at some stages. An ellipsoidal model is more appropriate yet more complicated to implement. Further approximations were made in order to avoid a computationally expensive orbit propagation step. These approximations would be unnecessary if the ASCAT orbit propagation were implemented.

- The SRF parameterization described in Chapter 3 is accurate, but the assumption that the SRF is elliptical is not valid for measurements at very low incidence angles ($< 25°$): at these angles, the SRF becomes more curved. This is not included in the parameterization due to both its complexity and that these measurements are typically discarded from processing. A future refinement to the parameterized SRF could include this curvature, or, instead, a more generalized parameterization could be developed.
- The reconstruction statistics are derived in Chapter 4 for GRD and for AVE, but no attempt is made to derive the statistics for SIR. This is due to the non-linear nature of SIR. The SIR non-linearity, however, could be approximated as linear (SIR uses a sigmoid function, so its behavior is indeed linear when close to the origin) and the first- and second-order statistics could be derived. If so, this obviates the need for simulation to compute the pixel statistics for SIR.
- Only a limited spectral analysis of GRD, AVE, and SIR is undertaken in Chapter 4. This could be extended and generalized.
- This dissertation focused on the GRD, AVE, and SIR algorithms. Other reconstruction algorithms could be evaluated and compared, such as the Backus-Gilbert [30] method, or the maximum *a posteriori* approach considered in [28] for QuikSCAT data (and which used the early, incorrect ASCAT SRF from [24]).
- The buoy validation in Chapter 5 uses only one year of collocations and only buoys in a small region. The number of collocations could be expanded by increasing the spatial region and extending the time period.
- For the oil spill mapping in Section 6.1, the early but incorrect SRF from [24] was used. Repeating the methodology with the more accurate SRF from Chapter 3 would therefore give somewhat different results, which perhaps may improve the oil spill detection. Additionally, there may be higher-resolution ECMWF winds than the 1°x1°

product used. In computing the backscatter error, the beams are equally weighted, but they measure σ° at different incidence angles. This could be accounted for by either using an unequal weighting of the three beams or the σ° values could be corrected after estimating $\mathcal{B}$, the incidence angle dependence of σ°. Additionally, the OSCAT scatterometer was operational during the time period of the Deepwater Horizon oil spill. Unlike ASCAT, it measures σ° at both horizontal and vertical polarization. Fusing the OSCAT data with ASCAT may improve the spill extent mapping.

- The azimuth modulation of East Antarctica in Section 6.2 is compared using ASCAT and QuikSCAT data. More microwave instruments could be used to map the azimuth modulation parameters, such as from radiometers, which measure the microwave brightness temperature at a variety of polarizations and frequencies. This may provide further insight into the geophysical parameters responsible for the observed azimuth angle anisotropy.

7.5 Final Remarks

The results and contributions of this dissertation are available not only here and in the publications listed above, but also in the form of processed data available as part of the NASA-sponsored Scatterometer Climate Record Pathfinder (SCP) at `http://scp.byu.edu`. Reconstructed σ° images from ASCAT measurements are produced using the GRD, AVE, and SIR methods discussed in this dissertation. It is anticipated that the enhanced-resolution data will benefit other geoscience studies and applications.

Bibliography

[1] T. A. Scambos, M. Frezzotti, T. Haran, J. Bohlander, J. T. M. Lenaerts, M. R. Van Den Broeke, K. Jezek, D. G. Long, S. Urbini, K. Farness, T. Neumann, M. Albert, and J. Winther, "Extent of low-accumulation 'wind glaze' areas on the East Antarctic plateau: implications for continental ice mass balance," *Journal of Glaciology*, vol. 58, no. 210, pp. 633–647, Aug 2012. xiv, 96, 97, 106, 107, 108

[2] J. Figa-Saldaña, J. J. W. Wilson, E. Attema, R. Gelsthorpe, M. R. Drinkwater, and A. Stoffelen, "The Advanced Scatterometer (ASCAT) on the meteorological operational (MetOp) platform: A follow on for European wind scatterometers," *Canadian Journal of Remote Sensing*, vol. 28, no. 3, pp. 404–412, 2002. 6, 10, 25, 63

[3] F. M. Naderi, M. H. Freilich, and D. G. Long, "Spaceborne radar measurement of wind velocity over the ocean-an overview of the NSCAT scatterometer system," *Proceedings of the IEEE*, vol. 79, no. 6, pp. 850–866, 1991. 6, 8, 9

[4] F. T. Ulaby and D. G. Long, *Microwave Radar and Radiometric Remote Sensing.* The University of Michigan Press, 2014. 7, 8, 9, 10

[5] I. S. Ashcraft and D. G. Long, "The spatial response function of SeaWinds backscatter measurements," in *Proceedings of SPIE: Earth Observing Systems VIII*, W.L. Barnes, Ed., vol. 5151, 3–6 Aug. 2003. 7, 8, 16, 44

[6] C. Nie, "Wind/rain backscatter modeling and wind/rain retrieval for scatterometer and synthetic aperture radar," Ph.D. dissertation, Brigham Young University, 2008. 9

[7] H. Hersbach, "Cmod5.n: A C-band geophysical model function for equivalent neutral wind," ECMWF, Tech. Rep., 2008. [Online]. Available: http://www.ecmwf.int/publications/library/ecpublications/_pdf/tm/501-600/tm554.pdf 9, 83

[8] A. Stoffelen, "Scatterometry," Ph.D. dissertation, Utrecht University, 1998. [Online]. Available: http://dspace.library.uu.nl/handle/1874/636 9

[9] S. J. Shaffer, R. S. Dunbar, S. V. Hsiao, and D. G. Long, "A median-filter-based ambiguity removal algorithm for NSCAT," *IEEE Transactions on Geoscience and Remote Sensing*, vol. 29, no. 1, pp. 167–174, 1991. 10

[10] A. Stoffelen, S. de Haan, Y. Quilfen, and H. Schyberg, "ERS scatterometer ambiguity removal scheme comparison," Royal Netherlands Meterological Institute, Tech. Rep., 2000. [Online]. Available: http://www.knmi.nl/publications/showAbstract.php?id=4835 10

[11] A. M. Swan and D. G. Long, “Multiyear arctic sea ice classification using QuikSCAT,” *IEEE Transactions on Geoscience and Remote Sensing*, vol. 50, no. 9, pp. 3317–3326, 2012. 10, 18

[12] L. Breivik, S. Eastwood, and T. Lavergne, “Use of C-band scatterometer for sea ice edge identification,” *IEEE Transactions on Geoscience and Remote Sensing*, vol. 50, no. 7, pp. 2669–2677, 2012. 10

[13] K. M. Stuart and D. G. Long, “Tracking large tabular icebergs using the SeaWinds Ku-band microwave scatterometer,” *Deep Sea Research Part II: Topical Studies in Oceanography*, vol. 58, no. 11–12, pp. 1285–1300, 2011. 10, 18

[14] ——, “Iceberg size and orientation estimation using SeaWinds,” *Cold Regions Science and Technology*, vol. 69, no. 1, pp. 39–51, 2011. 10, 18

[15] W. Wagner, S. Hahn, R. Kidd, T. Melzer, Z. Bartalis, S. Hasenauer, J. Figa-Saldaña, P. de Rosnay, A. Jann, S. Schneider, J. Komma, G. Kubu, K. Brugger, C. Aubrecht, J. Züger, U. Gangkofner, S. Kienberger, L. Brocca, Y. Wang, G. Blöschl, J. Eitzinger, K. Steinnocher, P. Zeil, and F. Rubel, “The ASCAT soil moisture product: A review of its specifications, validation results, and emerging applications,” *Meteorologische Zeitschrift*, vol. 22, no. 1, pp. 5–33, 2013. 10

[16] D. G. Long and P. J. Hardin, “Vegetation studies of the Amazon basin using enhanced resolution Seasat scatterometer data,” *IEEE Transactions on Geoscience and Remote Sensing*, vol. 32, no. 2, pp. 449–460, 1994. 10

[17] D. W. Draper and D. G. Long, “Simultaneous wind and rain retrieval using SeaWinds data,” *IEEE Transactions on Geoscience and Remote Sensing*, vol. 42, no. 7, pp. 1411–1423, 2004. 10, 18

[18] M. P. Owen and D. G. Long, “M-ary Bayes estimator selection for QuikSCAT simultaneous wind and rain retrieval,” *IEEE Transactions on Geoscience and Remote Sensing*, vol. 49, no. 11, pp. 4431–4444, 2011. 10

[19] A. D. Fraser, N. W. Young, and N. Adams, “Comparison of microwave backscatter anisotropy parameterizations of the Antarctic ice sheet using ASCAT,” *IEEE Transactions on Geoscience and Remote Sensing*, vol. 52, no. 3, pp. 1583–1595, 2014. 10, 96

[20] D. G. Long and M. R. Drinkwater, “Azimuth variation in microwave scatterometer and radiometer data over Antarctica,” *IEEE Transactions on Geoscience and Remote Sensing*, vol. 38, no. 4, pp. 1857–1870, Jul 2000. 10, 96, 98

[21] I. S. Ashcraft and D. G. Long, “Relating microwave backscatter azimuth modulation to surface properties of the Greenland ice sheet,” *Journal of Glaciology*, vol. 52, no. 177, p. 257–266, Mar 2006. [Online]. Available: http://dx.doi.org/10.3189/172756506781828764 10, 96

[22] I. J. Birrer, E. M. Bracalente, G. J. Dome, J. Sweet, and G. Berthold, "$\sigma°$ signature of the Amazon rain forest obtained from the Seasat scatterometer," *IEEE Transactions on Geoscience and Remote Sensing*, vol. GE-20, no. 1, pp. 11–17, Jan. 1982. 12

[23] D. G. Long, M. R. Drinkwater, B. Holt, S. Saatchi, and C. Bertoia, "Global ice and land climate studies using scatterometer image data," *EOS Transactions, American Geophysical Union*, vol. 82, no. 43, p. 503, 2001. 12, 16

[24] R. D. Lindsley and D. G. Long, "Adapting the SIR algorithm to ASCAT," in *Geoscience and Remote Sensing Symposium (IGARSS), 2010 IEEE International*, 2010, pp. 3402–3405. 12, 37, 86, 114, 115

[25] D. G. Long, P. Hardin, and P. Whiting, "Resolution enhancement of spaceborne scatterometer data," *IEEE Transactions on Geoscience and Remote Sensing*, vol. 31, no. 3, pp. 700–715, 1993. 12, 16, 18

[26] *Estimation of ASCAT-Normalised Radar Cross Section: ATBD*, EUMETSAT, July 2014, EUMETSAT reference EUM/TSS/SPE/14/762689, available from `ops@eumetsat.int`. 13, 25, 43

[27] P. K. Yoho and D. G. Long, "An improved simulation model for spaceborne scatterometer measurements," *IEEE Transactions on Geoscience and Remote Sensing*, vol. 41, no. 11, pp. 2692–2695, 2003. 14

[28] B. A. Williams and D. G. Long, "Reconstruction from aperture-filtered samples with application to scatterometer image reconstruction," *IEEE Transactions on Geoscience and Remote Sensing*, vol. 49, no. 5, pp. 1663–1676, May 2011. 15, 16, 115

[29] D. S. Early and D. G. Long, "Image reconstruction and enhanced resolution imaging from irregular samples," *IEEE Transactions on Geoscience and Remote Sensing*, vol. 39, no. 2, pp. 291–302, 2001. 16, 17, 18, 40, 45, 127, 129, 130

[30] G. E. Backus and J. F. Gilbert, "Numerical applications of a formalism for geophysical inverse problems," *Geophysical Journal International*, vol. 13, no. 1-3, pp. 247–276, July 1967. 16, 115

[31] D. G. Long and D. L. Daum, "Spatial resolution enhancement of SSM/I data," *IEEE Transactions on Geoscience and Remote Sensing*, vol. 36, no. 2, pp. 407–417, 1998. 16

[32] F. Lenti, F. Nunziata, C. Estatico, and M. Migliaccio, "On the spatial resolution enhancement of microwave radiometer data in Banach spaces," *IEEE Transactions on Geoscience and Remote Sensing*, vol. 52, no. 3, pp. 1834–1842, 2014. 16

[33] J. P. Bradley and D. G. Long, "Estimation of the OSCAT spatial response function using island targets," *IEEE Transactions on Geoscience and Remote Sensing*, vol. 52, no. 4, pp. 1924–1934, 2014. 16

[34] D. G. Long, "NSCAT views land and ice," in *Geoscience and Remote Sensing Symposium Proceedings, 1998. IGARSS '98. 1998 IEEE International*, vol. 4, 1998, pp. 1973–1975. 16

[35] R. D. Lindsley and D. G. Long, "Standard BYU ASCAT land/ice image products," BYU MERS Lab, Tech. Rep., 2010. [Online]. Available: http://www.mers.byu.edu/docs/reports/MERS1002.pdf 16

[36] B. A. Williams, M. P. Owen, and D. G. Long, "The ultra high resolution QuikSCAT product," in *Radar Conference, 2009 IEEE*, May 2009, pp. 1–6. 18

[37] D. G. Long and J. B. Luke, "High-resolution wind retrieval for SeaWinds," R. J. Frouin, G. D. Gilbert, and D. Pan, Eds., vol. 5155, no. 1. SPIE, 2003, pp. 216–225. 18, 96, 103, 127

[38] M. P. Owen and D. G. Long, "Simultaneous wind and rain estimation for QuikSCAT at ultra-high resolution," *IEEE Transactions on Geoscience and Remote Sensing*, 2011, to appear. 18

[39] F. Saïd and D. G. Long, "Determining selected tropical cyclone characteristics using QuikSCAT's ultra-high resolution images," *IEEE Journal of Selected Topics on Applied Observations and Remote Sensing*, vol. 4, no. 4, pp. 857–869, 2011. 18

[40] Q. P. Remund and D. G. Long, "A decade of QuikSCAT scatterometer sea ice extent data," *IEEE Transactions on Geoscience and Remote Sensing*, vol. 52, no. 7, pp. 4281–4290, 2014. 18

[41] L. B. Kunz and D. G. Long, "Melt detection in Antarctic ice shelves using scatterometers and microwave radiometers," *IEEE Transactions on Geoscience and Remote Sensing*, vol. 44, no. 9, pp. 2461–2469, 2006. 18

[42] B. R. Hicks and D. G. Long, "Inferring Greenland melt and refreeze severity from seawinds scatterometer data," *International Journal of Remote Sensing*, vol. 32, no. 23, pp. 8053–8080, Aug 2011. 18

[43] S. Frolking, M. Fahnestock, T. Milliman, K. McDonald, and J. Kimball, "Interannual variability in North American grassland biomass/productivity detected by SeaWinds scatterometer backscatter," *Geophysical Research Letters*, vol. 32, no. 21, 2005. 18

[44] S. R. Oza, S. Panigrahy, and J. S. Parihar, "Concurrent use of active and passive microwave remote sensing data for monitoring of rice crop," *International Journal of Applied Earth Observation and Geoinformation*, vol. 10, no. 3, pp. 296–304, 2008. 18

[45] P. J. Hardin and D. G. Long, "Integrating reconstructed scatterometer and advanced very high resolution radiometer data for tropical forest inventory," *Opt. Eng*, vol. 34, no. 11, pp. 3146–3153, Nov 1995. 18

[46] M. P. Owen and D. G. Long, "Land-contamination compensation for QuikSCAT near-coastal wind retrieval," *IEEE Transactions on Geoscience and Remote Sensing*, vol. 47, no. 3, pp. 839–850, 2009. 19, 20, 64, 67, 69, 70

[47] W. J. Hullinger and D. G. Long, "Mitigation of sea ice contamination in QuikSCAT wind retrieval," *IEEE Transactions on Geoscience and Remote Sensing*, vol. 52, no. 4, pp. 2149–2158, 2014. 20

[48] P. Clemente-Colón and X. H. Yan, "Low-backscatter ocean features in synthetic aperture radar imagery," *Johns Hopkins APL Technical Digest*, vol. 21, no. 1, pp. 116–121, 2000. [Online]. Available: http://www.jhuapl.edu/techdigest/TD/td2101/clemente.pdf 20

[49] W. Alpers, "Remote sensing of oil spills," in *Maritime Disaster Management Symposium*, 2002, pp. 19–23. 20, 21

[50] C. Brekke and A. H. S. Solberg, "Oil spill detection by satellite remote sensing," *Remote Sensing of Environment*, vol. 95, no. 1, pp. 1–13, 2005. 20, 21, 81

[51] M. Migliaccio, F. Nunziata, A. Montuori, X. Li, and W. G. Pichel, "A multifrequency polarimetric SAR processing chain to observe oil fields in the Gulf of Mexico," *IEEE Transactions on Geoscience and Remote Sensing*, no. 99, pp. 1–9, 2011, Early Access. 20, 81

[52] M. Migliaccio, A. Gambardella, and M. Tranfaglia, "SAR polarimetry to observe oil spills," *IEEE Transactions on Geoscience and Remote Sensing*, vol. 45, no. 2, pp. 506–511, 2007. 20, 81

[53] A. H. S. Solberg, C. Brekke, and P. O. Husoy, "Oil spill detection in Radarsat and Envisat SAR images," *IEEE Transactions on Geoscience and Remote Sensing*, vol. 45, no. 3, pp. 746–755, 2007. 20, 81

[54] B. Zhang, W. Perrie, X. Li, and W. G. Pichel, "Mapping sea surface oil slicks using RADARSAT-2 quad-polarization SAR image," *Geophysical Research Letters*, vol. 38, no. L10602, 2011. 20

[55] M. A. Donelan and W. J. Pierson Jr, "Radar scattering and equilibrium ranges in wind-generated waves with application to scatterometry," *Journal of Geophysical Research*, vol. 92, no. C5, pp. 4971–5029, 1987. 21

[56] F. Girard-Ardhuin, G. Mercier, F. Collard, and R. Garello, "Operational oil-slick characterization by SAR imagery and synergistic data," *IEEE Journal of Oceanic Engineering*, vol. 30, no. 3, p. 487, 2005. 21

[57] C. Nie and D. G. Long, "A C-Band scatterometer simultaneous wind/rain retrieval method," *IEEE Transactions on Geoscience and Remote Sensing*, vol. 46, no. 11, pp. 3618–3631, 2008. 21

[58] M. P. Owen and D. G. Long, “Towards an improved wind and rain backscatter model for ASCAT,” in *Geoscience and Remote Sensing Symposium (IGARSS), 2010 IEEE International*, July 2010, pp. 2531–2534. 21

[59] I. S. Ashcraft, “Projecting an arbitrary latitude and longitude onto a tangent plane,” BYU MERS Lab, Tech. Rep. 99-04, 1999. [Online]. Available: http://www.mers.byu.edu/docs/reports/MERS9904.pdf 23, 65

[60] R. D. Lindsley, “Estimating the ASCAT spatial response function,” BYU MERS Lab, Tech. Rep. 14-01, May 2014. [Online]. Available: http://www.mers.byu.edu/docs/reports/MERS1401.pdf 24, 28

[61] C. Anderson, H. Bonekamp, C. Duff, J. Figa-Saldaña, and J. J. W. Wilson, “Analysis of ASCAT ocean backscatter measurement noise,” *IEEE Transactions on Geoscience and Remote Sensing*, vol. 50, no. 7, pp. 2449–2457, July 2012. 25, 28

[62] J. J. W. Wilson, C. Anderson, M. A. Baker, H. Bonekamp, J. Figa-Saldaña, R. G. Dyer, J. A. Lerch, G. Kayal, R. V. Gelsthorpe, M. A. Brown, E. Schied, S. Schutz-Munz, F. Rostan, E. W. Pritchard, N. G. Wright, D. King, and Ü. Önel, “Radiometric calibration of the advanced wind scatterometer radar ASCAT carried onboard the METOP-A satellite,” *IEEE Transactions on Geoscience and Remote Sensing*, vol. 48, no. 8, pp. 3236–3255, Aug 2010. 28

[63] R. D. Lindsley, C. Anderson, J. Figa-Saldaña, and D. G. Long, “A parameterized ASCAT measurement spatial response function,” *IEEE Transactions on Geoscience and Remote Sensing*, 2015, in review. 36, 37, 114

[64] K. Gröchenig, “Reconstruction algorithms in irregular sampling,” *Mathematics of Computation*, vol. 59, no. 199, pp. 181–194, July 1992. 40, 41, 127

[65] A. Verhoef, M. Portabella, and A. Stoffelen, “High-resolution ASCAT scatterometer winds near the coast,” *IEEE Transactions on Geoscience and Remote Sensing*, vol. 50, no. 7, pp. 2481–2487, Jul 2012. 63

[66] J. R. Blodgett, “Analysis, validation, and improvement of high-resolution wind estimates from the advanced scatterometer (ASCAT),” Master’s thesis, Brigham Young University, December 2014. [Online]. Available: http://www.mers.byu.edu/long/theses/msthesis_blodgett.pdf 63

[67] B. A. Williams and D. G. Long, “Estimation of hurricane winds from SeaWinds at ultrahigh resolution,” *IEEE Transactions on Geoscience and Remote Sensing*, vol. 46, no. 10, pp. 2924–2935, 2008. 63

[68] F. Saïd and D. G. Long, “Effectiveness of QuikSCAT’s ultra-high resolution images in determining tropical cyclone eye location,” in *IEEE International Geoscience and Remote Sensing Symposium, 2008. IGARSS 2008.*, vol. 1, July 2008, pp. I–351–I–354. 63

[69] W. T. Liu, K. B. Katsaros, and J. A. Businger, “Bulk parameterization of air-sea exchanges of heat and water vapor including the molecular constraints at the interface,” *Journal of the Atmospheric Sciences*, vol. 36, no. 9, pp. 1722–1735, Sep 1979. 71

[70] A. B. Kara, A. J. Wallcraft, and M. A. Bourassa, “Air-sea stability effects on the 10 m winds over the global ocean: Evaluations of air-sea flux algorithms,” *Journal of Geophysical Research*, vol. 113, no. C4, 2008. 71

[71] A. Verhoef and A. Stoffelen, “Validation of ASCAT 12.5-km winds,” KNMI, Tech. Rep., February 2009, sAF/OSI/CDOP/KNMI/TEC/RP/147. [Online]. Available: ftp://podaac.jpl.nasa.gov/allData/ascat/preview/L2/docs/ASCAT_validation_125.pdf 75

[72] T. J. Crone and M. Tolstoy, “Magnitude of the 2010 Gulf of Mexico oil leak,” *Science*, vol. 330, no. 6004, p. 634, 2010. 81

[73] Satellite Derived Surface Oil Analysis Products - Deepwater Horizon. NOAA/NESDIS. [Online]. Available: http://www.ssd.noaa.gov/PS/MPS/deepwater.html 84

[74] B. Lambert and D. G. Long, “Seasonal and interannual variations in Antarctic backscatter signature from 2000 to 2006 as observed by QuikSCAT,” *Earth Observing Systems XII*, Sep 2007. 96

[75] Z. Bartalis, K. Scipal, and W. Wagner, “Azimuthal anisotropy of scatterometer measurements over land,” *IEEE Transactions on Geoscience and Remote Sensing*, vol. 44, no. 8, pp. 2083–2092, 2006. 96

[76] M. W. Spencer, C. Wu, and D. G. Long, “Improved resolution backscatter measurements with the SeaWinds pencil-beam scatterometer,” *IEEE Transactions on Geoscience and Remote Sensing*, vol. 38, no. 1, pp. 89–104, 2000. 97

[77] R. D. Lindsley and D. G. Long, “Enhanced-resolution reconstruction of ASCAT backscatter measurements,” *IEEE Transactions on Geoscience and Remote Sensing*, 2016, to appear. 114

[78] ——, “Estimating surface oil extent from the Deepwater Horizon oil spill using ASCAT backscatter,” in *Radar Conference (RADAR), 2011 IEEE*, 2011, pp. 559–563. 114

[79] ——, “Mapping surface oil extent from the Deepwater Horizon oil spill using ASCAT backscatter,” *IEEE Transactions on Geoscience and Remote Sensing*, vol. 50, no. 7, pp. 2534–2541, 2012. 114

[80] ——, “ASCAT and QuikSCAT azimuth modulation of backscatter over East Antarctica,” *IEEE Geoscience and Remote Sensing Letters*, 2016, in review. 114

[81] R. D. Lindsley, J. R. Blodgett, and D. G. Long, “Analysis and validation of high-resolution wind from ASCAT,” *IEEE Transactions on Geoscience and Remote Sensing*, 2016, in review. 114

[82] A. V. Oppenheim, R. W. Schafer, and J. R. Buck, *Discrete-Time Signal Processing*, 2nd ed., A. V. Oppenheim, Ed. Prentice Hall, 1998. 126, 132

[83] B. A. Williams, “Signal processing methods for ultra high resolution scatterometry,” Ph.D. dissertation, Brigham Young University, 2010. 128

[84] J. J. W. Wilson, “ASCAT inverse impulse response function,” Personal communication (email), Jan 2009. 135

[85] *ASCAT Product Generation Function Specification*, 2005. [Online]. Available: http://eumeds.eumetsat.int/groups/ops/documents/document/PDF_TEN_990009-EPS-ASCAT-PGS.pdf 135

Appendix A

Background in Sampling and Reconstruction

In this appendix, some background in sampling theory is discussed, along with the extensions required to discuss the special class of sampling employed by ASCAT: irregularly spaced aperture-filtered sampling. Further information about the block additive algebraic reconstruction technique (AART) is also given.

A.1 Sampling Theory for Scatterometers

Sampling theory dictates that, under certain conditions, a signal may be sampled such that its samples perfectly represent the signal. The classical case of a band-limited regularly sampled signal is governed by the Nyquist criterion—there is a relationship between the minimum sampling frequency and the signal bandwidth that, if satisfied, perfectly represent the signal.

The regular assumptions of this classical case are too restrictive for some classes of signals, including scatterometer measurements of the Earth surface σ°, as considered in this dissertation. These signals are sampled at irregular locations using aperture functions. Some background on sampling theory is presented in this section. Conventional sampling is reviewed first, followed by extensions to model both irregularly spaced samples and aperture-filtered samples.

A.1.1 Regular Sampling and Reconstruction

For a regularly (meaning periodically) sampled band-limited signal with bandwidth ω_0, the Nyquist criterion gives the minimum sampling frequency (f_s), or equivalently, the maximum sampling period (T_s), in order to perfectly reconstruct the signal:

$$T_s < \frac{1}{\omega_0} \tag{A.1}$$

$$f_s > \omega_0. \tag{A.2}$$

Here, the signal bandwidth extends from $-\omega_0/2$ to $\omega_0/2$, for a total bandwidth of ω_0.

The signal of interest is $a(x)$, a one-dimensional continuous signal with bandwidth ω_0. To obtain a single sample from the signal, the sifting property selects a value from $a(x)$ at location x_0:

$$a(x_0) = \int a(x)\delta(x - x_0)\, dx. \tag{A.3}$$

Interpreted another way, a sample of $a(x)$ is the inner product between the signal and a sampling function: $a(x_0) = \langle a(x), \delta(x - x_0) \rangle$.

Regularly sampling the function $a(x)$ is represented with an impulse train (also known as a Dirac comb or Shah function):

$$Ш_T(x) = \sum_{m=-\infty}^{\infty} \delta(x - mT), \tag{A.4}$$

where T is the sampling period, or interval between successive delta functions. The sampled signal is

$$\begin{align} a_s(x) &= a(x) Ш_T(x) \tag{A.5} \\ &= a(x) \sum_{n=-\infty}^{\infty} \delta(x - nT) \tag{A.6} \\ &= \sum_{n=-\infty}^{\infty} a(nT) \delta(x - nT). \tag{A.7} \end{align}$$

The sampled function $a_s(x)$ is still a continuous signal, but it is only defined at locations where $x = mT$ (m is an integer). The discrete-time function $a[n]$ is related to the sampled signal $a_s(x)$ through

$$a[n] = a_s(nT), \tag{A.8}$$

where n indexes the samples.

The signal $a(x)$ may be reconstructed from the samples $a[n]$ through sinc interpolation [82]:

$$\hat{a}(x) = \sum_{n=-\infty}^{\infty} a[n] \operatorname{sinc}\left(\frac{x - nT}{T} \right), \tag{A.9}$$

where the (normalized) sinc function is defined as

$$\operatorname{sinc}(x) = \frac{\sin \pi x}{\pi x}. \tag{A.10}$$

Because of the bandlimited nature of $a(x)$ and that it is sampled frequently enough to fulfill the Nyquist criterion, the reconstructed signal $\hat{a}(x)$ is identical to $a(x)$.

A.1.2 Irregular Sampling

In reality, not all signals are regularly sampled. For a collection of samples $\{s_i\}$ of $a(x)$ at arbitrary positions $\{x_i\}$, each sample may be expressed as

$$\begin{align} s_i &= \int a(x) \delta(x - x_i) \, dx \tag{A.11} \\ &= a(x_i), \tag{A.12} \end{align}$$

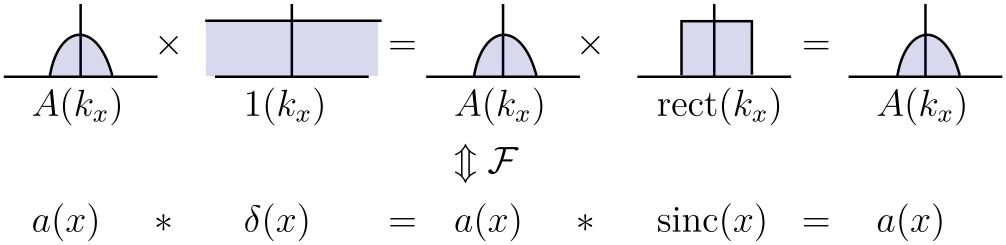

Figure A.1: This diagram illustrates how a band-limited $a(x)$, convolved with a delta function, is equivalent to convolution with a sinc function of appropriate bandwidth, which is in turn equivalent to itself.

where i is the sample index and x_i represents the position of sample i. The samples are characterized as having a density of δ, where δ represents the largest spacing between the samples.

Analogous to the Nyquist criterion, Gröchenig has shown [29, 37, 64] that irregularly sampled band-limited signals at a density of δ and a bandwidth of ω_0 can perfectly represent the original signal. This is termed here Gröchenig's lemma. The irregular samples represent the original signal if the collection of δ-dense samples satisfy

$$\delta < \frac{\ln(2)}{\omega_0}. \tag{A.13}$$

This is similar to the Nyquist criterion in Eq. (A.1), in that the sample period (parameterized here by δ) is related to the signal bandwidth. Note the additional factor of $\ln(2) \approx 0.69$.

A.1.3 Aperture-Filtered Irregular Sampling

The delta functions in Eq. (A.11) may be replaced with arbitrary functions, or apertures:

$$s_i = \int a(x) h_i(x)\, dx, \tag{A.14}$$

where each sample s_i has an associated aperture $h_i(x)$. This reduces to Eq. (A.11) if $h_i(x) = \delta(x - x_i)$. Note that if $a(x)$ is bandlimited, the delta functions in Eq. (A.11) can be replaced with sinc functions. An informal proof follows.

Figure A.1 illustrates the idea that convolving a band-limited function with a delta function is equivalent to convolution with a sinc function (with matching or greater bandwidth). Stated another way, a band-limited delta function is a sinc function.

To show how this applies to Eq. (A.11), the delta function is replaced by a generic aperture function $h_i(x)$:

$$s_i = \int a(x) h_i(x)\, dx = \langle a(x), h_i(x) \rangle. \tag{A.15}$$

While this is expressed as an inner product, it is also in the form of a convolution integral, evaluated at a single point (e.g. $\tau = 0$):

$$\int a(x)h_i(x)\,dx = \langle a(x), h_i(x)\rangle \tag{A.16}$$

$$\int a(x)g_i(\tau - x)\,dx = a(x) * g_i(x), \tag{A.17}$$

where the convolution kernel $g_i(x)$ is a reversed and possibly shifted aperture function $h_i(x)$: $g_i(x) = h_i(\alpha - x)$.

Substituting $h_i(x) = \delta(x - x_i)$ into $g_i(x)$:

$$\begin{aligned} g_i(x) &= h_i(\alpha - x) && \text{(A.18)}\\ &= \delta(\alpha - (x - x_i)) && \text{(A.19)}\\ &= \delta(\alpha + x_i - x). && \text{(A.20)} \end{aligned}$$

Noting that $\delta(-x) = \delta(x)$ and letting $\beta = \alpha + x_i$,

$$\begin{aligned} g_i(x) &= \delta(\beta - x) && \text{(A.21)}\\ &= \delta(x - \beta); && \text{(A.22)} \end{aligned}$$

therefore, $g_i(x)$, like $h_i(x)$, is a shifted delta function. The exact value of β is inconsequential since a nonzero β adds a phase shift to the Fourier transform while leaving the magnitude unaffected. Since $g_i(x)$ is a delta function, both $g_i(x)$ and $h_i(x)$ can be replaced with sinc functions, as discussed. Thus, because the signal has finite bandwidth, the delta functions in Eq. (A.11) can be replaced with sinc functions with appropriate bandwidth.

A.1.4 Two-Dimensional Signals

The previous subsections have used a one-dimensional signal $a(x)$ for clarity. However, the results are readily extended to a two-dimensional signal $a(x, y)$. Aperture-filtered irregular sampling, for example, is expressed as

$$s_i = \iint a(x, y)h_i(x, y)\,dx\,dy. \tag{A.23}$$

A.1.5 Discrete Signals

While the signal $a(x, y)$ is desired from reconstructing the measurements s_i, in practice we are only concerned with reconstructing $a[x_k, y_k]$, that is, $a(x, y)$ on a regular grid. A digital representation (e.g., an image) of $a(x, y)$ is stored and displayed as $a[x_k, y_k]$. So long as the grid spacing in $a[x_k, y_k]$ satisfies the Nyquist criterion, then $a(x, y)$ is completely represented by its discrete version. As before, sinc interpolation can reconstruct $a(x, y)$ from $a[x_k, y_k]$.

It has been shown [83] that if either the signal $a(x, y)$ or the aperture functions $h_i(x, y)$ are bandlimited, then the continuous functions are equivalent to discrete versions:

$$s_i = \iint a(x, y)h_i(x, y)\,dx\,dy = \sum_k a[x_k, y_k]h_i[x_k, y_k], \tag{A.24}$$

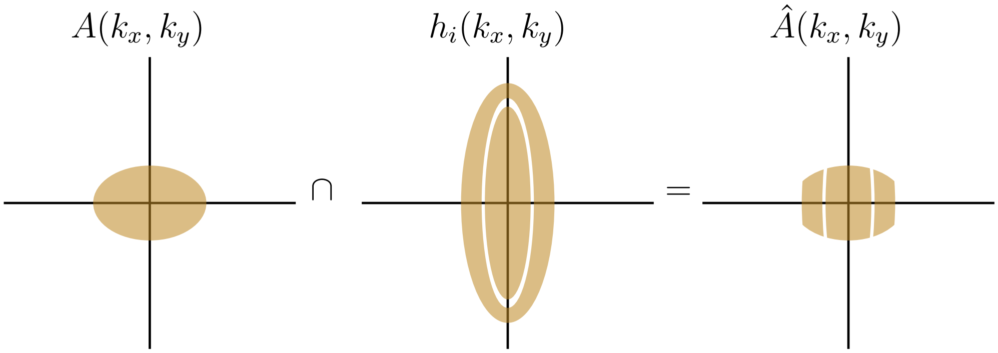

Figure A.2: Hypothetical region of support in the frequency domain for the signal $a(x, y)$, an aperture function $h_i(x, y)$, and the recoverable signal $\hat{a}(x, y)$. The recoverable frequencies are dictated by the intersection of frequency support.

where the discrete functions $a[x_k, y_k]$ and $h_i[x_k, y_k]$ are bandlimited to the smaller of the two bandwidths.

A.1.6 Signal Bandlimit

A bandlimited signal implies that the signal has infinite extent in the time or spatial domain. However, the functions $a[x_k, y_k]$ and $h_i[x_k, y_k]$ have a finite extent in the spatial domain, so they cannot be bandlimited. Nevertheless, these functions are treated as *approximately* bandlimited. For example, $a(x, y)$ is a signal generated from a physical process, such as radar reflectivity or brightness temperature. These signals typically have a power-law relationship that results in a red spectrum—that is, it decays as a function of frequency. Thus, at high enough frequencies, the energy is small. What a suitable cutoff frequency is depends on both the signal and how much aliasing is tolerable.

Even though high-frequency energy exists and is aliased after sampling, sampling with the bandlimited aperture functions $h_i[x_k, y_k]$ in Eq. (A.24) (usually lowpass in behavior) further suppresses the high-frequency energy so that the aliased energy can be ignored. This acts as a lowpass filter so that $a[x_k, y_k]$ is a bandlimited version of $a(x, y)$.

A.1.7 Aperture Bandlimit

While the signal may have bandlimit $\omega_{0,a}$, the aperture functions have their own bandlimits ω_{0,h_i}. Consider Fig. A.2 for a hypothetical bandlimit for signal $a(x, y)$ and aperture function $h_i(x, y)$. The recoverable bandwidth is governed by the *intersection* of the frequency support for the signal and for the aperture functions. Spectral nulls also reduce the recoverable frequencies. In Fig. A.2, the aperture function limits the recoverable frequencies in the k_x direction and also causes loss of frequencies due to spectral nulls. Using multiple variable aperture functions yields an effective net aperture function, with spectral nulls equal to the intersection of the spectral nulls of the component aperture functions (or, the union of the frequency extent of all the aperture function) [29].

"Aliasing" occurs if the original signal $a(x, y)$ has frequencies outside the limit given by Eq. (A.13). Technically, it is a generalized form of aliasing due to varying aperture functions and irregular sampling. This gives an interesting result, as demonstrated in Fig. A.2. Since the maximum frequency extent in the k_x direction is smaller for the recoverable signal than the actual signal, it is possible to have a more sparse δ-density (and therefore a larger T_s) than that required for the original signal, even though no aliasing is introduced. An alternate interpretation is that the aperture functions performs a role similar to an anti-aliasing filter.

A.2 Block AART

An iterative reconstruction approach is block additive ART [29]. This is expressed as

$$a_j^{(n+1)} = a_j^{(n)} + \frac{\sum_i (z_i - p_i) h_{ij}}{\sum_i h_{ij}}, \tag{A.25}$$

where $a^{(n)}$ is the n-th iteration of the a estimate and $p_i^{(n)}$ is the forward projection

$$p_i^{(n)} = \sum_j a_j^{(n)} h_{ij}, \tag{A.26}$$

z_i is noisy measurement i, and h_{ij} is the SRF value of measurement i at pixel j. Block AART may also be expressed in matrix equations, where the forward projection for iteration n is

$$\vec{p}_n = H \vec{a}_n \tag{A.27}$$

and block AART at iteration $n+1$ is

$$\vec{a}_{n+1} = \vec{a}_n + \tilde{H}^T (\vec{s} - \vec{p}_n), \tag{A.28}$$

where $\tilde{H}$ is column-normalized H (elements $h_{ij} / \sum_k h_{ik}$). Factoring out H (noting the implicit assumption that the estimate of H exactly matches the underlying H used for the aperture-filtered sampling operation):

$$\vec{a}_{n+1} = \vec{a}_n + \tilde{H}^T H (\vec{a} - \vec{a_n}). \tag{A.29}$$

$\tilde{H}^T H$ is $n \times n$, and $\vec{a}_{n+1}$ ideally converges to $\vec{a}$. Expressed another way,

$$\begin{aligned} \vec{a}_{n+1} &= \vec{a}_n + \tilde{H}^T (\vec{s} - \vec{p}_n) &\text{(A.30)} \\ &= \vec{a}_n + \tilde{H}^T \vec{s} - \tilde{H}^T H \vec{a}_n &\text{(A.31)} \\ &= (I - \tilde{H}^T H)\, \vec{a}_n + \tilde{H}^T \vec{s}. &\text{(A.32)} \end{aligned}$$

If $\tilde{H}^T = H^{-1}$, this reduces to Eq. (2.23).

A closed form solution of Eq. (A.32) for iteration N is, using the substitution $G = (I - \tilde{H}^T H)$ for brevity,

$$\begin{aligned} \vec{a}_N &= (G^{N-1} + G^{N-2} + \cdots + G^2 + G + I)\, \tilde{H}^T \vec{s} &\text{(A.33)} \\ &= \left(\sum_{n=0}^{N-1} G^n \right) \tilde{H}^T \vec{s} = \left(\sum_{n=0}^{N-1} (I - \tilde{H}^T H)^n \right) \tilde{H}^T \vec{s}. &\text{(A.34)} \end{aligned}$$

The term $\tilde{H}^T\vec{s}$[1] can be viewed as a first-order approximation to $\vec{a} = H^{-1}\vec{s}$. The power series $\sum_{n=0}^{N-1}(I - \tilde{H}^T H)^n$ is a correction factor.

For practical purposes, only a finite number of iterations may be computed. The error from using a finite number of terms in the power series is

$$\vec{a}_\infty - \vec{a}_N = \left(\sum_{n=0}^{\infty} G^n\right)\tilde{H}^T\vec{s} - \left(\sum_{n=0}^{N-1} G^n\right)\tilde{H}^T\vec{s} \tag{A.35}$$

$$= \left(\sum_{n=N}^{\infty} G^n\right)\tilde{H}^T\vec{s} = \left(\sum_{n=N}^{\infty}(I - \tilde{H}^T H)^n\right)\tilde{H}^T\vec{s}. \tag{A.36}$$

Note that while the power series depends only on the sampling matrix H, the iteration output in Eq. (A.34) and the truncated iteration error in Eq. (A.36) additionally depend on the measurements $\vec{s}$ and therefore the signal $a(x, y)$.

---

[1] Note that this is the definition of the AVE algorithm.

Appendix B

ASCAT FFT Bin Response

As part of its onboard processing, ASCAT estimates a power spectrum using an FFT (fast Fourier transform). The FFT, being an efficient implementation of the DFT (discrete Fourier transform), regularly samples the DTFT (discrete-time Fourier transform). The number of FFT bins is the number of samples from the DTFT. Window functions are often applied to data processed with an FFT in order to reduce spectral leakage.

This appendix derives the frequency response of each FFT bin used in the ASCAT power spectrum estimation. The frequency response of an unwindowed FFT bin is computed in Appendix B.1. The window function used onboard ASCAT is described in Appendix B.2, and the corresponding windowed FFT bin response is found in Appendix B.3.

B.1 Rect Window Response

For the discrete-time signal [82] $x[n]$ with length N (and assumed to be periodic with period N), the DTFT is expressed as

$$X(e^{j\omega}) = \sum_{n=0}^{N-1} x[n]e^{-j\omega n}. \tag{B.1}$$

The DFT is

$$\begin{aligned} X[k] &= \sum_{n=0}^{N-1} x[n]e^{-j2\pi kn/N} && \text{(B.2)} \\ &= X(e^{j\omega})|_{\omega=2\pi k/N}. && \text{(B.3)} \end{aligned}$$

Implicit in these definitions is a window function, $w[n]$, so that $x[n]$ should be replaced with $x[n]\, w[n]$. Instead, let $y[n] = x[n]\, w[n]$ so that $x[n]$ is the true signal, $w[n]$ is the window function, and $y[n]$ the windowed signal. Due to the convolution theorem,

$$Y(e^{j\omega}) = \text{DTFT}\{x[n]\, w[n]\} = X(e^{j\omega}) * W(e^{j\omega}). \tag{B.4}$$

To find the frequency response of an FFT bin means to determine which frequencies of $X(e^{j\omega})$ are in bin k of $Y[k]$. This depends on the window $w[n]$ used. So in order to evaluate the frequency response of $y[n] = x[n]\, w[n]$, the quantity $W(e^{j\omega})$ must first be evaluated.

$W(e^{j\omega})$ is evaluated for a rect window (or an implicit window) of length N so that $w[n] = 1$ for all n. The DTFT of $w[n]$ is then

$$W(e^{j\omega}) = \sum_{n=0}^{N-1} e^{-j\omega n} = \frac{1 - e^{-j\omega N}}{1 - e^{-j\omega}}. \tag{B.5}$$

Making use of the following expansions:

$$1 - e^{-j\omega} = e^{-j\omega/2}(e^{j\omega/2} - e^{-j\omega/2}) \tag{B.6}$$

$$1 - e^{-j\omega N} = e^{-j\omega N/2}(e^{j\omega N/2} - e^{-j\omega N/2}), \tag{B.7}$$

then the DTFT of a rect can be written as:

$$W(e^{j\omega}) = \frac{1 - e^{-j\omega N}}{1 - e^{-j\omega}} = \frac{e^{-j\omega N/2}}{e^{-j\omega/2}} \left(\frac{e^{j\omega N/2} - e^{-j\omega N/2}}{e^{j\omega/2} - e^{-j\omega/2}} \right) \frac{2j}{2j} \tag{B.8}$$

$$= e^{-j\omega(N-1)/2} \frac{\sin(\omega N/2)}{\sin(\omega/2)}. \tag{B.9}$$

Recalling that one definition of the Dirichlet kernel (or "periodic sinc" function) is

$$D_n(x) = \frac{\sin(nx/2)}{\sin(x/2)}, \tag{B.10}$$

then the DTFT is expressible in terms of the Dirichlet kernel:

$$W(e^{j\omega}) = e^{-j\omega(N-1)/2} D_N(\omega). \tag{B.11}$$

Since the FFT is used for power spectrum estimation, only the magnitude-squared response is of interest, which is

$$|W(e^{j\omega})|^2 = |D_N(\omega)|^2. \tag{B.12}$$

Equation (B.12) is the continuous-valued frequency response of a rect window function using a DTFT. In practice, a DTFT is approximated by a DFT with sufficiently many samples. Thus, while Eq. (B.12) gives the analytic frequency response of an FFT bin, it could be approximated computationally by zero-padding the window $w[n]$ by some amount and then computing the FFT for a large number of samples.

Since the signal frequency response $X(e^{j\omega})$ is convolved with the window frequency response $W(e^{j\omega})$, the value of a given FFT bin $Y[k]$ is not a single signal frequency (i.e., $X(e^{j\omega})$ for some ω), but the linear combination of all signal frequencies weighted by the window spectrum.

Some examples are shown in Fig. B.1. The frequency response for a 16-point FFT is shown. The frequencies for FFT bin centers are indicated with the stem plots. Note that the response follows a Dirichlet kernel. Additionally, the frequency response of any given bin is the weighted combination of all other frequencies except for the frequencies at the centers of the other bins.

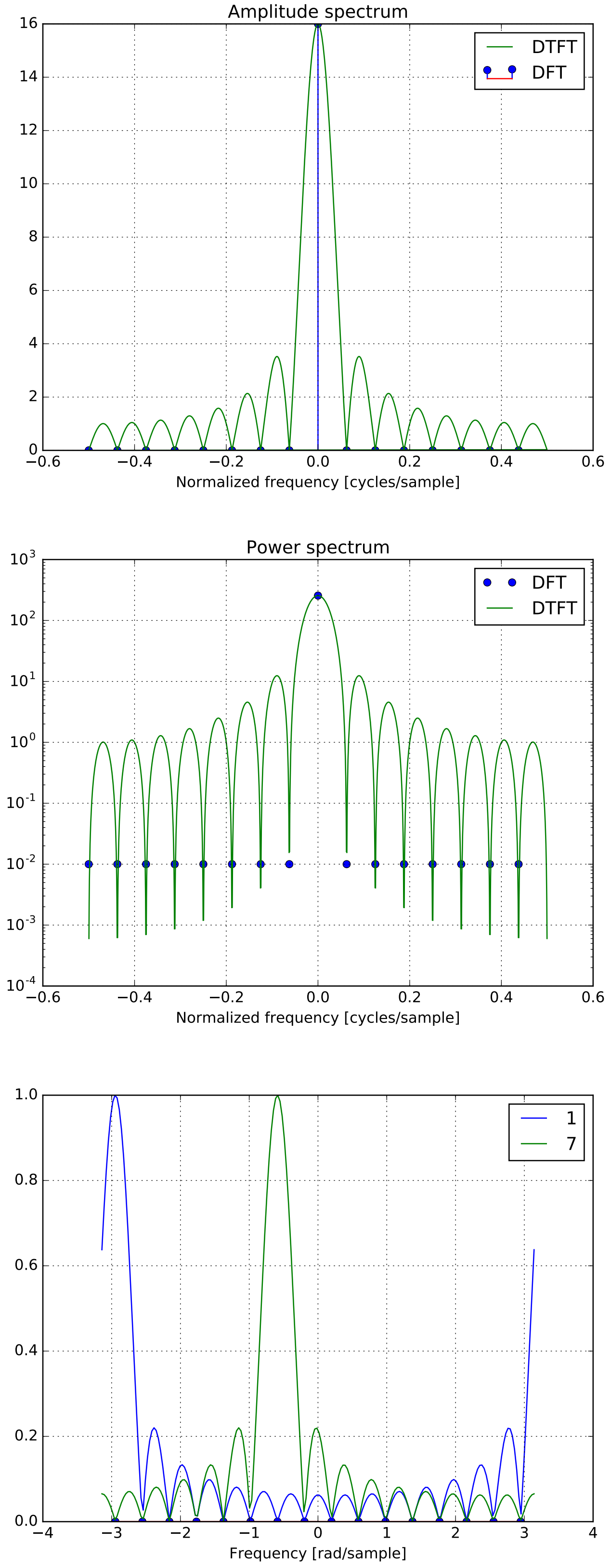

Figure B.1: The magnitude (top) and magnitude-squared (middle) frequency response of an FFT bin. The frequency response (bottom) for two example bins in a 16-point FFT.

Table B.1: FFT chunk parameters

Beam	# of chunks	Window parameters c	p
Mid	5	1.521 45	0.75
Side	8	1.685 56	0.5

B.2 ASCAT Onboard Processing

ASCAT transmits linear FM pulses.[1] The received signal is dechirped and sampled at 412.5 kHz. The sampled mid and side beams contain 2252 and 3193 samples, respectively. These samples are then divided into overlapping chunks of 512 samples. Each FFT chunk is referred to as a *range look*.

The window applied to each chunk is specified in [85], Eq. 6.2.7-8. The number of chunks and the window parameters are shown in Table B.1. A generalized Welch's power spectrum estimate is computed, where each chunk is windowed, and then a 512 point FFT is performed. Half of the samples are discarded (the negative frequencies are redundant in a real-valued signal) and the magnitude-square is taken. All the transformed chunks are averaged together to give the final power spectrum estimate: power as a function of frequency, which in ground processing maps to σ° as a function of range.

The window function used is described as

$$w(t) = \begin{cases} c & 0 \le |t| \le p\,T_{rl}/2 \\ \frac{c}{2}\left[1 + \cos\left(\frac{2\pi(|t| - pT_{rl}/2)}{T_{rl}(1-p)}\right)\right] & p\,T_{rl}/2 \le |t| \le T_{rl}/2 \end{cases}, \tag{B.13}$$

where T_{rl} is the "range look duration" and is 1.241 212 ms. Note that c and p differ for mid and side beams. The sampled window function $w[n]$ is $w(t)$ where $t \in [-T_{rl}/2, T_{rl}/2]$ and $N = 512$ samples are taken. The window function is plotted in Fig. B.2 for the mid and side beams. The window is a tapered rect, similar to a Tukey window.

B.3 Windowed FFT Bin Response

The magnitude of the Fourier transform for one of the windows is shown in Fig. B.3, with the response from a rect window, for comparison. While the peak sidelobe level and mainlobe width are not drastically different from the rect response, the sidelobes taper off more quickly and the mainlobe is slightly wider. The closer view of the mainlobe is shown in Fig. B.4 in comparison with a rect window mainlobe.

B.4 Summary

The ASCAT processing maps the FFT bin frequency response to a spatial response along the Earth surface. Therefore, this appendix has described the frequency response of the

---

[1] Most of the information in this section comes from from [84], an email from Julian Wilson at EUMETSAT on 2009-01-23.

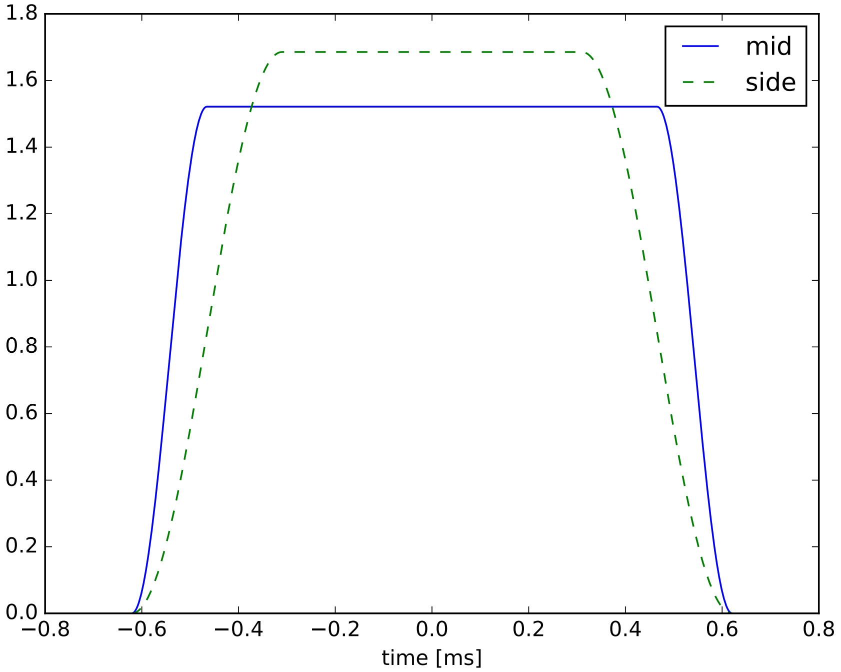

Figure B.2: The window function applied to each 512-sample chunk.

FFT bins computed onboard ASCAT. For a rect window (or, an unwindowed case), the FFT bin frequency response is shown to be related to a Dirichlet kernel. The window used onboard ASCAT is described and its corresponding mainlobe frequency response is very similar to, but slightly wider than, a rect. Different window parameters are used for the mid and side beams, and therefore the response on the ground is slightly different for the mid and side beams.

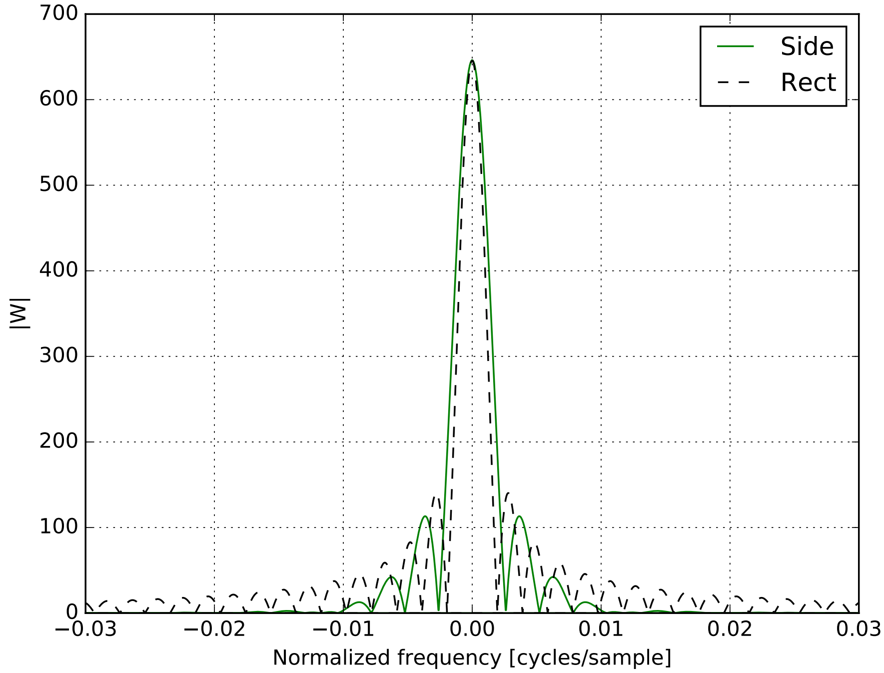

Figure B.3: The magnitude of the Fourier transform of the chunk window for side beams, along with the response from a rect window. The rect response has been renormalized to match the peak level of the side range look window response. This plot is horizontally zoomed in order to show more detail near the mainlobe (the full domain is -0.5 to 0.5 cycles/sample).

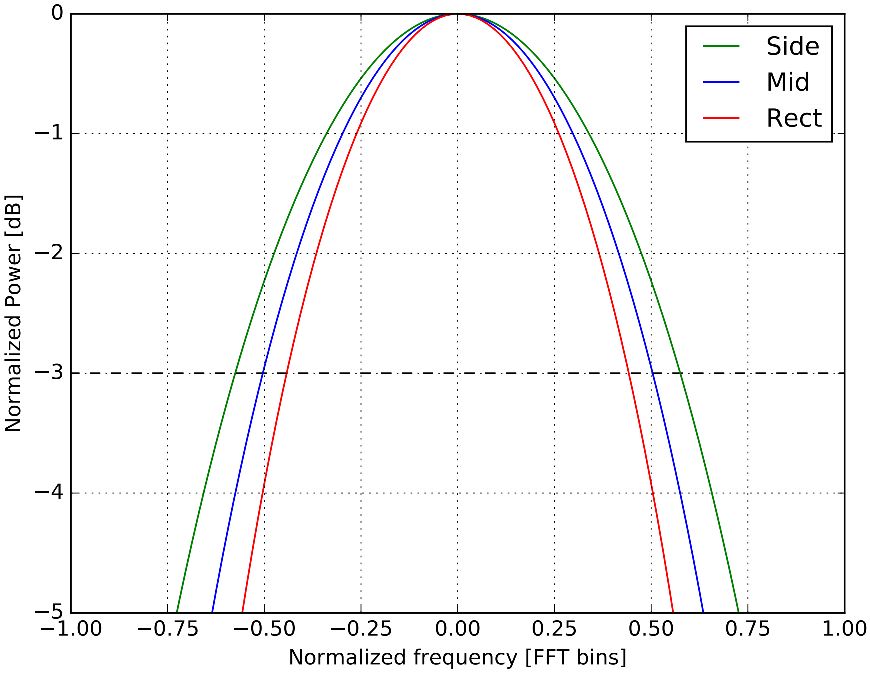

Figure B.4: The magnitude-squared of the Fourier transform of the chunk windows, along with a rect window for comparison. This plot is horizontally zoomed in order to show more detail near the mainlobe. The 3 dB width of the windows is estimated to be 0.88, 1.0, and 1.125 FFT bins for the rect, mid, and side windows, respectively.

Appendix C

Reconstruction Image Statistics

This appendix derives the predicted GRD and AVE statistics and validates the predictions through comparison to corresponding sample statistics. To simplify the analysis, no incidence angle dependence is included.

For pixels m and n of the output image $\hat{a}$ (the 2d image $\hat{a}[x, y]$ is vectorized to a column vector $\hat{a}_j$), the mean at pixel m and the autocorrelation and autocovariance between pixels m and n are

$$\begin{aligned}
\mu_{\hat{a}}[m] &= E[\hat{a}_m] \\
r_{\hat{a}}(m, n) &= \mathrm{cor}_{\hat{a}}(m, n) = E[\hat{a}_m \hat{a}_n] \\
k_{\hat{a}}(m, n) &= \mathrm{cov}_{\hat{a}}(m, n) = E[(\hat{a}_m - E[\hat{a}_m])(\hat{a}_n - E[\hat{a}_n])].
\end{aligned}$$

Note that the pixel variance is a special case of the autocovariance: $\mathrm{var}_{\hat{a}}[m] = k_{\hat{a}}(m, m)$. Similarly, for measurements a and b of the measurement vector z_i, the mean and autocovariance are

$$\begin{aligned}
\mu_z[a] &= E[z_a] \\
r_z(a, b) &= \mathrm{cor}_z(a, b) = E[z_a z_b] \\
k_z(a, b) &= \mathrm{cov}_z(a, b) = E[(z_a - E[z_a])(z_b - E[z_b])].
\end{aligned}$$

Two sources of randomness are modeled: first, the noise-free measurements are treated as deterministic. The random measurement noise is modeled and the mean and autocovariance of the AVE and GRD outputs are analytically determined. Simulation is used to measure the pixel mean and autocovariance of the AVE and GRD outputs. In order to validate the prediction, they are compared against the simulated values.

The second source of randomness is to consider the truth σ° scene, before sampling, as a random process with an associated pixel mean and autocovariance. Thus the noise-free measurements are stochastic and are characterized by their associated mean and autocovariance. Finally, the AVE and GRD methods are applied to predict the mean and autocovariance of the reconstructed image. As with the first approach, simulation is used to validate the predicted values.

Some background on confidence intervals is first discussed in Appendix C.1. Then the reconstruction mean and autocovariance are predicted and validated in Appendix C.2, only considering the effect of measurement noise. The reconstructed image mean and autocovariance are again predicted in Appendix C.3, this time modeling the true σ° scene as a random process. Both effects are combined in Appendix C.4 and the predicted values are validated. Appendix C.5 concludes.

C.1 Confidence Intervals

To validate the predictions made below, the predicted mean and variance are compared against the sample mean and variance. In order to evaluate the accuracy of the predicted mean and variance, a Neyman-Pearson hypothesis test is created for each case. Under the Central Limit Theorem, the distribution of the sample mean $\bar{x}$ approaches a Gaussian, distributed as $\mathcal{N}(\mu, \sigma^2/N)$ where N is the number of realizations averaged together, μ is the true mean, and σ^2 is the true variance. The distribution of the sample variance s^2 similarly approaches a scaled chi-squared distribution.

For the sample mean, the null hypothesis H_0 is that the sample mean for a pixel equals the predicted mean for that pixel:

$$\begin{aligned} &H_0 : \bar{x} = \mu,\ \bar{x} \sim \mathcal{N}(\mu, \sigma^2/N) \\ &H_1 : \bar{x} \neq \mu,\ \bar{x} \nsim \mathcal{N}(\mu, \sigma^2/N). \end{aligned}$$

Assuming the null hypothesis is true, the predicted mean μ and the predicted variance σ^2 are both assumed correct. For this hypothesis test, the sample mean $\bar{x}$ is the test statistic. It is normalized to find the z-score:

$$z = \frac{\bar{x} - \mu}{\sqrt{\sigma^2/N}},$$

where z is distributed as the unit normal distribution, $z \sim \mathcal{N}(0, 1)$.

In this appendix, the test significance level, α, is set to 0.05. This, in conjunction with the distribution of z, gives the well-known result that 95 % of the probability may be bounded by

$$\bar{x} \pm 1.96(\sigma/\sqrt{N}).$$

This is the 95 % confidence interval of $\bar{x}$. An illustration is shown in Fig. C.1. The frequentist interpretation is that, given many groups of data with the same underlying true mean and variance, if the sample mean is computed for each group, then 95 % of the time, the true mean μ will lie within the 95 % confidence interval of the sample mean.

In this appendix the sample and predicted statistics are computed separately for each pixel or for each measurement. Thus, it is expected that for 95 % of the pixels (or measurements), the predicted mean lies within the 95 % confidence interval around the sample mean. The null hypothesis is therefore rejected 5 % of the time, which is what is expected for an α (also called the probability of false alarm, or type I error) of 0.05.

The hypothesis test for the sample variance is similar. The null hypothesis H_0 is that the sample variance s^2 equals the predicted variance:

$$\begin{aligned} &H_0 : s^2 = \sigma^2 \\ &H_1 : s^2 \neq \sigma^2. \end{aligned}$$

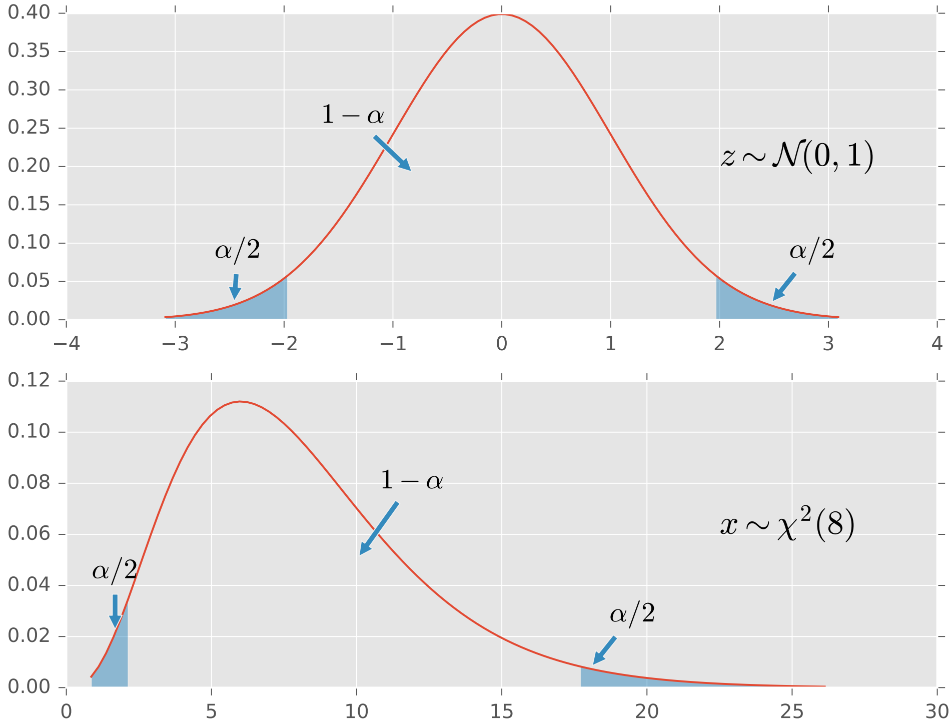

Figure C.1: A unit normal distribution (top) and a chi-squared distribution with 8 degrees of freedom (bottom). The cumulative probability α is indicated by the shaded portions at the two tails of each distribution. The unshaded portion contains $1-\alpha$ of the probability.

The test statistic is $x = (N-1)\frac{s^2}{\sigma^2}$, where $x \sim \chi^2(N-1)$, a chi-squared distribution with $N-1$ degrees of freedom. In this case, the $(1-\alpha)\%$ confidence interval for σ^2, the true variance, is

$$\frac{(N-1)s^2}{a} \leq \sigma^2 \leq \frac{(N-1)s^2}{b},$$

where a and b are the points in the chi-squared distribution that contain $1-\alpha$ of the probability. An illustration in this case is shown in Fig. C.1 using a chi-squared distribution with 8 degrees of freedom. As $N \to \infty$, a chi-squared distribution with $N-1$ degrees of freedom approximates a (shifted) Gaussian distribution.

C.2 Measurement Noise

C.2.1 Predicted Values

As stated in Eq. (2.19), the multiplicative measurement noise model is

$$z_i = \sigma^{\circ}_{\text{meas,i}}(1 + K_{p,i}\,\nu_i), \tag{C.1}$$

where $\sigma^\circ_{\text{meas,i}}$ is the sampled backscatter value, z_i is the noisy measurement, $K_{p,i}$ is a per-measurement noise term, and ν_i is an correlated Gaussian random process with zero mean and unit variance. For ASCAT, $K_{p,i}$ is treated as constant across the measurements, so that $K_{p,i} = K_p$.

Substituting Eq. (2.19) into the AVE algorithm, Eq. (2.26), and taking the expectation over ν_i, the mean of $\sigma^\circ_{\text{ave}}$ for pixel m is

$$\begin{aligned}
\mu_{\text{ave}}[m] &= E\left[\frac{\sum_i \sigma^\circ_{\text{meas,i}}(1+K_p\nu)h_{im}}{\sum_i h_{im}}\right] \\
&= \frac{\sum_i \sigma^\circ_{\text{meas,i}}E[(1+K_p\nu)]h_{im}}{\sum_i h_{im}} = \frac{\sum_i \sigma^\circ_{\text{meas,i}}(1+0)h_{im}}{\sum_i h_{im}} \\
&\boxed{\mu_{\text{ave}}[m] = \frac{\sum_i \sigma^\circ_{\text{meas,i}}h_{im}}{\sum_i h_{im}}}\,. \qquad \text{(C.2)}
\end{aligned}$$

The AVE autocorrelation, noting that $E[\nu_i] = 0$ and $E[\nu_l\nu_k] = \delta_{lk}$, is

$$\begin{aligned}
r_{\text{ave}}(m,n) = E[\sigma^\circ_{\text{ave}}[m]\sigma^\circ_{\text{ave}}[n]] &= E\left[\left(\frac{\sum_l \sigma^\circ_{\text{meas},l}\,h_{lm}\,(1+K_p\nu_l)}{\sum_l h_{lm}}\right)\left(\frac{\sum_k \sigma^\circ_{\text{meas},k}\,h_{kn}\,(1+K_p\nu_k)}{\sum_k h_{kn}}\right)\right] \\
&= \frac{E\left[\sum_l\sum_k \sigma^\circ_{\text{meas},l}\sigma^\circ_{\text{meas},k}\,h_{lm}h_{kn}\,(1+K_p\nu_l)(1+K_p\nu_k)\right]}{\sum_l h_{lm}\sum_k h_{kn}} \\
&= \frac{\sum_l\sum_k \sigma^\circ_{\text{meas},l}\sigma^\circ_{\text{meas},k}\,h_{lm}h_{kn}\,E\left[(1+K_p\nu_l+K_p\nu_k+K_p^2\nu_l\nu_k)\right]}{\sum_l h_{lm}\sum_k h_{kn}} \\
&= \frac{\sum_l\sum_k \sigma^\circ_{\text{meas},l}\sigma^\circ_{\text{meas},k}\,h_{lm}h_{kn}\,(1+K_p^2\delta_{lk})}{\sum_l h_{lm}\sum_k h_{kn}} \\
&= \frac{\left(\sum_l \sigma^\circ_{\text{meas},l}\,h_{lm}\right)\left(\sum_k \sigma^\circ_{\text{meas},k}\,h_{kn}\right) + K_p^2\sum_l(\sigma^\circ_{\text{meas},l})^2 h_{lm}h_{ln}}{\sum_l h_{lm}\sum_k h_{kn}}. \qquad \text{(C.3)}
\end{aligned}$$

The AVE autocovariance is simpler due to removing the mean terms:

$$\boxed{k_{\text{ave}}(m,n) = \frac{K_p^2\sum_l(\sigma^\circ_{\text{meas},l})^2 h_{lm}h_{ln}}{\sum_l h_{lm}\sum_k h_{kn}}}\,. \qquad \text{(C.4)}$$

Above, i, l, and k index over the measurements and h_{ij} is the SRF value of measurement i at pixel j.

The mean and autocovariance for GRD are similar, but h_{ij} is replaced with the GRD indicator function G_{ij}. Noting that $\sum_i G_{ij} = N_j$ and $\sum_i G_{im}G_{in} = N_m\delta_{mn}$,

$$\boxed{\mu_{\text{grd}}[m] = \frac{\sum_i \sigma^\circ_{\text{meas,i}}G_{im}}{N_m}}\,. \qquad \text{(C.5)}$$

$$\begin{aligned} k_{\text{grd}}(m,n) &= \frac{K_p^2 \sum_l (\sigma^\circ_{\text{meas},l})^2 G_{lm} G_{ln}}{\sum_l G_{lm} \sum_k G_{kn}} \\ &= \frac{K_p^2 \delta_{mn} \sum_l (\sigma^\circ_{\text{meas},l})^2 G_{lm} G_{lm}}{N_m N_n} \end{aligned}$$

$$\boxed{k_{\text{grd}}(m,n) = \begin{cases} \dfrac{K_p^2 \sum_l (\sigma^\circ_{\text{meas},l} G_{lm})^2}{(N_m)^2}, & m = n \\ 0, & m \neq n \end{cases}}. \tag{C.6}$$

Because GRD pixels do not share measurements with other pixels, the autocovariance of GRD pixels—due only to measurement noise—is 0 when $m \neq n$.

C.2.2 Sample Values

The predicted reconstruction statistics are validated through simulation. A synthetic truth image is created and sampled using actual ASCAT observation geometry, including the SRF. The SRF is computed for each measurement and stored (as elements h_{ij}, the SRF value for measurement i at pixel j) as well as the synthetic noise-free measurements $\sigma^\circ_{\text{meas,i}}$. Noise is added to the measurements using Eq. (C.1), with multiple realizations of ν. For the results below, 1000 noise realizations are generated. K_p for ASCAT is assumed to be a constant value of 0.20.

From the noisy measurements, the GRD and AVE algorithms reconstruct the output images for each realization of noisy measurements. With 1000 noise realizations, 1000 sets of GRD and AVE images are created. To measure the reconstruction mean and autocovariance, the sample mean and sample autocovariance are taken over the realizations.

The sample mean and sample autocovariance are computed independently for each pixel m. Whether the image is generated from the GRD or AVE methods, the output images here are referred to as $a_t[j]$ where j is the pixel index and t is the realization index. The total number of realizations is T ($\sum_t 1 = T$). The sample mean for pixel j is

$$\hat{\mu_a}[j] = \frac{1}{T} \sum_{t=1}^{N} a_t[j], \tag{C.7}$$

and the unbiased sample autocovariance for pixels m and n is

$$\hat{k_a}(m,n) = \frac{1}{T-1} \sum_{t=1}^{N} (a_t[m] - \mu_{\hat{a}}[m])(a_t[n] - \mu_{\hat{a}}[n]). \tag{C.8}$$

The sample autocovariance $\hat{k_a}(m,n)$ may be computed for every pixel pair (m,n). However, for brevity, only the pixel variance $\hat{k_a}(m,m)$ is considered in this appendix.

C.2.3 Validation

The predicted and sample mean are shown for a subset of GRD pixels in Fig. C.2. The predicted mean is Eq. (C.5) and the predicted variance is Eq. (C.6) for $m = n$. The sample mean and variance are computed as detailed above. Results for AVE are similar.

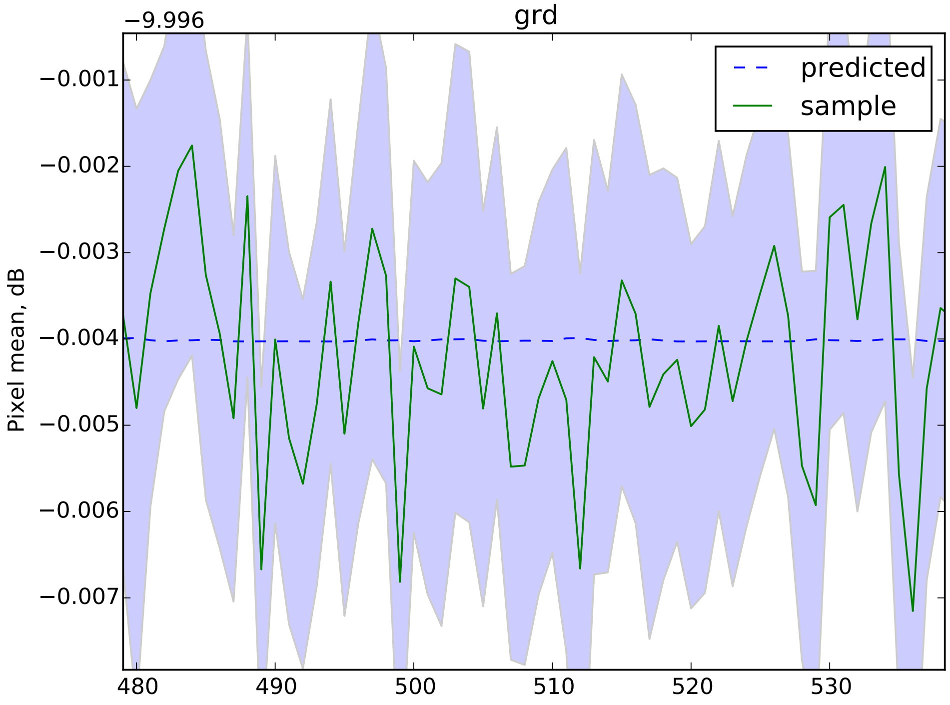

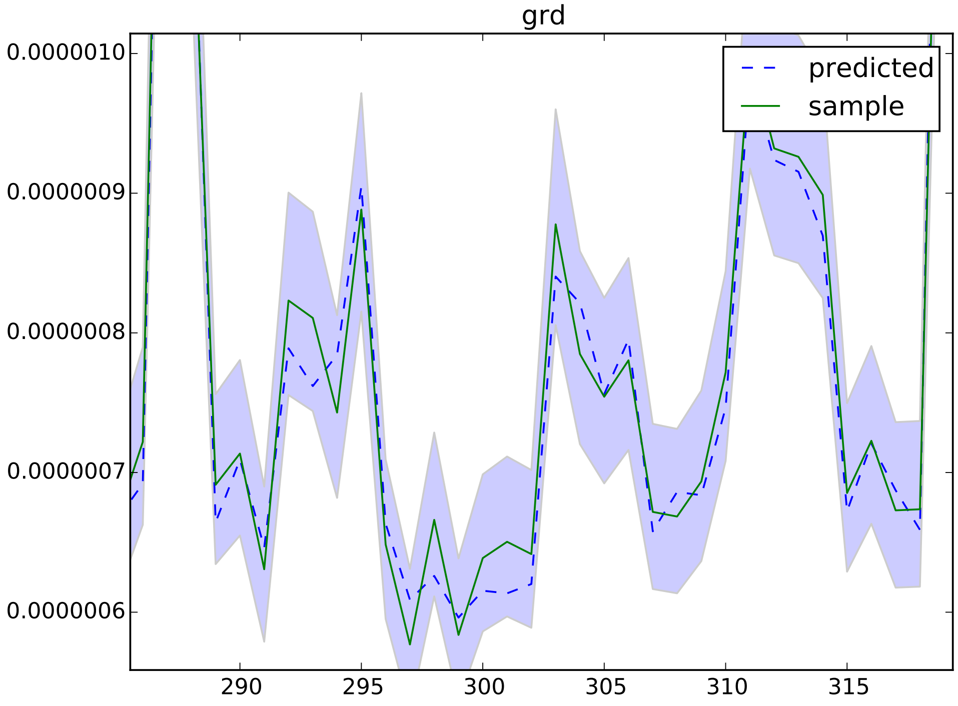

Figure C.2: The mean (top) and variance (bottom) for GRD as a function of pixel index. The predicted values are indicated with dashed lines and the sample values with a solid line. The 95 % confidence interval is indicated by the error bars.

Table C.1: The number of pixels whose predicted mean or variance falls within the 95 % confidence interval of the sample mean and variance.

Statistic	Pixels	
GRD sample mean	555/576	96.4 %
GRD sample variance	544/576	94.4 %
AVE sample mean	54796/57419	95.4 %
AVE sample variance	54551/57419	95.0 %

Since each pixel is considered separately, it is expected that for 95 % of the pixels, the predicted mean and variance fall within the 95 % confidence intervals of the sample mean and sample variance. The actual number of pixels within the confidence intervals for GRD and AVE are listed in Table C.1. The rejection rate matches that set by the choice of α: only 5 % of the pixels are outside the 95 % confidence interval. This validates the predicted mean and variance. The autocovariance for $m \neq n$ is not shown in this appendix, but a comparison between the predicted and sample autocovariances similarly matches well.

C.3 True Signal Uncertainty

The true image $A[j] = \sigma^\circ[x, y]$ is modeled as having first- and second-order statistics $\mu_A[j]$ and $k_A(m, n)$, the mean at pixel j, and autocovariance between pixels m and n, respectively. Neglecting measurement noise, the discretized sampling process is

$$z_i = \frac{\sum_j A[j] h_{ij}}{\sum_j h_{ij}}. \tag{C.9}$$

The measurement mean is

$$\begin{aligned}
\mu_z[i] &= E\left[\frac{\sum_j A[j] h_{ij}}{\sum_j h_{ij}}\right] \\
&= \frac{\sum_j E\left\{A[j]\right\} h_{ij}}{\sum_j h_{ij}} \\
&\boxed{\mu_z[i] = \frac{\sum_j \mu_A[j] h_{ij}}{\sum_j h_{ij}}}.
\end{aligned} \tag{C.10}$$

The noise-free measurement autocorrelation is

$$\begin{aligned}
r_z(a, b) = E[z_a z_b] &= \frac{1}{\sum_m h_{am}} \frac{1}{\sum_n h_{bn}} E\left\{\sum_m A[m] h_{am} \sum_n A[n] h_{bn}\right\} \\
&= \frac{1}{\left(\sum_m h_{am}\right)\left(\sum_n h_{bn}\right)} \sum_m \sum_n E\left\{A[m]A[n]\right\} h_{am} h_{bn} \\
&= \frac{\sum_m \sum_n r_A(m, n) h_{am} h_{bn}}{\left(\sum_m h_{am}\right)\left(\sum_n h_{bn}\right)},
\end{aligned}$$

where a and b index over measurements and m and n index over pixels. Noting that the autocorrelation may be expressed in terms of autocovariance, $r_A(m,n) = k_A(m,n) + \mu_A[m]\mu_A[n]$, the noise-free measurement autocovariance is

$$\begin{aligned}
k_z(a,b) &= E[(z_a - \mu_z[a])(z_b - \mu_z[b])] = r_z(a,b) - \mu_z[a]\mu_z[b] \\
&= \frac{\sum_m \sum_n r_A(m,n) h_{am} h_{bn}}{\left(\sum_m h_{am}\right)\left(\sum_n h_{bn}\right)} - \frac{\sum_m \mu_A[m] h_{am}}{\sum_m h_{am}} \frac{\sum_n \mu_A[n] h_{bn}}{\sum_n h_{bn}} \\
&= \frac{\sum_m \sum_n \left(k_A(m,n) + \mu_A[m]\mu_A[n]\right) h_{am} h_{bn}}{\left(\sum_m h_{am}\right)\left(\sum_n h_{bn}\right)} - \frac{\sum_m \sum_n \mu_A[m]\mu_A[n] h_{am} h_{bn}}{\left(\sum_m h_{am}\right)\left(\sum_n h_{bn}\right)}
\end{aligned}$$

$$\boxed{k_z(a,b) = \frac{\sum_m \sum_n k_A(m,n) h_{am} h_{bn}}{\left(\sum_m h_{am}\right)\left(\sum_n h_{bn}\right)}}. \tag{C.11}$$

Using the AVE algorithm from Eq. (2.26), the mean for each pixel j and the autocovariance between the pixels m and n are

$$\mu_{\text{ave}}[j] = \frac{\sum_a \mu_z[a] h_{aj}}{\sum_a h_{aj}}, \tag{C.12}$$

$$k_{\text{ave}}(m,n) = \frac{\sum_a \sum_b k_z(a,b) h_{am} h_{bn}}{\sum_a h_{am} \sum_b h_{bn}}, \tag{C.13}$$

where a and b index the measurements.

For the GRD method, the indicator G_{ij} replaces the SRF value h_{ij} and $\sum_i G_{ij} = N_j$ is the number of measurements falling within each GRD pixel j. The GRD mean and autocovariance are therefore

$$\mu_{\text{grd}}[j] = \frac{1}{N_j} \sum_a \mu_z[a] G_{aj}, \tag{C.14}$$

$$k_{\text{grd}}(m,n) = \frac{1}{N_m N_n} \sum_a \sum_b k_z(a,b) G_{am} G_{bn}, \tag{C.15}$$

where a and b index over the measurements. Unlike the deterministic measurement case in Eq. (C.6), the GRD autocovariance is not necessarily a delta function but a function of the truth image autocovariance $k_A(m,n)$.

For brevity, the validation of the predicted quantities Eqs. (C.10) to (C.15) is deferred to the next section.

C.4 Signal and Noise Uncertainty

C.4.1 Predicted Values

Including measurement noise modeled in Eq. (C.1) into the sampling equation Eq. (C.9), the noisy sampling is expressed as

$$z_i = \frac{\sum_j \sigma^\circ[j] h_{ij}}{\sum_j h_{ij}} (1 + K_p \nu_i).$$

The measurement noise ν_i is assumed uncorrelated with the source image, so $E[A[j]\nu_i] = E[A[j]]E[\nu_i] = 0$. The noisy measurement mean is therefore

$$\begin{aligned}
\mu_z[i] &= E\left[\frac{\sum_j A[j]h_{ij}}{\sum_j h_{ij}}(1 + K_p\nu_i)\right] \\
&= \frac{\sum_j E\{A[j]\}\, h_{ij}}{\sum_j h_{ij}} + K_p\frac{\sum_j E\{A[j]\nu_i\}\, h_{ij}}{\sum_j h_{ij}} \\
&\boxed{\mu_z[i] = \frac{\sum_j \mu_A[j]h_{ij}}{\sum_j h_{ij}}},
\end{aligned} \tag{C.16}$$

which is identical to Eq. (C.10).

The autocorrelation between measurements z_a and z_b is

$$\begin{aligned}
r_z(a,b) &= E\left\{\left(\underbrace{\frac{\sum_k A[k]h_{ak}}{\sum_k h_{ak}}}_{\alpha} + K_p\nu_a \underbrace{\frac{\sum_k A[k]h_{ak}}{\sum_k h_{ak}}}_{\alpha}\right)\left(\underbrace{\frac{\sum_l A[l]h_{bl}}{\sum_l h_{bl}}}_{\beta} + K_p\nu_b \underbrace{\frac{\sum_l A[l]h_{bl}}{\sum_l h_{bl}}}_{\beta}\right)\right\} \\
&= E\left\{\alpha\beta + K_p\nu_b\alpha\beta + K_p\nu_a\alpha\beta + K_p^2\nu_a\nu_b\alpha\beta\right\} = E[\alpha\beta] + 0 + 0 + K_p^2\delta_{ab}E[\alpha\beta] \\
&= \frac{\sum_k\sum_l r_A(k,l)h_{ak}h_{bl}}{\sum_k h_{ak}\sum_l h_{bl}}(1 + K_p^2\delta_{ab}).
\end{aligned}$$

The autocovariance between measurements z_a and z_b is

$$\begin{aligned}
k_z(a,b) &= r_z(a,b) - \mu_z[a]\mu_z[b] \\
&= \frac{\sum_k\sum_l \left(k_A(k,l) + \mu_A[k]\mu_A[l]\right) h_{ak}h_{bl}}{\sum_k h_{ak}\sum_l h_{bl}}(1 + K_p^2\delta_{ab}) - \frac{\sum_k\sum_l \mu_A[k]\mu_A[l]h_{ak}h_{bl}}{\sum_k h_{ak}\sum_l h_{bl}} \\
&\boxed{k_z(a,b) = \frac{\sum_k\sum_l k_A(k,l)h_{ak}h_{bl}}{\sum_k h_{ak}\sum_l h_{bl}} + K_p^2\delta_{ab}\frac{\sum_k\sum_l \left(k_A(k,l) + \mu_A[k]\mu_A[l]\right) h_{ak}h_{bl}}{\sum_k h_{ak}\sum_l h_{bl}}}.
\end{aligned} \tag{C.17}$$

With noise included, the measurement mean μ_z is unchanged from Eq. (C.10), but the measurement autocorrelation k_z has an additional term. Because of the Kronecker delta δ_{ab}, the second term is only nonzero when computing the variance of measurement z_a. This implies that the covariance between measurements $a \neq b$ is unaffected by measurement noise. However, with measurement noise, the measurement variance increases. The mean and autocovariance of the reconstructed pixels may be found by substituting the measurement statistics of Eqs. (C.16) and (C.17) into Eqs. (C.12) and (C.13) for AVE and Eqs. (C.14) and (C.15) for GRD.

C.4.2 Sample Values

The predicted statistics of the measurements z_i may be validated through simulation. Multiple realizations of a truth image may be created using known image statistics $\mu_A[j]$ and $k_A(m,n)$. For simplicity, I assume the truth image $A[j]$ is a multi-variate Gaussian so that it is completely described by the choice of mean vector $\vec{\mu_A}$ and covariance matrix Σ. For a size-M truth image, each truth image realization is a random vector $\vec{A} \sim \mathcal{N}(\vec{\mu_A}, \Sigma)$, where the vector

$$\vec{\mu_A} = \begin{bmatrix} \mu_A[0] & \mu_A[1] & \dots & \mu_A[M-1] \end{bmatrix}^T$$

is the mean for each pixel and the covariance matrix Σ contains the autocovariances between every possible pair of pixels:

$$\Sigma = \begin{bmatrix} k_A(0,0) & k_A(0,1) & \cdots & k_A(0,M-1) \\ k_A(1,0) & \ddots & & \vdots \\ \vdots & & \ddots & \vdots \\ k_A(M-1,0) & \dots & \dots & k_A(M-1,M-1) \end{bmatrix}.$$

After creating multiple truth image realizations (all with the same statistics $\mu_A[j]$ and $k_A(m,n)$), the images are sampled with the same sampling geometry h_{ij} as above and measurement noise is optionally added. Then the sample mean and sample autocovariance are computed.

The sample mean for measurement i is

$$\hat{\mu_z}[i] = \frac{1}{N} \sum_{t=1}^{N} z_t[i],$$

and the (unbiased) sample autocovariance for measurements a and b is

$$\hat{k_z}(a,b) = \frac{1}{N-1} \sum_t (z_t[a] - \mu_z[a])(z_t[b] - \mu_z[b]),$$

where t indexes the N realizations. For the noise-free case, N realizations of the truth image are created and sampled. For the noisy case, a single noise realization is created for each truth realization, so there are still N total realizations to average over.

C.4.3 Validation

The predicted mean and variance of the measurements, $\mu_z[i]$ and $k_z(a,b)$, are compared against the sample values for various truth image statistics μ_A and Σ_A. The predicted and sample mean and variance are shown for some measurements in Figs. C.3 and C.4 for 500 realizations of sample values. Measurement noise is both omitted and included for comparison.

Comparing the noisy and noise-free cases in Fig. C.3, although the predicted mean is the same (since Eq. (C.10) and Eq. (C.16) are the same), measurement noise increases the variance of the sample mean, as seen in the broader confidence interval. Measurement noise also affects the variance of the measurements in Fig. C.4: the measurement variance in the noisy case is larger than the noise-free case by two orders of magnitude. The variance increase is due to the second term in Eq. (C.17), where K_p is nonzero due to measurement noise. Within the double summation, the $\mu_A[k]\mu_A[l]$ portion of the summand dominates.

Notwithstanding the difference measurement noise makes, the predicted and sample statistics match very well in all cases for all truth image statistics tested. The number of

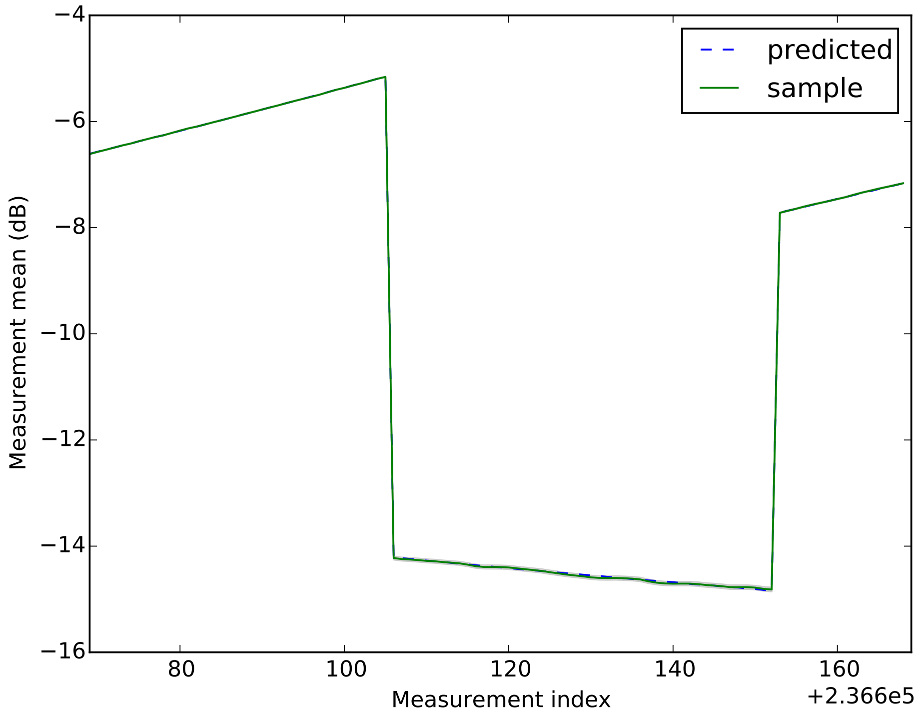

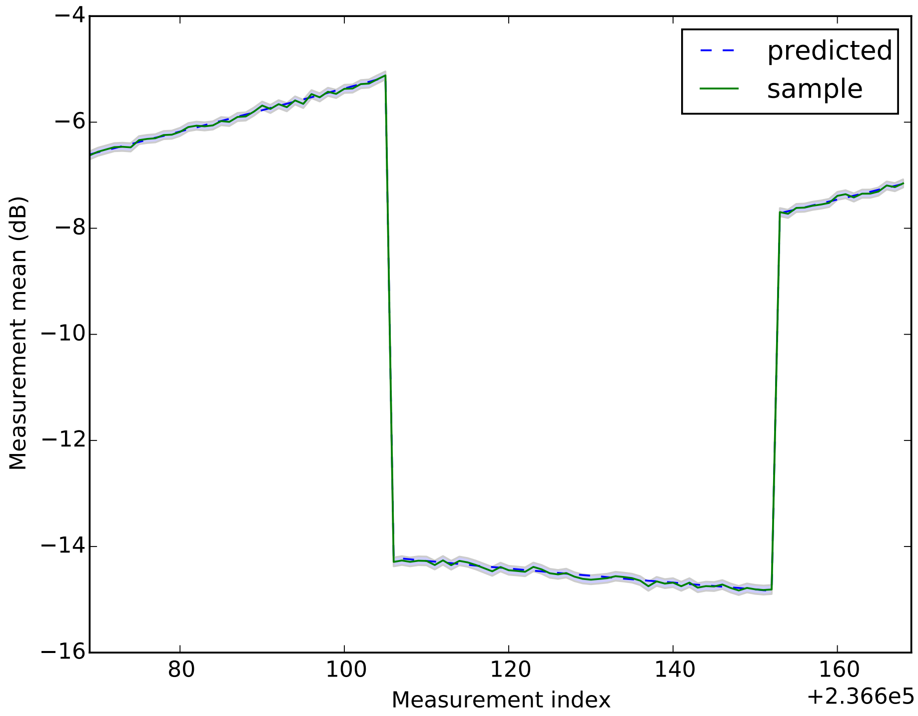

Figure C.3: The predicted and sample mean for both the noise-free (top) and noisy (bottom) measurements.

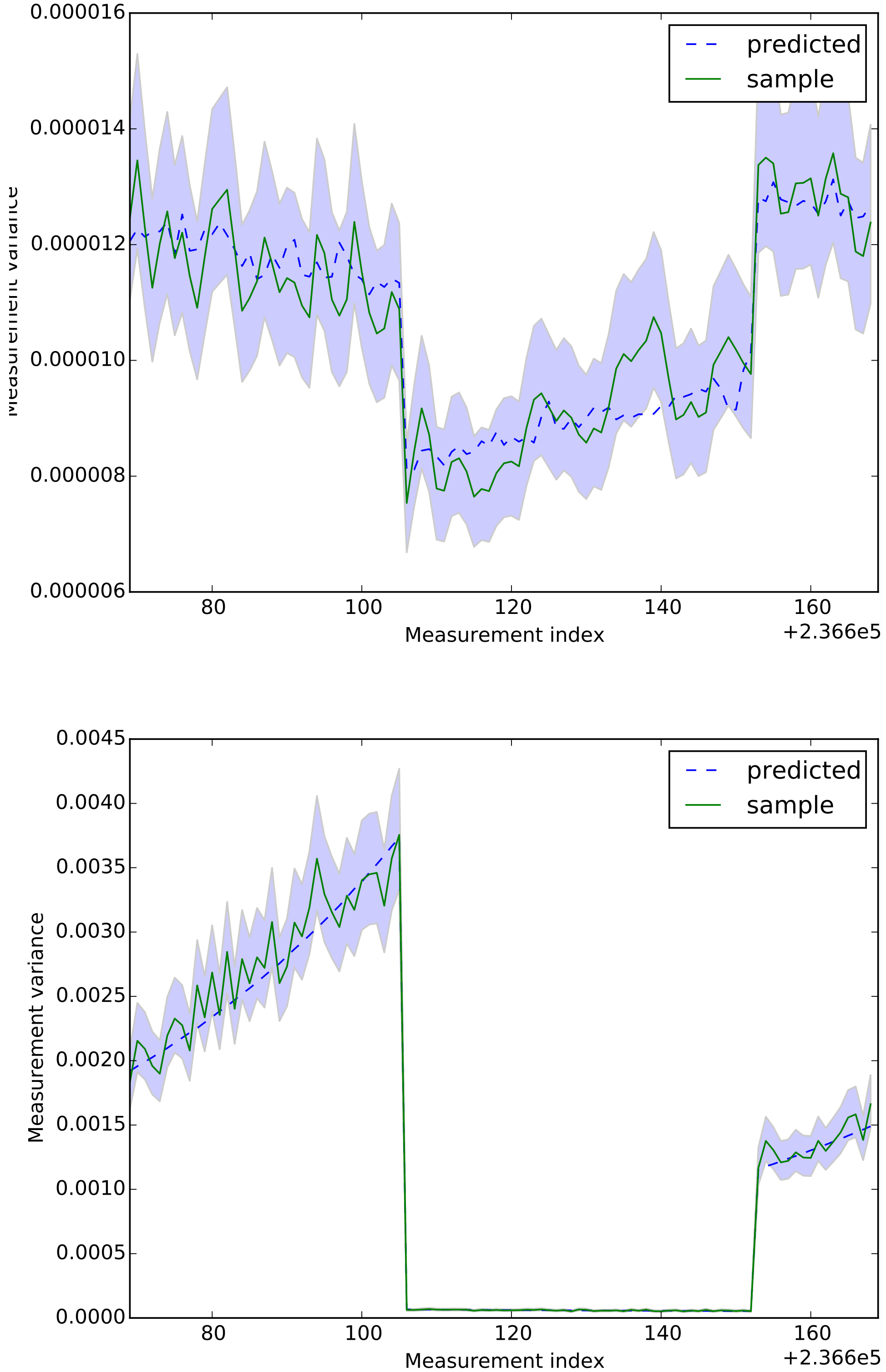

Figure C.4: The predicted and sample variance for both the noise-free (top) and noisy (bottom) measurements.

Table C.2: The number of measurements whose predicted mean or variance falls within the 95 % confidence interval of the sample mean and variance. This is for one particular truth image, but the values are similar for the other truth images tested.

Statistic	Noise-free		Noisy	
Sample mean	282654/299369	94.4 %	284223/299369	94.9 %
Sample variance	284867/299369	95.2 %	283950/299369	94.9 %

measurements with predicted values with the sample statistics 95 % confidence intervals are listed in Table C.2. This validates the predicted measurement statistics, both with and without noise.

The synthetic measurements are next used to validate the GRD and AVE predicted mean and variance, Eqs. (C.12) to (C.15). AVE and GRD images are created from the synthetic measurements. The sample mean and sample variance are computed on the reconstruction outputs over the multiple realizations. The sample statistics are performed over 500 realizations.

As in Appendix C.2.3, the 95 % confidence intervals are computed for the AVE and GRD sample mean and variance. The percentage of the GRD and AVE pixels with the predicted mean or variance within the confidence intervals in all cases is very close to 95 %, validating the accuracy of the predicted values. Although not shown, the behavior of the mean and variance in all cases is similar to Fig. C.2.

C.5 Conclusion

This appendix has derived the pixel mean and autocovariance for the GRD and AVE algorithms. Two sources of randomness are modeled: measurement noise and the uncertainty of the source σ° scene. Measurement noise is first treated in Appendix C.2, where the GRD and AVE mean and autocovariance are predicted. Simulation is used to find the sample mean and variance. The predicted and sample values agree with each other, validating the predicted mean and variance.

Source uncertainty is modeled in Appendices C.3 and C.4 with a true image mean vector and autocovariance matrix. Sampling is modeled and the mean and autocovariance of the sampled measurements are predicted. Simulation is used to find the sample mean and sample autocovariance of the measurements. The sample statistics validate the predicted statistics. Finally, the predicted statistics for AVE and for GRD are computed and likewise validated through simulation.

This analysis provides closed-form solutions for the mean and autocovariance for GRD and for AVE, with measurement noise and truth image uncertainty modeled. Although the ASCAT sample geometry and SRF is applied, any arbitrary sample geometry and SRF is feasible. Therefore, future work could include comparing the measurement and pixel statistics between other scatterometers or radiometers. For simplicity, incidence angle dependence of σ° is not included, but it could be addressed in future work.